



— BUREAU OF —
RECLAMATION

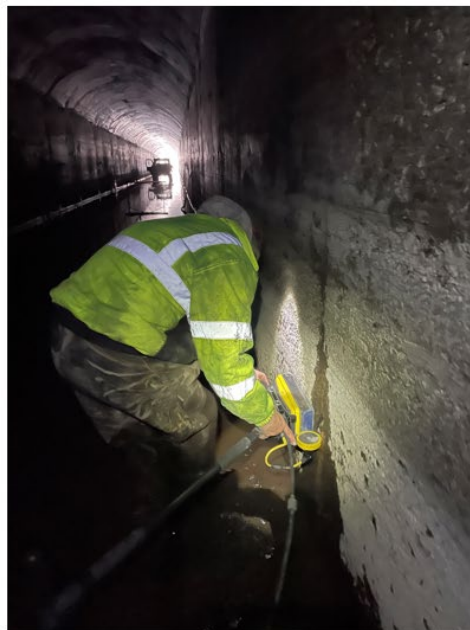
Final Report No. ST-2024-21045-02 (86-68320-2025-16)

Detection of Voids Behind Spillway, Conduits, Canals, Tunnels, and Siphons – Report 2 of 3 on Void Causes, Detection, and Repair

Research and Development Office

Science and Technology

Research Program



REPORT DOCUMENTATION PAGE			Form Approved OMB No. 0704-0188	
<p>The public reporting burden for this collection of information is estimated to average 1 hour per response, including the time for reviewing instructions, searching existing data sources, gathering and maintaining the data needed, and completing and reviewing the collection of information. Send comments regarding this burden estimate or any other aspect of this collection of information, including suggestions for reducing the burden, to Department of Defense, Washington Headquarters Services, Directorate for Information Operations and Reports (0704-0188), 1215 Jefferson Davis Highway, Suite 1204, Arlington, VA 22202-4302. Respondents should be aware that notwithstanding any other provision of law, no person shall be subject to any penalty for failing to comply with a collection of information if it does not display a currently valid OMB control number.</p> <p>PLEASE DO NOT RETURN YOUR FORM TO THE ABOVE ADDRESS.</p>				
1. REPORT DATE (DD-MM-YYYY) 03/04/2025		2. REPORT TYPE Research		3. DATES COVERED (From - To) 10/15/2020 to 03/04/2025
4. TITLE AND SUBTITLE Detection of Voids Behind Spillways, Conduits, Canals, Tunnels, and Siphons This is one of three reports covering void causes, detection, and repair.			5a. CONTRACT NUMBER XXXR4524KS-RR4888FARD2100401 F397A	
			5b. GRANT NUMBER	
			5c. PROGRAM ELEMENT NUMBER 1541 (S&T)	
6. AUTHOR(S) Sarah L. Morton Rupert, Ph.D. Camilla C. Warden			5d. PROJECT ID NUMBER Final Report ST-2024-21045-02	
			5e. TASK NUMBER	
			5f. WORK UNIT NUMBER	
7. PERFORMING ORGANIZATION NAME(S) AND ADDRESS(ES) Bureau of Reclamation Technical Service Center Denver, CO			8. PERFORMING ORGANIZATION REPORT NUMBER 86-68320-2025-16	
9. SPONSORING/MONITORING AGENCY NAME(S) AND ADDRESS(ES) Science and Technology Program Research and Development Office Bureau of Reclamation U.S. Department of the Interior Denver Federal Center PO Box 25007, Denver, CO 80225-0007			10. SPONSOR/MONITOR'S ACRONYM(S) Reclamation	
			11. SPONSOR/MONITOR'S REPORT NUMBER(S) (if applicable) Final Report ST-2024-21045-02	
12. DISTRIBUTION/AVAILABILITY STATEMENT Final Report may be downloaded from https://www.usbr.gov/research/projects/index.html				
13. SUPPLEMENTARY NOTES				
14. ABSTRACT Detection of voids along conduits has been attempted in the past using various non-invasive technologies. While progress has been made, underlying challenges exist that have resulted in the limited adoption of these systems. Developing a set of methods and analysis techniques that can help locate voids in a variety of different mediums (concrete, metal, etc.) in a variety of different conditions (dry, wet, below/above the water table, etc.) is a valuable tool for use in facility inspections. This report details three different studies where multiple geophysical methods were deployed to detect voids at three different Reclamation facilities. Results of these methods and summary tables of their findings are included to provide guidance on future investigations.				
15. SUBJECT TERMS Voids, spillway, causes of voids				
16. SECURITY CLASSIFICATION OF:			17. LIMITATION OF ABSTRACT	18. NUMBER OF PAGES 107
a. REPORT U	b. ABSTRACT U	c. THIS PAGE U		
			19b. TELEPHONE NUMBER (Include area code) 3035151691	

Mission Statements

The U.S. Department of the Interior protects and manages the Nation's natural resources and cultural heritage; provides scientific and other information about those resources; honors its trust responsibilities or special commitments to American Indians, Alaska Natives, Native Hawaiians, and affiliated Island Communities.

The mission of the Bureau of Reclamation is to manage, develop, and protect water and related resources in an environmentally and economically sound manner in the interest of the American public.

Disclaimer

Information in this report may not be used for advertising or promotional purchases. The data and findings should not be construed as an endorsement of any product or firm by the Bureau of Reclamation, Department of Interior, or Federal Government. The products evaluated in the report were evaluated for purposes specific to the Bureau of Reclamation mission. Reclamation gives no warranties or guarantees, expressed or implied, for the products evaluated in this report, including merchantability or fitness for a particular purpose.

Acknowledgements

The Science and Technology Program, Bureau of Reclamation, sponsored this research. The author sincerely thanks the reviewers within Reclamation, and at the USACE and FERC.

Cover Image – Geophysical data collection (Sarah L. Morton Rupert, Ph.D., Geophysicist/Bureau of Reclamation)

Detection of Voids Behind Spillways, Conduits, Canals, Tunnels, and Siphons

Final Report No. ST-2024-21045-02

86-68320-2026-16

Report 2 of 3 on Void Causes, Detection, and Repair

Prepared by:

Technical Service Center

Sarah L. Morton Rupert, Ph.D., Geophysicist

Peer Review

Bureau of Reclamation Research and Development Office Science and Technology Research Program

**Final Report ST-2024-21045-02
86-68320-2025-16
Report 2 of 3 on Voice Causes, Detection, and Repair**

Detection of Voids Behind Spillways, Conduits, Canals, Tunnels, and Siphons

Prepared by: Sarah L. Morton Rupert, Ph.D.
Geophysicist, Engineering Geology and Geophysics, 86-68320

Prepared and checked by: Camilla C. Warden
Geophysicist, Engineering Geology, and Geophysics, 86-68320

Peer review by: Miriam M. Johnston, P.G.
Geophysicist, Engineering Geology, and Geophysics, 86-68320

This document has been reviewed under the Research and Development Office Discretionary peer review process, consistent with Reclamation Policy CMP P14. It does not represent and should not be construed to represent the Bureau of Reclamation's determination, concurrence, or policy.

Contents

	Page
1.0	Executive Summary 1
2.0	Introduction..... 1
3.0	Void Detection Methods..... 3
3.1	Ground Penetrating Radar..... 4
3.1.1	BOR Case Studies using GPR 5
3.2	Ultrasonic Pulse Echo 8
3.2.1	BOR Case Study Using UPE 8
3.3	Seismic Methods..... 9
3.3.1	BOR Case Studies Using Seismic Methods..... 12
3.4	Electrical Methods 13
3.4.1	BOR Case Studies Using Electrical Methods 14
3.5	Electromagnetics (EM) 16
3.5.1	BOR Case Studies Using EM Methods 16
3.6	Thermography..... 17
3.6.1	BOR Case Studies Using Thermography 18
4.0	Field Experiments 18
4.1	Experiment 1: Glendo Powerplant..... 19
4.1.1	Background..... 19
4.1.2	Methodology 19
4.1.3	Data Collection 21
4.1.4	Results..... 23
4.2	Experiment 2: Denver Federal Center 32
4.2.1	Background..... 32
4.2.2	Methodology 34
4.2.3	Experimental Design and Data Collection..... 38
4.2.4	Results..... 43
4.3	Experiment 3: A Canal Tunnel 57
4.3.1	Background..... 57
4.3.2	Methodology 60
4.3.3	Data Acquisition 61
4.3.4	Results..... 66
5.0	Conclusion 86
5.1	Experiment 1..... 86
5.2	Experiment 2..... 86
5.3	Experiment 3..... 87
6.0	References..... 89

Tables

1.—Geophysical methods used for void detection investigations.....	3
2.—Field experiments summary.....	19
3.—Summary of concrete slab experiments.....	38
4.—Concrete slab characteristics.....	39
5.—Geophysical results summary table.....	43
6.—Average of slab thickness (ft) across each slab.....	44
7.—SIR Grid Geometries.....	62
8.—Summary table of interpreted GPR anomalies in a canal tunnel.....	66

Figures

1.—Photo of 6 ft tall by 27 ft wide 2-D grid corner points (indicated with yellow stars) starting above the top right corner of the tube entrance and extending to the right for 27 ft in the horizontal direction.	22
2.—Photo of the grid markings and two of the four hanging platform supports and chains.	23
3.—2-D plot of acoustic sounding data set collected by Westin Joy and interpreted by Sarah Rupert for data visualization.	24
4.—2-D plot of slab impulse response average mobility measurements from the 2022 survey in Glendo Draft Tube No. 2.	26
5.—Example of (top) a 2022 measurement with poor sub-liner support from [1.5, 9] and (bottom) a 2022 measurement with good sub-liner support from [5.5, 19.5].....	27
6.—2-D plots of slab impulse response average mobility measurements from the (top) 2022 survey and (bottom) 2023 survey in Glendo Draft Tube No. 2.	28
7.—Measurement from [1, 6] (top) before the grouting repair in 2022 and (bottom) after the grouting repair in 2023.....	29
8.—2-D plot of interpreted UPE results.	30
9.—Example UPE sounding from the 2022 survey.....	31
10.—(a) Photo of the four-by-four and seven-by-seven rebar mat reinforcements.....	33
11.—Photos of GPR data collection at the Denver Federal Center using a (left) cart-based system and (right) handle attachment.....	35
12.—Photo of Impact Echo data collection on the experimental slabs.	36
13.—Impact Echo (IE) amplitude versus frequency plots with automatically estimated peak frequencies (vertical red lines) and corresponding depth to a deeper reflection boundary.....	37
14.—(Left) Photo of geophysicist Miriam Johnston using the FLIR during one of the outdoor experiments.....	38
15.—Photo of field experiments showing each of the four concrete slabs.....	40
16.—Photo of ramp construction on each end of survey area to aid GPR surveying.....	40

17.—Photo of concrete blocks with survey grid marked along the edges to indicate total distance along the survey grid.....	41
18.—Photo of longitudinal tunnel hand dug under the long axis of the experimental setup.	41
19.—Photo of water-filled visqueen films that were placed under each of the four concrete slabs.	42
20.—X-axis (long-axis) GPR profiles across the centerline of each experimental setup.	46
21.—Y-axis (short axis) GPR profiles across each concrete slab in Experiment 1; no void is present in this setup.	47
22.—Depth slices (plan-view profiles) from Experiment 1.....	48
23.—Y-axis (short axis) GPR profiles across each concrete slab in Experiment 2 with an air-filled void; the void centerline is at approximately $y = 2$ ft.....	49
24.—Depth slices (plan-view profiles) from Experiment 2.....	50
25.—Y-axis (short axis) GPR profiles across each concrete slab in Experiment 3 with a water-filled void; the void centerline is at approximately $y = 2$ ft.....	51
26.—Depth slices (plan-view profiles) from Experiment 3.....	52
27.—Y-axis (short axis) GPR profiles across each concrete slab in Experiment 4 with a partially frozen water-filled void; the void centerline is at approximately $y = 2$ ft.	53
28.—Depth slices (plan-view profiles) from Experiment 4.....	54
29.—IE results for each experiment and each slab.....	55
30.—(a) – (d) FLIR images of each slab for each experiment.	56
31.—Photos of exposed timber reinforcement and varying degrees of concrete deterioration observed in A Canal Tunnel during data collection.....	58
32.—Photos of tunnel conditions showing uneven concrete surface (top) and icy walls (bottom) due to the deterioration of the concrete.	59
33.—Photos of Reclamation personnel performing GPR surveys on the tunnel walls.	63
34.—Photos of tunnel conditions showing cobwebs across ceiling with broken up icy floor (left) and deepening standing water (right).....	63
35.—(a) GPR survey line locations (orange) in A Canal Tunnel.	64
36.—Photo of Reclamation personnel performing one of the slab-impulse response surveys within A Canal.....	65
37.—GPR line names and each profile’s depth orientation.....	68
38.—GPR profiles from Tunnel Section 11 along the North wall.	69
39.—GPR profiles from Tunnel Section 11 along the South wall.	70
40.—GPR profiles from Tunnel Section 11 along the crown.....	71
41.—GPR profiles from Tunnel Section 18 along the North wall.	72
42.—GPR profiles from Tunnel Section 18 along the South wall.	73
43.—GPR profiles from Tunnel Section 18 along the crown.....	74
44.—GPR profiles from Tunnel Section 22 along the North wall.	75
45.—GPR profiles from Tunnel Section 22 along the South wall.	76
46.—GPR profiles from Tunnel Section 22 along the crown.....	77

47.—Photo of SIR1 grid area consisting of a 5ft by 12ft grid with measurements every 1ft.	79
48.—SIR1 results from the North Wall of Section 11 where more rigid areas are colored in blue and less rigid areas are colored in red.	80
49.—Photo of SIR2 grid area consisting of a 3ft by 6ft grid and measurements every 0.5ft.	81
50.—SIR2 results from the North Wall of Section 18 where more rigid areas are colored in blue and less rigid areas are colored in red.	82
51.—Photo of SIR3 survey grid area consisting of a 5 ft by 9 ft wide grid with measurements every 0.5 ft.	83
52.—SIR3 results from the South Wall of Section 22 where more rigid areas are colored in blue and less rigid areas are colored in red.	84
53.—SIR4 results from Section 22 with GPR line locations labeled across the grid.	85

1.0 Executive Summary

The presence of voids behind a structure can limit operations at best and at worst be a precursor to failure. Voids could lead to hydraulic jacking, ground instability, and a roofed path for internal erosion processes. Any and all of these conditions could result in a failure, as seen recently at the Fort Laramie tunnel or the Oroville Dam spillway.

This report is Part 2 of a three-part series written to explore different technologies and their effectiveness for detecting voids that form in concrete infrastructure.

Report ST-2024-21045-01: Void formation has been attributed to many causes, from soil settlement and frost heave to movement of materials caused by scour processes or internal erosion. In many cases it is likely a combination of factors. Identifying the processes by which a void formed often occurs as a post-failure forensic analysis, which helps to inform future work. This report identifies geotechnical conditions and soil/rock types that may be more susceptible to void formation, elucidates on design or construction practices that have a higher probability of leading to void formation, and comments on observable indicators of void formation. The report concludes with a series of questions to help prioritize inspections from inventory-wide to structure-scale based on likely void locations.

Report ST-2024-21045-02: Detection of voids along conduits has been attempted in the past using various non-invasive technologies. While progress has been made, underlying challenges exist that have resulted in the limited adoption of these systems. Developing a set of methods and analysis techniques that can help locate voids in a variety of different mediums (concrete, metal, etc.) in a variety of different conditions (dry, wet, below/above the water table, etc.) is a valuable tool for use in facility inspections. This report details three different studies where multiple geophysical methods were deployed to detect voids at three different Reclamation facilities. Results of these methods and summary tables of their findings are included to provide guidance on future investigations.

Report ST-2024-21045-03: Determining the appropriate action to be taken after a void has been detected involves the careful consideration of many different factors. Selection of the appropriate method is always site specific. Designers must consider factors such as the type of materials used in the original design as well as common design and construction practices at the time of construction. Some other important factors include downstream impacts, extent and location of damage, size and shape of conduit or spillway adjacent to the void, type of material being eroded, size of dam, and cost of repair. This report details each of the different repair, renovation, and replacement techniques for structures associated with void formation, and provides guidance on the appropriate action to be taken.

2.0 Introduction

In its most basic form, the term "void" refers to a volume or space that is defined by a lack of physical material relative to the surrounding host medium. Voids can occur within or beneath man-made structures or within or beneath naturally occurring geologic structures or soils. They can either develop after a structure is placed (e.g., internal erosion or differential settlement), or they can be included in a structure at the time of construction or placement due to some manufacturing defect, construction error, or intentionally by design. Voids are typically either air or water/fluid filled but can sometimes be partially filled with loose (e.g., unbounded or uncemented) small clasts or anomalously low-density soils (e.g., in-filled voids in a hard structure such as concrete structures or within bedrock).

The term "void" can be used to describe several different scenarios and spatial scales relevant to infrastructure and Reclamation activities in general. For example, the term void could be used to refer to a relatively large sinkhole or sub-slab void space on the order of 10s of feet or larger, or it could refer to relatively small and subtle features such as entrapped air pockets/bubbles or small delaminations (open cracks or voids along rebar cages) in concrete structures or composite materials that are on the order of inches or millimeters in size. As a result, there are several different void detection techniques that may or may not be relevant or appropriate in each scenario.

Subsurface void and tunnel detection and imaging has been a challenging area of research in near-surface geophysics and engineering communities for more than fifty years (Greenfield et al., 1976; Belesky and Hardy, 1986; Munk and Sheets, 1997; Grandjean and Leparoux, 2004; Gelis et al., 2005; Sloan et al., 2015). Several non-invasive geophysical methods have been applied to this problem including ground penetrating radar (Hollema and Olson, 2004; Kutrubes et al., 2008; Cassidy et al., 2011; Aioke et al 2013; Hu and Li, 2020; Ortega-Ramirez, et al., 2020; Qin et al., 2020), seismic body-wave methods (Hickey et al., 2009; Peterie et al., 2009; Walters et al., 2009; Ivanov et al., 2018; Pugin et al., 2019; Peterie et al., 2020; Sloan et al., 2020), seismic surface-wave methods (Zhao and Rector, 2010; Nasseri-Moghaddam et al., 2015; Ivanov et al., 2016; Sloan et al., 2016; Schwenk et al., 2016; Ivanov et al., 2016; Ivanov et al., 2017; Ivanov et al., 2019; Morton et al., 2024), ultrasonic pulse echo (Papadakis, 1968; Akkaya et al., 2003; Hollema and Olson, 2004; Cassidy et al., 2011; Laureti et al., 2018), and electrical resistivity (Prikryl et al., 2007; Hickey, 2008; Hutchinson, 2008).

Munk and Sheets (1997) investigated the feasibility of using almost all available geophysical methods for void detection using numerical modeling and field investigations. Forward models were designed using electrical resistivity (including self-potential and very-low frequency methods), ground penetrating radar, and gravity and magnetic methods with field studies conducted using only ground penetrating radar. Most of these investigations mentioned conclude that complex near-surface geologic environments and void structures, such as their spatial characteristics and cultural noise, prevent the development of a simple and rapid method for obtaining a distinct void signature. There is no one-size-fits-all geophysical method currently suggesting the use of multiple geophysical techniques, when possible, to increase the likelihood of locating voids (Munk and Sheets, 1997).

Detection of Voids Behind Spillways, Conduits, Canals, Tunnels, and Siphons

Void detection along the inside of conduits and across concrete surfaces has been attempted using non-destructive testing techniques including active and passive thermographic techniques and the “slab impulse response” technique. While progress has been made, typical challenges associated with site conditions have prevented these approaches from being fully adopted. Therefore, the development of a rapid-deployment system that can effectively and efficiently locate voids in various mediums (concrete, metal, etc.) and conditions (dry, wet, below/above the water table, etc.) will be an invaluable tool for use in facility inspections.

Complexities in the subsurface are considered natural geologic heterogeneities such as non-uniform materials with rapid lithologic changes, fractures, or boulders. These features can appear as variations or signal disruptions with signal characteristics consistent with anthropogenic anomalies that can prevent the target of interest from being discretely interpreted (Moran and Greenfield, 1993; Grandjean and Leparoux, 2004). Signal-to-noise ratio (SNR) of a data set can also contribute to the misidentification of a tunnel signature because these geologic complexities may exhibit a SNR higher than the tunnel, making the tunnel more difficult to distinguish from the natural environment (Sloan et al., 2010). When the target of interest (i.e., the tunnel) has relatively low SNR, it can be challenging to distinguish the target from the background (i.e., natural geologic environment). The amplitude of these signals may also deteriorate as the diameter of the tunnel decreases with increasing depth (Zeng et al., 2009; Sloan, 2015) which further affects (decreases) the detectable limit of the tunnel. The presence of voids behind or below a structure can limit operations at best and at worst be a precursor to failure. Voids could lead to hydraulic jacking, ground instability, and a roofed path for internal erosion processes. All of these conditions could result in a failure, as seen recently at the Fort Laramie tunnel or the Oroville Dam spillway.

A significant amount of work has been performed on the various topics presented herein. This report is intended to provide a high-level overview of the topics as they relate directly to the problem of void detection near spillways, conduits, canals, tunnels, and siphons. A series of questions aimed at guiding the investigator towards structures (inventory-wide) and areas (structure-specific) most likely to have voids is provided to streamline detection efficiency. The reader is encouraged to review the references provided in each section for more detail on each topic.

3.0 Void Detection Methods

Table 1.—Geophysical methods used for void detection investigations

Geophysical Method	Property Measured	Failure Feature Indicators	BOR Case Studies
Ground penetrating radar (GPR)	Dielectric permittivity or impedance contrasts at material interfaces	Attenuated radar signal	Green Mountain Spillway (2011) McKay Dam (2013) Kachness Dam (2019) Oglala Spillway (2019) Hungry Horse Tunnels (2020) Merritt Dam Spillway (2020) Vallecito Dam Spillway (2020) B.F. Sisk Spillway (2021) Buffalo Bill Visitor Center (2021) Grand Coulee Dam (2021) Weber Dam Spillway (2021)
Ultrasonic pulse echo (UPE)	Acoustic-wave impedance	Reflections, refractions, and diffractions of waves off material interfaces	Elephant Butte (2022)
Seismic refraction	First arrivals of direct and refracted waves	Diffractions, layer thickness changes (e.g., thinning)	Gerber Dam (2011) El Vado Dam (2016) Lake Arrowhead, Phase II (2019) Buffalo Bill Visitor Center (2021)
Seismic surface-waves analysis	Shear-wave velocity	Changes in shear modulus within a given material layer, backscattered signal	East Canyon Dam (2014) Folsom Spillway (2020)
Electrical resistivity	Material’s resistance to flow of electrical current (electrical resistivity)	Lower or higher than expected resistivity anomaly within a given medium	Hyrum Dam (2012) El Vado Dam (2016) Folsom Mine Works (2016) Senator Wash Reservoir (2019) DSO research effort (2020)
Self-potential (electrical method)	Electrical potential	Changes in electric potential	Causey Dam (1987) Conconully Dam (1992) Hyrum Dam (2012)
Electromagnetic mapping and imaging	Material’s capability to carry flow of electrical current (electrical conductivity)	Lower or higher than expected conductivity anomaly within a given medium	Lake Arrowhead, Phase I (2019) S&T Rapid Canal Seepage (2018) Tat Momolikot Dam (2019)
Thermography	Thermal readings of a material	Temperature differential	Pipe void research effort (2008) S&T research effort (2019)

3.1 Ground Penetrating Radar

Ground penetrating radar (GPR) uses a range of different frequency electromagnetic (EM) wave pulses (a.k.a., radar waves) to image subsurface structures that are characterized by changes in dielectric permittivity. A GPR system typically consists of a transmitter and receiver antenna with a single central frequency ranging from approximately 10-3000MHz. In general, systems that are 1000MHz or greater are considered high frequency, whereas systems that are lower than 1000MHz are considered low frequency. At even higher frequencies (>3000MHz), the same physics and imaging principals are commonly employed for quality assurance within manufacturing processes and for damage/defect inspections of critical components, specifically within the automotive and aerospace industries. Here, the imaging technique is referred to as “low terahertz imaging” (Low-THz) which utilizes EM waves in the frequency ranges of 100GHz to 10s of THz (between microwave and infrared bands) to achieve extremely high-resolution imaging of materials (typically fiber reinforced composites). At this frequency range, sub-millimeter features or defects such as voids or cracks can be imaged, but the depth of investigation is typically limited to only an inch or two at best, depending on material type and electromagnetic properties.

Newer multi-frequency antenna systems allow a single GPR system to simultaneously operate and emit radar waves with more than one frequency value. This enables the operator to achieve both high spatial resolutions with the high frequency components without sacrificing depth of exploration obtained with the lower frequency components (Qin et al, 2020). Such systems can be more effective for detecting voids or other features at unknown depths. For example, Qin et al. (2020) conducted a feasibility study using a multi-frequency system (250, 500, and 1000MHz) in a shallow, 2 m-deep, test box to determine which frequency setting would optimally image different features of a concrete tunnel. Four different types of voids were simulated including (1) voids between secondary and initial lining, (2) delamination between secondary and initial linings, (3) delamination between initial lining and sand, and (4) voids buried in sand. Initial findings suggest the 1000MHz antenna could be used to characterize shallow voids in the secondary lining, but not the initial lining. The 500 MHz antenna provided optimal results of void signatures with a balanced performance between resolution and depth. The 250 MHz sensor yielded the lowest-quality results of the three frequency sensors with respect to identifying voids.

The GPR method has been successfully used for void detection investigations in natural and man-made environments (e.g., pavement, concrete) at shallow depths (<10 m). However, various GPR studies have noted that estimation of vertical void thickness remains a challenge due to radar signal attenuation (Aoike et al., 2013). The top of the void is more commonly observed as a polarity reversal in a GPR section due to the strong dielectric contrast between the void and surrounding material (Aoike et al., 2013), but the void’s host material or void structure may distort the GPR response of the bottom of the void (Hollema and Olson, 2004; Cassidy et al., 2011; Aioke et al., 2013; Diamanti and Annan, 2019). Other features that may alter the GPR response are the void’s structural support (liner or other reinforcement) and buried utilities (electrical cables or metal pipes) (Cassidy et al., 2011; Diamanti and Annan, 2019). Diffractions

are often observed in GPR sections due to the presence of rebar (Diamanti and Annan, 2019). Rebar often attenuates radar signal, reducing the likelihood that the deeper features below the rebar will be detected.

GPR data collected along a linear survey line are commonly presented as pseudo-2D sections with respect to vertical depth and horizontal distance. Data can also be collected along a 2D grid with results presented as a series of time-depth (horizontal) slices to aid investigations focused on dipping features such as fractures, cracks, and jointing features. Kutrubes et al. (2008) successfully used GPR depth-slices to determine the orientation of limestone fractures that were either water- or clay-filled features; high-amplitude features were interpreted as water-filled fractures and low-amplitude features were interpreted as clay-filled features. Ortega-Ramirez et al. (2020) also used GPR to determine the vertical extent of cracks within a 16th century altar wall. This ultra-shallow investigation used a 2600 MHz GPR antenna to successfully image a 15 cm-deep crack with total depth of investigation of 33cm and 1cm vertical resolution. Hollema and Olson (2004) collected 3D GPR across a reinforced concrete spillway using a 400 MHz antenna to detect subgrade voids ranging beneath a 6.5-13.9-inch-thick slab. Authors associated a “bright spot” in GPR results with the presence of a void beneath wet concrete; this bright spot is the result of a strong dielectric contrast between the concrete and void. Similar to other studies, the total height of the void, or depth to the bottom of the void could not be determined using GPR due to attenuated signal below the concrete-top of void interface. Attenuated signal amplitudes were also associated with the presence of voids.

Aioke et al. (2013) created a database of numerical GPR signals to archive different waveform responses from different voids. This database combined with the Signal Propagation Model Method was applied to GPR data to predict the waveform that would reflect off the top of the void, bottom of the void, and possible multiple reflections in a 1D environment to support the development of a semi-automatic detection method. These numerically simulated waveforms were then used to estimate the vertical void thickness and provide detection guidelines for future void detection investigations. Geotechnical contributors to void formation include settlement/consolidation of fill and/or the foundation material, frost heave, dispersive clays, slakeable foundation or fill materials, soluble minerals, erodibility, and internal erosion and scour.

3.1.1 BOR Case Studies using GPR

Green Mountain Spillway, Colorado (2011)

Various GPR anomalies were detected beneath the spillway floor and right approach wall. These anomalies are likely related to settling and wash out of gravel, sand, or earth fill material. Other areas of water-filled voids were detected beneath the approach channel floor. These areas of suspected voids were recommended for confirmation coring.

McKay Dam, Oregon (2013)

The upstream face of McKay Dam was surveyed to investigate potential voids beneath the upstream concrete armor due to washed out or settled foundation materials. Voids were detected using GPR, primarily near joint lines, and confirmed from 0.5 in to 2 in depth with concrete coring and video inspection.

Detection of Voids Behind Spillways, Conduits, Canals, Tunnels, and Siphons

Kachess Dam, Washington (2019)

A GPR survey was conducted across the entire length of the outlet works concrete conduit in support of an ongoing Corrective Action Study focused on internal erosion. Several anomalies were observed suggesting the location of localized voids at the concrete-soil interface along the conduit. GPR anomalies possessing high-amplitude reflections are most associated with delaminated rebar or other defect-related features within a concrete slab. These high-amplitude anomalies (e.g., “ringing” signature) can also be associated with sub-slab voids located at the concrete/soil interface. Areas “most likely” containing voids were observed near the downstream conduit entrance and at two different sections in the upstream direction, most of which correspond to a cold joint that ran the length of the conduit.

Oglala Spillway, South Dakota (2019)

A GPR survey was conducted on a 2 ft by 2 ft grid across the concrete spillway to detect sub-slab voids. Several GPR anomalies were observed consistent with the presence of a void, some appeared isolated beneath the concrete slab, while others appearing interconnected suggesting possible flow channels. Nine concrete cores were drilled to confirm the location of suspected voids as well as areas not containing voids. These cores taken at locations with and without voids were used to constrain the GPR data in order to aid GPR data re-processing, improve data interpretations, and increase confidence in results. Results were presented as a 2D map of the spillway.

Hungry Horse Tunnels, Montana (2020)

Linear GPR anomalies were detected and interpreted as wood timber-lined tunnels located beneath the ground surface and vehicle storage buildings. Based on the anomaly signature, these tunnels were likely partially or completely collapsed and later backfilled. It is believed that these tunnels were not completely backfilled and the backfill material likely settled leaving the air-filled voids detected during this work. Depth to GPR anomalies suspected to be the top of air-filled voids ranged from 4-12 ft deep.

Merritt Dam Spillway, Nebraska (2020)

GPR surveys were conducted across the Merritt Dam Spillway to detect anomalous zones that may be indicative of sub-slab voids. Several areas exhibited high-amplitude GPR anomalies and some ringing features that are often associated with the presence of sub-slab voids. Signal ringing occurs when GPR signal reverberates between two reflectors (e.g., two high-contrast boundaries such as the top and bottom of a void). No confirmation drilling was conducted to verify the results of this work.

Vallecito Dam Spillway, Colorado (2020)

GPR data sets were collected in support of an issue evaluation related to visible damage within the concrete spillway floor slabs. Such damage features include holes, spalling and delamination, positive pressure seepage with piping of fine materials out of pressure relief valves, and concrete slab control joints. An objective of this study was to assess the spillway floor slab and sub-slab conditions and identify potential seepage pathways. Numerous GPR anomalies were observed during this study that were indicative of sub-slab voids and other possible concrete damage/delaminations. It was noted that damaged concrete and delaminations can exhibit similar signatures in GPR data (i.e., high-amplitude ringing) where the primary way to differentiate them is determining the depth at which the feature originates. Differentiating between these features is

challenging from 2D GPR cross sections alone. This study noted that control joints are often associated with high amplitude ringing regardless of damage along such areas. An interesting observation of this study was an apparent sinuous and continuous feature that extended more than 5 ft wide in some areas that eventually bifurcated from the left to right wall from upstream to downstream. This feature was suspected to be a concentrated seepage pathway beneath the spillway floor.

B.F. Sisk Spillway, California (2021)

Multiple 3D GPR surveys were conducted along the vertical portion of the morning glory spillway intake structure as well as downstream to detect potential voids behind the walls of the concrete structure. An asymmetric linear anomaly was observed below the horizontal section of the right abutment springline. This suggests the presence of a water-filled void behind the concrete wall where the concrete angle changes rather than overlapping steel rebar cages. Concrete coring was recommended to confirm the presence of water-filled voids. An interesting observation from this study is the difference between GPR anomalies observed along flat and non-flat sections. It is important to consider the shape of the surveyed surface (e.g., inside surface of a cylinder/conduit wall) during data interpretation because these curved areas will cause out of plane effects on the GPR signal, which can cause hyperbola reflections to appear as broader reflection features, rather than a point reflector.

Buffalo Bill Dam, Wyoming (2021)

3D GPR surveys and 2D p-wave seismic refraction surveys were conducted in support of an ongoing construction design feasibility study. The goal of these geophysical surveys was to identify subsurface voids and/or low-velocity zones within the overburden materials that may be contributing to identified slope stability issues. In the GPR results, joints and fractures were identified based on the presence of strong reflection horizons below the interpreted top-of-bedrock interface. The observed dip of interpreted joints/fractures is generally consistent with those observed within bedrock outcrops to the north of the project area.

Grand Coulee Dam, Washington (2021)

3D GPR data were collected in support of assessment of visible damage to concrete on the west facing exterior façade of the Left Powerhouse and immediate vicinity of the interior 350-ton overhead crane rails and crane stop. Damage features of interest were cracks and delaminations observed at the exposed slab surface; GPR surveys were aimed to determine whether these damage features were surficial or penetrated deeper into the slab. In this study, five different classifications of damage features were identified including: (1) interpreted delamination along vertical cracks observed on an exterior wall, (2) possible aggregate disbonding within interior of concrete features, (3) other discrete points of concrete damage at depth, (4) possible rebar delamination or other concrete damage at depth, and (5) main visible delamination features. Although evidence of delamination and cracking were observed at the slab surface, GPR results did not detect any anomalies that indicate damage extends deeper into the concrete or beyond the shallow (exterior) rebar cage.

Weber Dam Spillway, Nevada (2021)

3D GPR surveys were conducted along the spillway floor and walls to assess floor slab and sub-slab conditions related to seepage and movement of fine-grained soils. The most significant anomalies that are potentially related to sub-slab voids are near the radial gates behind the left

and right walls, though investigators do not have high confidence that these anomalies are representative of voids. This is due to minimal levels of anomalous nature of identified data patterns and limited or no spatial continuity in these features across scan lines.

3.2 Ultrasonic Pulse Echo

The ultrasonic pulse echo (UPE) method is a well-established acoustic testing/imaging method that uses acoustic waves (compressional waves are more commonly used than shear waves) to delineate and image structural features in concrete and other media (e.g., composite structures, rock, metal, plastics, etc.); one of the earliest applications of UPE is documented by Papadakis (1968). Features are interpreted based on reflections, refractions, and diffractions of waves off material interfaces such as a void boundary or change in material stiffness (Akkaya et al., 2003). Other applications of UPE include determining the water-to-concrete ratio, monitoring hardening, damage detection, and determining the structural health of reinforcement bars within concrete structures (Laureti et al., 2018). One challenge encountered with the UPE method is that only one side of a target structure is typically available for surveying, which limits the investigation of failure features. This method is often coupled with GPR surveys to verify results of detected features in subgrade concrete and other materials. Cassidy et al. (2011) conducted a feasibility study to compare the effectiveness of using GPR and UPE methods for a shallow void detection investigation. Overall findings of that 2D and 3D study was that the UPE system performed as equally well as the GPR method. A high-amplitude contrast was observed in results from both methods between the top of the void/bottom of the slab and the background material.

Several studies have highlighted UPE as a method that can overcome some of the GPR method's inherent limitations such as imaging below dense rebar meshes (Cassidy et al., 2011). UPE has been used to evaluate the flexibility and stiffness of a subgrade system where features possessing high flexibility and low stiffness can be associated with voids (Hollema and Olson, 2004). However, the UPE system has not yet been used to successfully estimate void height (Hollema and Olson, 2004). Overall, the UPE method has proven to work well for void detection investigations within uniform concrete subgrades where the surveyed surface of the concrete is relatively unweathered; unweathered surfaces allow optimal coupling of ultrasonic waves (Cassidy et al., 2011).

3.2.1 BOR Case Study Using UPE

Elephant Butte Dam, New Mexico (2022):

A series of UPE line scans were conducted using a handheld system to detect the lateral extent of the void beneath the historic restaurant patio above the reservoir. A GPR survey was performed first to help determine where to place this UPE study. As a result, a void was detected beneath the patio slab and across the length of most 14.5ft-long UPE line scans. High amplitude signatures were present and were likely associated with taller void spaces. It is important to note that the height of a void cannot be determined from UPE survey data because seismic shear-waves cannot propagate through fluids (e.g., air- and water-filled voids). Instead, these

data sets were used to detect the depth to the top of a void, which was approximately 5in, or 12.7cm. At the end of one survey line, a narrow section with lower amplitude was observed suggesting the absence of void space immediately below this portion of the patio slab.

3.3 Seismic Methods

Seismic methods have proven successful at detecting voids as small as 1-2 meters in diameter either directly or indirectly (Nasseri-Moghaddam et al., 2005; Sloan et al., 2015; Schwenk et al., 2016). Disturbances or changes in the material surrounding the void rather than the void itself are the indirect signatures observed most often (Belesky and Hardy, 1986; Ivanov et al., 2013). Proven and reliable seismic methods for capturing void signatures primarily include diffraction imaging (Xia et al., 2007; Sloan et al., 2013a; Peterie and Miller, 2015; Peterie et al., 2020) and backscatter analysis of surface waves (BASW) (Ivanov et al., 2003; Sloan et al., 2010; Sloan et al., 2015; Schwenk et al., 2014; Schwenk et al., 2016). Other seismic techniques applied to void detection include refraction tomography (Belfer et al., 1998; Wright et al., 2000), reflection (Inazaki et al., 2005; Llopis et al., 2005), borehole tomography (Shustak et al., 2015), and surface-wave attenuation (Nasseri-Moghaddam et al., 2005; Sherman et al., 2014).

Seismic methods have been favorable for larger-scale void detection efforts because data acquisition can be performed over large volumes with minimal ground footprint (Steeple, 2001). This concept has been enhanced with the development of towed arrays and land streamer technology which allow seismic surveys to be performed rapidly and continuously (Miller et al., 2003; Inazaki et al., 2005; Sloan et al., 2011; Buckley and Lane, 2012; Schwenk et al., 2016) while maintaining data quality consistent with fixed array methods (Suarez and Stewart, 2008).

Similar to GPR, resolution of the available data and processing algorithms can make void detection more challenging. For example, Sheehan et al. (2005) showed that the seismic result may smear the boundary between the void and surrounding material even though the actual seismic velocity contrast may be abrupt. This smearing effect may be associated with the resolution of the recorded available seismic wave and/or with the regularization algorithms used during inverse modeling for estimating seismic velocity. Smooth model regularization algorithms assume that the subsurface properties vary relatively slowly and continuously, resulting in sharp physical boundaries being smeared or blurred into a gradient. Other regularization approaches such as the L1-norm promote abrupt boundaries in model parameterization (i.e., model roughness).

With seismic techniques, there is still an inherent loss of sensitivity and resolution in the vicinity of voids, mainly because seismic waves will generally propagate around a void rather than through a void. To overcome this limitation, Hickey et al. (2009) suggested using ray path density maps, rather than velocity tomograms, to determine the void location more accurately. Hickey et al. (2009) and Sheehan et al. (2005) associated areas with low ray coverage as void signatures rather than low-velocity signatures. In the case of arrival-time analysis techniques, such as seismic refraction velocity tomography, the first arrival of seismic energy will almost always have propagated around a void space, and so any detected velocity decrease in the vicinity of a void is generally due to a longer wave propagation path between source and receiver

Detection of Voids Behind Spillways, Conduits, Canals, Tunnels, and Siphons

(i.e., a seismic ray path is longer due to the added segment required to circumnavigate the void space). In more recent studies, the use of joint inversion has been used to help improve seismic velocity tomograms and void-related low velocity anomalies (Rittgers, et al., 2015).

In some cases, this concept has been taken advantage of in relatively simple void detection seismic surveys, where seismic “fan shots” are implemented to detect azimuthal directions from a source point where propagation time is anomalously longer (increased propagation pathway detected by arrival times). Here, a seismic source is placed at one location, and an array of seismic sensors (e.g., geophones) are placed in a circle or semi-circle centered around the source point. Assumptions made with this technique include that the subsurface is laterally homogeneous and any geologic layers are horizontal such that any delayed arrival times are due to the presence of a void space at some azimuth. If detected, the location of the void can then be refined by moving the survey geometry and performing triangulation. However, to further complicate things, the annulus of materials surrounding a void space can exhibit both lower velocities (e.g., decompression of soils beside and below a void) and higher velocities (stress field arching above and adjacent to a void space).

Although spectral analysis of surface waves (SASW) and multichannel, high-frequency, surface-wave techniques such as multi-channel analysis of surface waves (MASW) can provide reliable S-wave velocities in different geological settings, they are not suitable for detecting voids directly based on anomalies of the S-wave velocity because of limitations on the resolution of S-wave velocity profiles inverted from surface-wave phase velocities (Xia et al., 2008). Alternatively, the backscatter analysis of surface waves (BASW) method has proven to be a more reliable void detection method (Schwenk et al. 2016). This method can be used to determine the location of vertical void boundaries as well as the depth to the top of the void (Ivanov et al., 2016), but backscatter sections do not provide image outlines of voids or other targets. BASW is primarily used to estimate the lateral location of a void based on what station number or trace number the backscatter feature crosses time-zero (Sloan et al., 2016; Ivanov et al. 2019). The depth of the backscatter feature is estimated by displaying the backscatter section as a frequency-amplitude plot to extract the dominant frequency of the high-amplitude feature. Using the equation $\text{wavelength} = \text{velocity}/\text{frequency}$, the dominant frequency of the backscatter and corresponding velocity (from the dispersion curve used for BASW processing during the linear moveout correction) yields a wavelength of the backscatter feature. Depth of the backscatter feature can then be estimated using the half wavelength rule.

Surface-wave attenuation analysis has also been used to support void detection studies (Nasseri-Moghaddam et al., 2005). Nasseri-Moghaddam et al. (2005) observed changes in surface-wave attenuation that suggest time and frequency domain parameters are sensitive to the location, size of the void, and embedment depth (depth to top of void). When a propagating surface wave interacts with a void, the void boundary surface-wave will scatter, leading to a strong attenuation and amplification of surface-wave energy at that boundary interface. The attenuation analysis of Rayleigh waves method (AARW) evaluates the frequency spectra of recorded surface waves to compute the spectral-energy parameter and a modified logarithmic-decrement parameter. Embedment depth is estimated using this decrement parameter, but it's important to note that depth estimation error also increases with depth. Other

studies (Morton et al., 2016) have suggested the use surface-wave attenuation as a void detection method, but more research is required to accurately detect voids outside controlled environments without knowledge of the void's location.

Ivanov et al. (2019) and Sloan et al. (2020) have observed ringing features on seismic records and suggest such anomalies are the result of trapped seismic energy in air-filled voids causing reverberations. Ivanov et al. (2019) used the frequency of the ringing feature from amplitude-frequency trace plots to estimate the embedment depth of the void. Sloan et al. (2020) did not initially observe this seismic resonance until after applying AGC and a narrow-frequency band bandpass filter. The lateral location, or station location, of the apex of the ringing corresponded to the lateral location of the void. It may be important to note that the void studied in both Ivanov et al. (2019) and Sloan et al. (2020) was an elongated, wood-frame-reinforced tunnel.

Another promising seismic void detection method is body-wave diffraction imaging, also known as diffraction enhancement (Peterie et al., 2009; Peterie and Miller, 2015; Peterie et al., 2020). In general, diffraction imaging is conducted by applying a Kirchoff migration to seismic reflection data sets to generate a cross section where a diffracted signal is focused at the lateral location of the diffracting object with respect to two-way traveltime (Peterie et al., 2020). Diffraction imaging has been commonly used to detect fault and fracture features that are smaller than the seismic wavelength (Khaidukov et al., 2004; Peterie et al., 2020). Such void features cause seismic waves to scatter as diffracted body waves upon interaction with the heterogeneity. Peterie et al. (2020) conducted 9C seismic modeling to analyze diffraction modes from pure P-wave, pure S-wave, mode-converted P- to S-wave, and S- to P-wave. Results from this work indicate that SH-wave diffraction yielded the largest amplitude void signature with coherent phase characteristics at a lateral location consistent with the surveyed void. The conventional P-wave diffraction signature exhibited low amplitudes relative to the background environment. Pugin et al. (2019) also noted increased diffraction-amplitude anomalies in SH-wave data sets during a shallow void investigation.

Other techniques for carrying out seismic surveys can have varying levels of success in void detection, including cross-hole seismic profiling and tomography imaging, surface-to-downhole vertical seismic profiling (VSP), seismic reflection surveys, and downhole sonic logging surveys. Similar to refraction surveying, cross-hole surveys depend on a sudden or anomalous decrease in the measured/calculated seismic wave propagation velocity that results from longer wave propagation pathways around a void space. For surface-to-downhole VSP surveying, void detection generally requires that the well intercepts a void space, or a laterally semi-continuous void space is located between the source (on the ground surface at some distance typically a few 10s of feet away from the top of the borehole) and receiver (down hole). For seismic reflection surveys, a void space at depth must be adequately large in its horizontal dimensions so that the relatively low-frequency body waves and correspondingly larger wavelengths (on the order of 10s of feet) will interact with and reflect off the void. For downhole logging surveys, the void space needs to be within a relatively close radial distance (approximately <2ft) from the borehole being logged, so that the seismic energy emanating from and refracting back to the borehole at a given depth interacts and “senses” the void space (also manifests as a decrease in measured velocity related to increased body-wave propagation pathways between source and receiver). In

all cases, the survey geometry deployed, including source and receiver spacings and their positions relative to a target void feature, are key factors in the success of detecting a void with any seismic technique.

3.3.1 BOR Case Studies Using Seismic Methods

East Canyon Dam, Utah (2014)

Seismic surface-wave surveys (SASW) were conducted in support of an ongoing crack investigation along the downstream face of East Canyon Dam. These 1D measurements were performed to identify zones possessing relatively low shear-wave velocity, or reduced shear strength, as a tool for mapping cracked or damaged concrete to a depth of 9 ft. Zones of relatively low shear-wave velocity are characterized as sections of concrete having values less than 6500 ft/sec. Concrete quality is classified by three shear-wave velocity ranges including: 0-5500 ft/s or severely damaged concrete, 5500-6500 ft/s or damaged concrete, and >6500 ft/s or competent/undamaged concrete. Control measurements of s-wave velocity were taken as reference points at areas where the competency of good-quality concrete was known, averaging approximately 8000 ft/s.

Folsom Dam, California (2020)

Seismic surface-wave surveys (SASW) were performed on the Folsom auxiliary spillway floor to detect cracks within three of the spillway slab-sections. S-wave velocity values are used to interpret the physical orientation and depth characteristics of observed cracks within the concrete slab. Control measurements of s-wave velocity were taken to a depth of 28 inches as reference points at areas where the competency of good-quality concrete was known (2200 to 2400 m/s). Cracks (voids) in the concrete were defined based on the following characteristics: non-cracked concrete possessed s-wave velocity from 2200 to 2400 m/s; vertically cracked concrete possessed s-wave velocity 0 to 2000 m/s that did not increase with increasing depth; horizontally cracked concrete possessed sharp drops in s-wave velocity over a short distance that did increase with increasing depth.

Gerber Dam, Oregon (2011)

Seismic refraction surveys were conducted to map the extent of concrete deterioration caused by freeze-thaw damage based on changes in p-wave velocity. Survey locations included both the vertical faces of the upstream and downstream side of the dam as well as horizontally across the right closing plug and contraction joint. Survey results indicated concrete deterioration from 1 to 4 ft deep on the dam crest with deeper deterioration on the left side of the dam based on decreased p-wave velocity anomalies (e.g., 8 to 10 kft/s compared to 14kft/s). Although cracks were observed on the vertical faces of the structure, seismic results did not provide indications of decreased velocities beneath these areas.

El Vado Dam, New Mexico (2016)

A combination of s-wave seismic refraction and ER surveys were conducted to characterize areas within El Vado Dam that potentially contain void-like features and better understand

seepage pathways from the upstream left abutment to the downstream toe. Seepage pathways were interpreted based on low s-wave velocity anomalies that were co-incident with low-resistivity anomalies observed in a similar location.

Lake Arrowhead IPR Mountain Ponds, Phase II, California (2019)

S-wave seismic refraction and ER surveys were conducted in support of an ongoing multi-phased feasibility study focused on evaluating the hydrogeologic and bedrock conditions. Seismic results were used to identify areas of extremely weathered and/or fractured bedrock. Such features were interpreted based on the presence of lower velocities where natural drainage may be taking place and carrying groundwater downhill. This interpretation is supported by anomalous regions of low resistivity (e.g., partially or full saturated zones) in a similar location. These co-located anomalies suggest the presence of preferentially fractured zones of bedrock with potentially elevated hydraulic permeability. The locations of anomalous zones were suggested as potential drillhole locations.

Buffalo Bill Dam, Wyoming (2021)

2D p-wave seismic refraction surveys and 3D GPR surveys were conducted in support of an ongoing construction design feasibility study. The goal of these geophysical surveys was to identify subsurface voids and/or low-velocity zones within the overburden materials that may be contributing to identified slope stability issues. In the seismic results, regions of low velocity were observed in a location consistent with anomalously low standard penetration blow-counts where small voids were encountered. These low-velocity regions of overburden material are likely the most susceptible to differential settlements, wave erosion processes, and slope stability issues.

3.4 Electrical Methods

Electrical resistivity methods apply electric current into the ground surface and the potential difference is measured between two lateral locations. Measured changes in potential then provide indications of subsurface structure and material properties. Materials that allow electric current to flow more easily are considered less resistive (more conductive) than materials that reduce the flow of current. Electrical resistivity surveys are commonly used in hydrogeologic investigations to track fluid flow where seepage paths (e.g., fractures, faults, or any other fluid pathway) may not be known. Hutchinson (2008) collected vertical electrical soundings to image subsurface haulways and rooms related to a deep, abandoned clay mine. Perpendicular electrode arrays were used to approximate the orientation of the haulways and results were used to determine that these voids were 35-50 ft below the ground surface. Hickey (2012) conducted time-lapse ER surveys over two years under different reservoir conditions to evaluate potential seepage pathways and how these features are affected by weather. In this work, Hickey (2012) characterized an erosion channel as a high-resistivity anomaly unlike a natural water channel, which possesses a more diffuse lower-resistivity anomaly.

Prikryl et al. (2007) also used ER surveys to map the location of karst voids below 30 m depth with openings as wide as 4 m. Karst features are characteristically complex due to rapid changes in material properties, depth, fill material, and the spatial distribution of those features.

Therefore, choosing the proper array or electrode configuration is a crucial step to accurately detect these features. For example, Prikryl et al. (2007) observed that the dipole-dipole array yielded results down to 12.1 m depth and the pole-dipole array yielded 25.7 m depth. The pole-dipole array offered higher signal strength and greater depth of investigation compared to the dipole-dipole array, but also found that the pole-dipole array was more sensitive to telluric current and cultural interference (e.g., powerlines, traffic noise).

The self-potential (SP) or spontaneous potential method is another electrical surveying method used for detecting electrical anomalies in the subsurface, primarily for mineral exploration and groundwater investigations. More specifically, SP surveys can be used to detect groundwater flows and contaminant plumes, as well as estimating hydraulic properties of aquifers (Jouniaux et al., 2009). It is a passive electrical geophysical method that measures the natural or spontaneous electrical potential due to electrochemical interactions between minerals and fluids, electrokinetic processes resulting from the flow of ionic fluids, or thermoelectric mechanisms from changes in temperature in the subsurface. Some limitations of the SP method are the prevalence of SP noise sources that readily interfere with recording higher-quality data and make interpretation more challenging. These noise sources include telluric currents, electrode drift, topographic effects related to streaming potentials, photovoltaic potentials, and changes in soil composition, moisture, and vegetative cover (Nyquist and Corry, 2012).

3.4.1 BOR Case Studies Using Electrical Methods

Causey Dam, Utah (1987)

Self-potential surveys were conducted in support of a seepage investigation. Three areas of seepage were interpreted related to seepage inflow south of the grouted area of the dam. Another seepage path was also observed from the seepage inflow area to the outflow area. SP anomalies followed a general pattern such that a relatively negative SP region was present at the seepage inlet area, a relatively positive SP region was present at the seepage outlet area, and a transition from more negative SP values to more positive SP values were observed in the direct of flow along the interpreted seepage path. In general, SP contours were orthogonal to the seepage flow path and flow direction went from negative to positive SP contours. Investigators suspect that topography, low water, and outlet works may have influenced SP results in other areas and could not confidently interpret other SP anomalies. They suggested repeating these surveys during low-pool conditions to improve the interpretation of SP effects and the outlet works based on the assumption that low seepage would coincide with low pool levels, but a continuing effect would be indicative of the outlet works and/or topography.

Conconully Dam, Washington (1992)

Investigators identified the self-potential method as the optimal method for detecting seepage at high pool based on positive, long-wavelength, and relatively low-amplitude SP anomalies near the embankment/foundation and berm/foundation contact. Dipole-dipole ERT surveys were used to delineate the subsurface geologic conditions at the embankment/foundation contact. These ERT surveys suggest the presence of fluviolacustine (heterogeneous) materials with high porosity and medium average grain size combined with saturated conditions are conducive to seepage at this embankment/foundation contact.

Hyrum Dam, Utah (2012)

ER and self-potential surveys were performed to detect areas of seepage and internal erosion within or beneath the embankment dam. It was suspected that areas of internal erosion could be characterized by variations in construction material composition. Results of geophysical surveys indicated the possibility of incomplete excavation of the river channel beneath the dam prior to placing the embankment. Areas possessing higher electrical potentials were observed with SP surveys, likely due to increased fluid flow through the river channel and surrounding material. If this increased fluid flow was not occurring, the expected SP response and distribution of electrical potential would resemble the hydraulic head distribution within the embankment. Areas with anomalously high resistivity were also observed in locations consistent with the SP surveys and suspected river channel (near the embankment/foundation contact). This observed channel is suspected to be a conduit for internal erosion and/or concentrated seepage.

El Vado Dam, New Mexico (2016)

A combination of s-wave seismic refraction and ER surveys were conducted to characterize areas within El Vado Dam that potentially contain void-like features and better understand seepage pathways from the upstream left abutment to the downstream toe. From ER tomograms, seven main seepage outlets that were observed near the downstream powerhouse were traced back to their respective upstream source area based on observed low-resistivity anomalies that were co-incident with low s-wave velocity anomalies observed in a similar location. Seepage pathways and void-like features were observed within the displaced Dakota Sandstone unit which is characterized as highly jointed/fractured.

Folsom Mine Works, California (2016)

ER surveys were conducted upstream of Dike #4 to detect air-filled or water-filled mine-related features varying from 5 to 8 ft wide and 20 to 30 ft deep. Interpretation of resistivity anomalies were based on five parameters: (1) measured resistivity versus background resistivity, (2) general data quality, (3) resistivity anomaly shape, (4) proximity to adjacent anomalies, and (5) resistivity depth below ground surface. Nine resistivity anomalies were considered “high risk” representing areas of subsidence, with some anomalies located in an area where surface subsidence was also observed.

Senator Wash Reservoir, California (2019)

A series of ER surveys were conducted using dipole-dipole and strong gradient array configurations to delineate possible piping and sediment transport along seepage pathways that exit near the dam toe. As a result, zones possessing low resistivity anomalies were observed beneath or within West Squaw Lake Dike and Senator Wash Dam. These anomalies are attributed to areas of elevated moisture content which support seepage. Results also suggest seepage is occurring through fractured volcanic rock units at the north and south abutments, which is supported by observations of increased soil moisture and salt accumulations near the left abutment toe and accumulation of standing water downstream from the right abutment.

Dam Safety Technology Development Program, Denver Federal Center (2020)

A Phase II research study was developed to test the feasibility of using time-lapse ER surveys to detect and monitor the progression of erosion and subsequent changes in void volume over time. Phase I included using ER to identify the location and volume of marble blocks stacked in various configurations within a water-filled box. Seven “snapshots” of ER data using

64 electrodes were collected and processed to show the evolution of erosion along a transverse crack in a laboratory test box (87% silt material with 85-90% maximum proctor density and 3-4% optimum water content). Primary findings of this work show success in using ER to identify areas of erosion but determining the true boundary between the water-filled void (due to erosion) and the remaining embankment proved challenging. It was noted that electrode spacing was likely too large relative to the size of the voids that formed. The test box used in this study was dismantled and is no longer available for future experiments. Various suggestions for future investigations include using different soil types or a zone embankment, using saturated material, conducting an initial ER survey to establish baseline conditions before experimental testing, photogrammetry for estimating embankment volume changes, and conducting additional GPR surveys to corroborate ER data sets.

3.5 Electromagnetics (EM)

EM methods are used to measure electrical properties of the subsurface by producing a primary EM field and passing alternating current through a coil. If a conducting body is present in the subsurface, a secondary EM field will be generated and detected by a receiver coil. The difference between this primary and secondary field is used to evaluate characteristics of these conducting bodies in the subsurface. This method can be conducted in either the time-domain (TDEM) or frequency-domain (FDEM). In TDEM, the conductivity of soil and rock materials are induced by pulsating currents into the ground using a transmitting coil and monitoring the decay of that signal over time with a separate receiver coil (Munk and Sheets, 1997). In FDEM, the magnitude and phase of an induced EM current are measured as the conductivity of underlying soil and rock materials are altered by the induced EM current.

EM surveys can be conducted along 2D survey profiles (e.g., independent dataset collected along a single path) or in a pseudo-3D mapping fashion (e.g., across a grid of overlapping X and Y-oriented survey lines). FDEM data are then post-processed, filtered, and plotted as either line graphs or contour plots to indicate the average electrical conductivity of the subsurface. EM surveys lack the resolution of ERT surveys but can be conducted more rapidly over greater volumes of space without the need to deploy multiple sensors across that given volume (Munk and Sheets, 1997). The effective detection depth is dependent on the electrical properties of earth materials, the frequency of EM waves, and the spacing between the transmitter and receiver coils (Keller and Frischknecht, 1966; Munk and Sheets, 1997).

3.5.1 BOR Case Studies Using EM Methods

Lake Arrowhead IPR Mountain Recharge Ponds, Phase I, California (2017)

FDEM surveys were conducted throughout the IPR mountain recharge ponds study area in support of a multi-phased feasibility study focused on evaluating the hydrogeologic and bedrock conditions. More specifically, investigators were interested in evaluating the hydrogeologic properties of the primary and secondary fracture networks and how it relates to infiltration, temporary storage, and recycled water recovery. EM34 data sets were used to identify linear trends of higher apparent conductivity that would indicate the location or orientation of elevated

fracture density and support preferential flow paths. As a result, three primary trends were identified that appear to converge downhill of the ponds where naturally occurring drainages/watersheds are also located. These three trends are likely the result of elevated fracture density and/or intersecting and converging fracture sets that created preferential flow paths and subsequently eroded the underlying bedrock. The convergence point of these three trends intersects with Willow Creek, which was labeled as a potential location to place recovery wells, but additional testing is required to further verify these results.

S&T Rapid Canal Seepage (2018)

This Science and Technology research project provided a foundation for seepage detection and general embankment health assessment with the integration of geophysical profiling and satellite remote sensing data analysis. A frequency-domain electromagnetic (FDEM) system towed behind an all-terrain vehicle was evaluated for feasibility of rapid data acquisition along canal embankments. These data sets were combined with remote sensing imagery (NVDI) to develop a robust, semi-automated approach for detecting and mapping seepage at four different test locations. FDEM systems tested during this research effort were: (1) GSSI Inc.'s EMP-400 (multi-frequency, fixed coil-spacing), (2) DualEM Inc.'s DualEM-2 (single-frequency, fixed coil-spacing), (3) Geonics Ltd's EM31-mk2 (single-frequency, fixed coil spacing), (4) Geonics Ltd's EM34-mk2 with 10m coil separation (single-frequency, variable coil spacing), and (5) Geonics Ltd's EM38-mk2 (single-frequency, two fixed coil spacings).

Tat Momolikot Dam, Arizona (2019)

EM31 and EM34 surveys (and ERT surveys) were conducted across the crest, upstream face, and downstream face of the dam to detect any features that may be indicative of open-air cracks or other signs of differential settlement. It is believed there is a sand filter that may have caused a trench to start forming directly above the downstream face as a result of earthfill materials sloughing and settling. Collecting the EM34 data sets were more challenging than the EM31 surveys because two people were required to operate the EM34 system which created more variable separations between the transmitter and receiver antennae on the rough surface of the upstream and downstream faces. Shallow, low-conductivity anomalies were interpreted along the upstream face off the crest road on EM31 and EM34 results, which correlate to deeper ERT resistivity anomalies. These anomalies were categorized as either a surficial resistive anomaly, core (of the dam) resistive anomaly, or both; note that high-resistivity corresponds to low-conductivity. Additional anomalous zones were identified as being related to potential high rates of seepage. All anomalies were recommended for in situ testing and confirming drilling.

3.6 Thermography

Thermography, or thermal imaging by way of emitted electromagnetic waves, measures infrared radiation emitted by materials and converts it into an image that can be used to detect changes in temperature. It can be used to identify malfunctioning electrical systems due to overheating or circuit overloading, heat loss within an insulated system, structural defects in man-made materials, water leaks, or other activities that emit anomalous thermal patterns. All objects above absolute zero temperature emit thermal radiation. Although these signals are invisible to the human eye, they can be converted into a thermal image (e.g., heat map) where warmer areas are represented by red and orange colors and cooler areas are represented by blues. Thermography

can be measured actively or passively, depending on whether a heat source is being applied to the imaged material (active) or the thermal emissions being recorded are naturally emitted by the imaged material (passive).

3.6.1 BOR Case Studies Using Thermography

Pipe Void Experiment, Denver Federal Center (2008)

A model was constructed to simulate and monitor the development of voids surrounding an underground spiral rib corrugated steel pipe (CSP) placed in soil. A FLIR Systems™ ThermaCAM™ P60 camera with a 65-degree wide-angle lens was used to image changes in temperature related to water flowing through a developing water-filled void. Initial testing revealed the surface of the CSP to be very reflective making it difficult to obtain absolute temperature values due to a very low emissivity of the CSP surface. The emissivity of an object refers to the amount of infrared radiation it emits compared to that of a blackbody (a blackbody is a perfect emitter and does not reflect any infrared radiation). Objects with low emissivities reflect more and emit less infrared radiation making it difficult to distinguish temperature variances. Conduits considered for real-world monitoring scenarios typically have scale buildup around the inner circumference of the pipe which tends to be more flat than reflective (higher emissivity). To simulate this type of surface and reduce the reflectivity of the CSP, the CSP was painted with flat black primer paint. As a result, IR thermography proved a useful tool for detecting voids behind CSP surrounded by compacted soil. Some cases provided very distinct pictures allowing for easily located voids. Other cases were less distinct; however, the water- and air-filled voids could still be located.

S&T Research Effort, Denver Federal Center (2020)

A feasibility study was designed to assess new technologies that could rapidly identify and characterize concrete defects, damage, and other types of deterioration in a more efficient and spatially comprehensive way than current technologies. As a result, experiments using active thermography techniques provided promising results when used to assess aging concrete structures. A major limitation of this method is the lack of depth of investigation. This method is often limited to the upper 10-15 cm of a material surface thus preventing deeper investigations. A challenge associated with active thermography is the logistics involved with applying heat to large structures during imaging. This requires direct access and physical contact with the target surface, which may not always be safely accessible or feasible. Investigators also found that spatial resolution of results decreases with increasing distance from the target surface, therefore requiring closer contact with that surface. Another concern for data reliability is air temperature fluctuations and how those changes affect thermal pulse readings from day to nighttime recordings.

4.0 Field Experiments

A series of field experiments at three different facilities were carried out to determine which method, or combination of methods, were suitable for detecting voids. These experiments are summarized in table 2.

Table 2.—Field experiments summary

	Location	Methodology
Experiment 1	Glendo Powerplant, Wyoming	Slab impulse response (SIR) Ultrasonic pulse echo (UPE)
Experiment 2	Denver Federal Center, Colorado	Ground penetrating radar (GPR) Impact echo (IE) Thermography (FLIR)
Experiment 3	A Canal Tunnel, Oregon	Ground penetrating radar (GPR) Slab impulse response (SIR)

4.1 Experiment 1: Glendo Powerplant

4.1.1 Background

The Glendo Dam Powerplant is located on the North Platte River in east-central Wyoming, approximately 4.5 miles southeast of Glendo, WY. This powerplant contains two units having an installed capacity of 19,000 kilowatts each which increases available power in the basin by approximately 500 million kilowatt-hours each year. The Wyoming Area Office (WAO) currently manages the facility’s water storage, drainage, recreation, and fish and wildlife enhancement for flood control and power production.

The current detection method for such applications is the “sounding” process which uses a mechanics hammer to map areas with apparent hollowness based on the sound of the impact. Geophysical surveys were requested to provide a more quantitative or qualitative void detection procedure in this steel-concrete environment. Therefore, three methodologies were considered for this work including the slab impulse response (SIR), impact echo (IE), and ultrasonic pulse echo (UPE) methods. Ground penetrating radar was not considered because the metal (i.e., steel) liner would reflect all emitted electromagnetic waves, preventing detection of any features beneath the liner. The IE instrument was determined to be unsuitable for this project due to the varying thickness of the concrete draft tube foundation. IE data analysis uses the thickness of the test material to determine whether voids are present. Since the circular draft tube resides in a rectangular concrete base, the resonance frequency and concrete thickness would vary greatly across the tube wall thus making data analysis more challenging and less feasible.

Results of this work are archived in Technical Memorandum No. 86-68320-2023-14.

4.1.2 Methodology

4.1.2.1 Slap Impulse Response

The slab impulse response method is designed to detect voids beneath concrete slabs as well as areas with delamination if the damage is relatively shallow. It is considered a non-invasive and non-destructive testing method that utilizes a modified hammer to generate acoustic waves at multiple, densely spaced locations. The velocity of these acoustic waves from the hammer

Detection of Voids Behind Spillways, Conduits, Canals, Tunnels, and Siphons

impacts are measured using a transducer, such as a vertical-component geophone or Wilcoxon vibration sensor, that is pressed firmly on the test surface (i.e., steel liner for this project). SIR is typically used on concrete slabs and retaining walls, pavement, runways, spillways, and tunnel liners.

These measurements are first plotted in the time domain as a function of wave amplitude to assess data quality. Multiple impacts can be performed at each grid location and stacked to improve signal quality and decrease noise. Once a stacked record is deemed acceptable, the velocity measurement is converted to the frequency domain to estimate the material's average mobility (velocity/force) and flexibility (displacement/force) at each point location.

In general, areas possessing low mobility and low flexibility qualitatively suggest the material is more rigid and well supported (e.g., minimal to no delamination present) compared to areas possessing relatively high mobility and flexibility (less supported, voids may be present allowing material to flex). These point measurements can be plotted as a two-dimensional (2-D) contour plot to map the average mobility; this allows a better visualization of the surveyed area and can be used to interpret the lateral extent of subsurface voids.

4.1.2.2 Ultrasonic Pulse Echo

Ultrasonic pulse echo is a non-invasive and non-destructive testing method that uses acoustic shear (s-) waves to image shallow, subsurface layers based on changes in acoustic impedance. The UPE method was primarily designed to evaluate concrete from one surface of a slab (e.g., only the top side of a concrete slab is accessible). The Pundit PD 8000 UPE instrument houses an array of piezoelectric transducers that emit acoustic waves into the medium and record the transit time of waves that are reflected to the surface. These acoustic waves reflect off features that exhibit a change in acoustic impedance such as a void (e.g., delamination, honeycombing), change in material type, or change in material quality due to variations in concrete density or competency.

Raw UPE data quality is dependent on the initial calibration scan. A calibration scan is performed to determine the optimal data acquisition settings, including analog gain and pulse velocity, for the survey environment. These settings are evaluated using an a-scan recording and the characteristics of its wave envelope and instantaneous amplitude information. It is critical that the amplitude of the a-scan waveform is not clipped, which occurs when the transducers are overdriven with a voltage or current that exceeds its maximum capability and output.

Some limitations associated with UPE are the necessity for densely spaced test points to produce reliable and higher-resolution images, accurate instrument calibration prior to data acquisition to reduce signal amplitude clipping, and proper coupling between the UPE transducers and the test surface to reduce noise in the data. Although not feasible for this work, UPE is often used alongside ground penetrating radar (GPR) to provide more focused investigations of a given area. More specifically, GPR surveys are often used to “rapidly scan” a broad area to detect anomalous features within the subsurface. UPE surveys focus on those anomalous areas to provide high-resolution imaging, and some UPE systems offer near real-time scans of subsurface targets using artificial intelligence and simplified signal processing.

4.1.3 Data Collection

An initial set of geophysical surveys were performed on March 1-2, 2022, to determine which NDT methods would be suitable for data collection in the steel-lined concrete draft tube. Results of the initial survey in 2022 aided design repair conducted by Westin Joy and members of the Glendo Dam Powerplant facility. A follow up survey was performed on January 25, 2023, to identify changes in the NDT results that would suggest the grouting repair was successful. Geophysical surveys were conducted by Technical Service Center (TSC) geophysicist Sarah L. Morton Rupert and TSC (formerly WAO) mechanical engineer Michael D. Rauh.

For the first survey, a 2-D grid was designed and marked on the walls of Draft Tube No. 2 consisting of an approximately 6 feet (ft) tall (x) by 27ft wide (y) grid with 0.5ft spacing in both x - and y -directions; the grid does not include the section of the tube liner above or below the tube entrance. The grid origin $[0,0]$ was located at the top of the wall and to the right of the tube entrance (figure 1). Data points were collected in the vertical direction on the wall with column number (x -coordinate) increasing in the clockwise direction, (if viewed looking down) around the inside of the draft tube.

Point measurements were recorded every 0.5ft using the SIR and UPE instruments in both the x - and y -directions, where accessible. It is important to note that some grid locations had to be skipped due to the presence of the hanging platform support hooks mounted on the tube walls (figure 2); the approximate locations of these support hooks are noted in the results. The UPE system is larger than the SIR system, which prevented it from being used in slightly fewer locations when the hooks and chains were present compared to the SIR system.

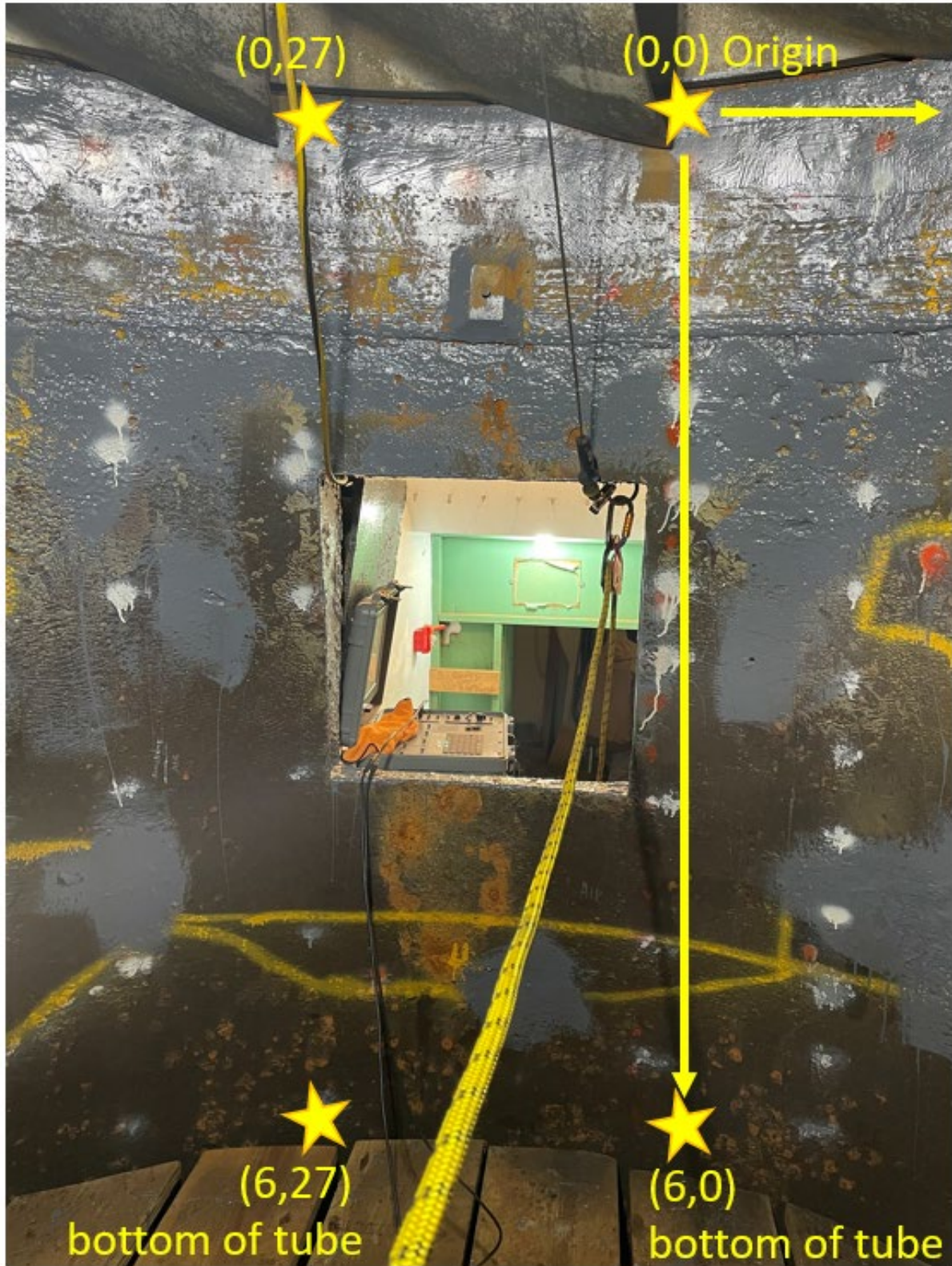


Figure 1.—Photo of 6 ft tall by 27 ft wide 2-D grid corner points (indicated with yellow stars) starting above the top right corner of the tube entrance and extending to the right for 27 ft in the horizontal direction.

Detection of Voids Behind Spillways, Conduits, Canals, Tunnels, and Siphons

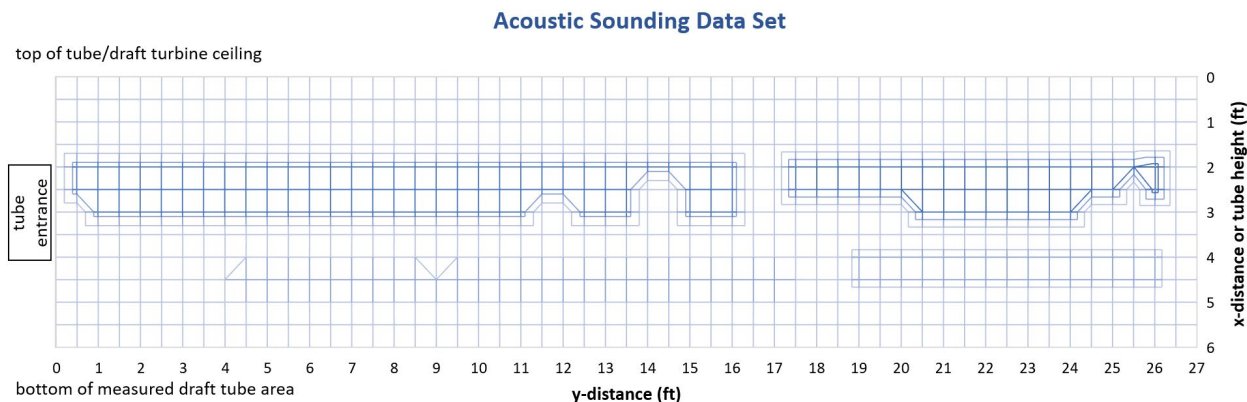


Figure 3.—2-D plot of acoustic sounding data set collected by Westin Joy and interpreted by Sarah Rupert for data visualization. Areas enclosed in polygons between $x = 2$ ft and $x = 3$ ft represent areas with suspected decoupling and voids behind the steel liner.

Slab impulse response results were plotted in the same coordinate system as the initial sounding data set. Areas possessing good sub-liner support are characterized by a lower-amplitude flexibility peak and a smoother or low-amplitude mobility curve. Areas possessing poor sub-liner support are characterized by a higher-amplitude flexibility peak and a higher-amplitude, low-frequency mobility peak.

In general, areas with the highest observed mobility were primarily located in the upper 0.5 - 1.5 ft from the top of the tube (figure 4). An example of this high mobility (poor sub-line support) is shown in figure 5 where a measurement recorded at [1.5, 9] exhibits a high-amplitude time domain signal of 10 in/sec compared to the measurement from [5.5, 19.5] with lower-amplitude time-domain signal less than 1.5 in/sec. A horizontal dashed line was superimposed on the 2-D plot (figure 4) to indicate where the grouting repair would be focused based on findings from other engineering inspections in the tube. This upper 1.5 ft of the tube liner is consistent with the SIR findings, which provides qualitative verification of where voids or steel liner-concrete decoupling exists.

The grouting repair was performed the week of January 23, 2023, and another SIR survey was requested following its completion (figure 6). The follow up SIR survey focused on the upper 3ft of the tube wall to coincide with the height of the grouting repair work. As a result, low-amplitude flexibility and smooth mobility curves were observed across most of the repaired area. This suggests the grouting successfully repaired the bonding between the steel liner and concrete foundation. An example of this repair is shown in figure 7 where a measurement indicating poor support from [1, 6] in 2022 now yields good sub-liner support after the grouting repair in 2023. At this location, the amplitude of the time domain signal decreased from a maximum of 5.5 in/sec to less than 1 in/sec, indicating that the support between the steel liner and concrete has improved.

Detection of Voids Behind Spillways, Conduits, Canals, Tunnels, and Siphons

Since these investigations, the draft tube has not shown signs of leaking, which suggests the inspections and geophysical results sufficiently identified damaged areas and that the grouting work successfully repaired the decoupling. Therefore, the SIR method has proven to effectively inform engineers about damaged areas in a steel-lined concrete draft tube and should be considered for future projects.

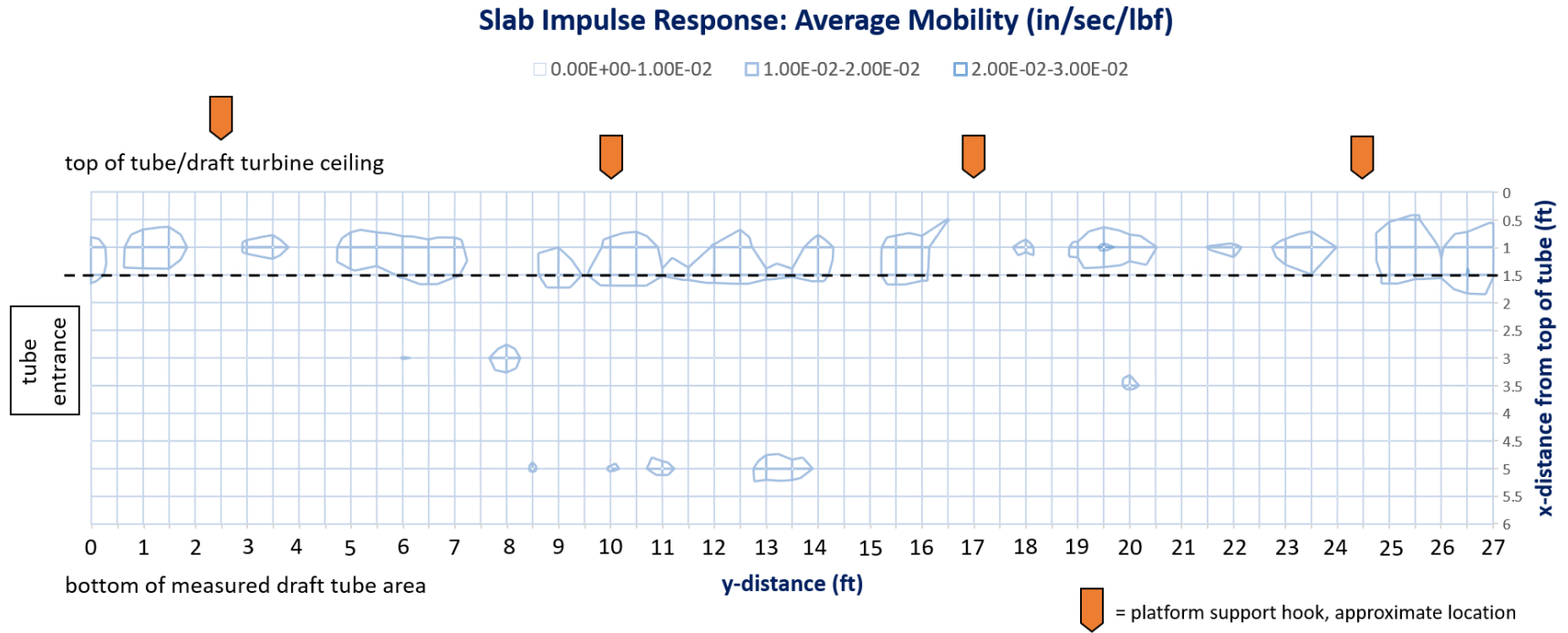


Figure 4.—2-D plot of slab impulse response average mobility measurements from the 2022 survey in Glendo Draft Tube No. 2. Blue polygons indicate areas that possess higher average mobility, suggesting the presence of delamination in these areas. The orange arrows indicate the location of platform support hooks. The horizontal dashed line indicates the upper section of the wall where grouting repairs were planned to be performed (i.e., $x=1.5$ ft).

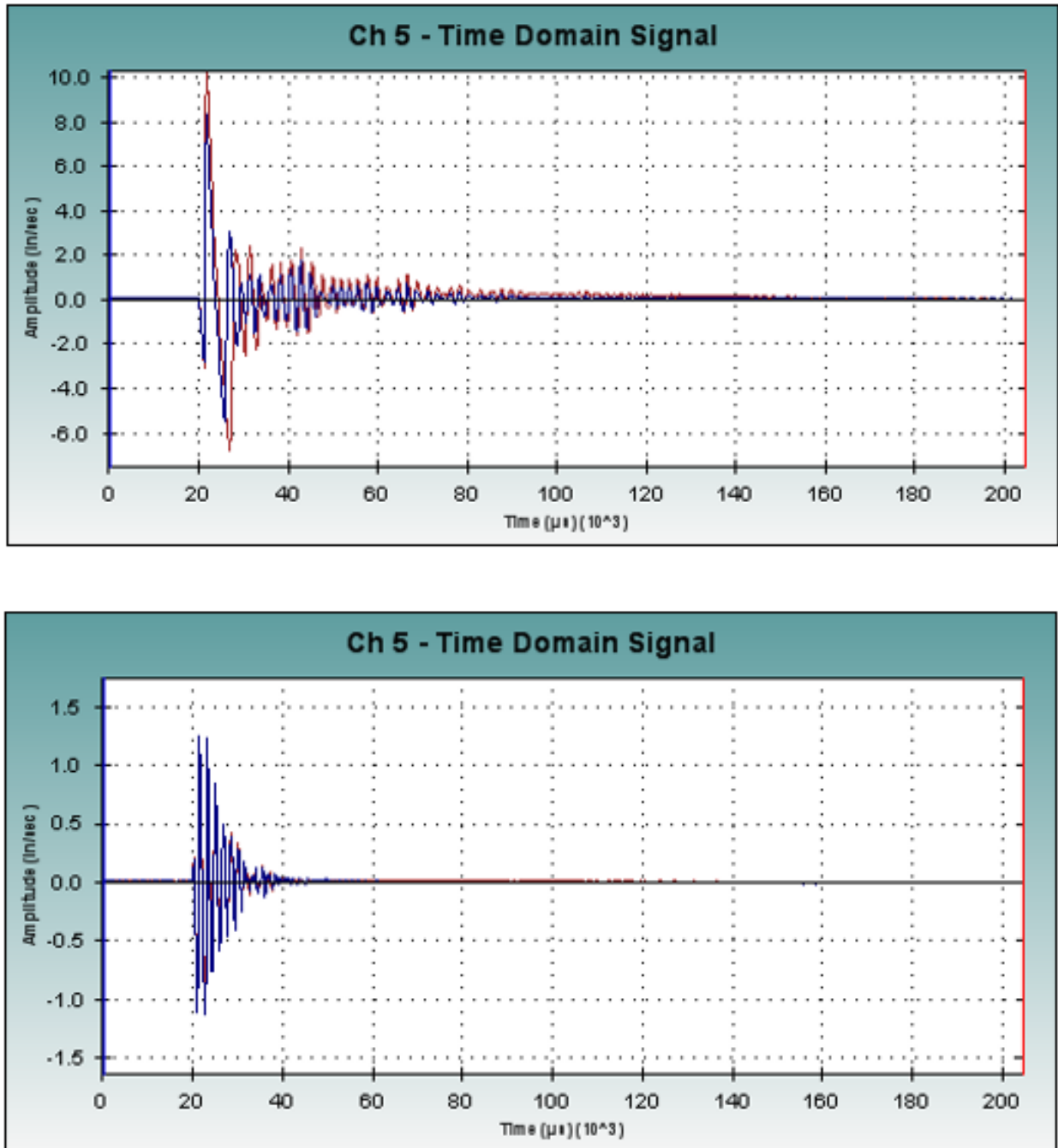


Figure 5.—Example of (top) a 2022 measurement with poor sub-liner support from [1.5, 9] and (bottom) a 2022 measurement with good sub-liner support from [5.5, 19.5]. The poorly supported area is characterized by the high-amplitude signal compared to the well supported area that exhibits a low-amplitude signal.

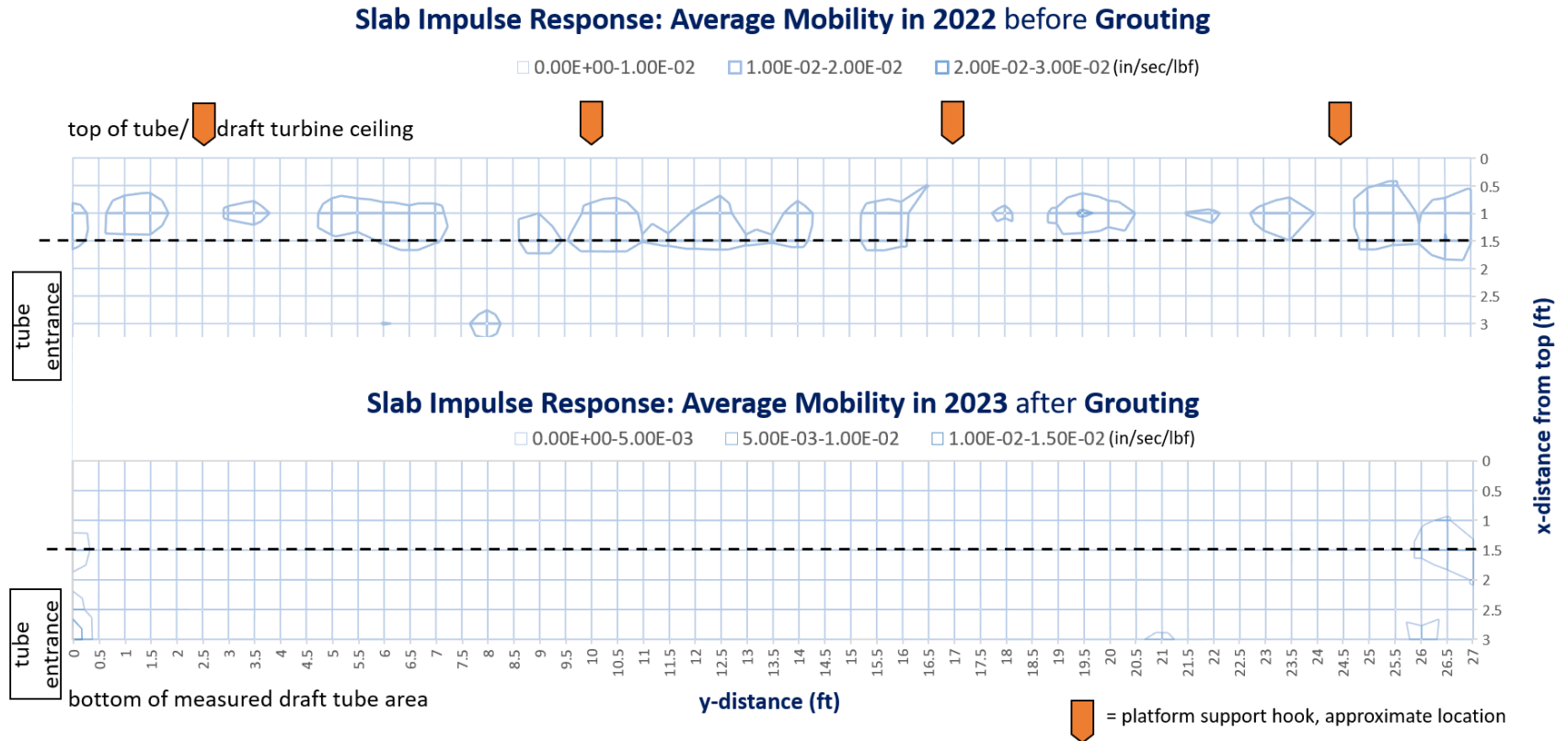


Figure 6.—2-D plots of slab impulse response average mobility measurements from the (top) 2022 survey and (bottom) 2023 survey in Glendo Draft Tube No. 2. Blue polygons indicate areas that possess higher average mobility, suggesting the presence of delamination in these areas. The orange arrows indicate the location of platform support hooks. The horizontal dashed line at [x = 1.5 ft] indicates the height on the wall where grouting repairs were planned and executed.

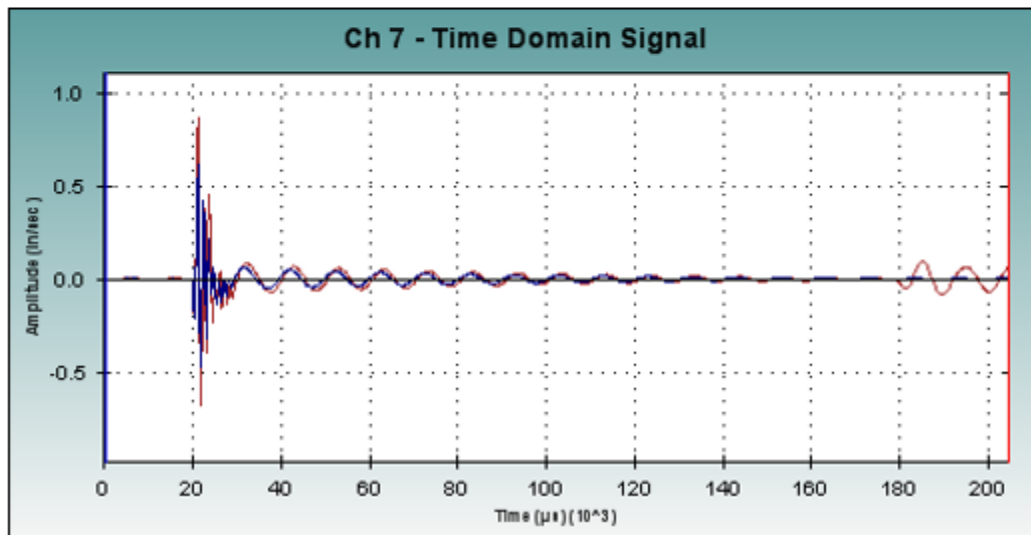
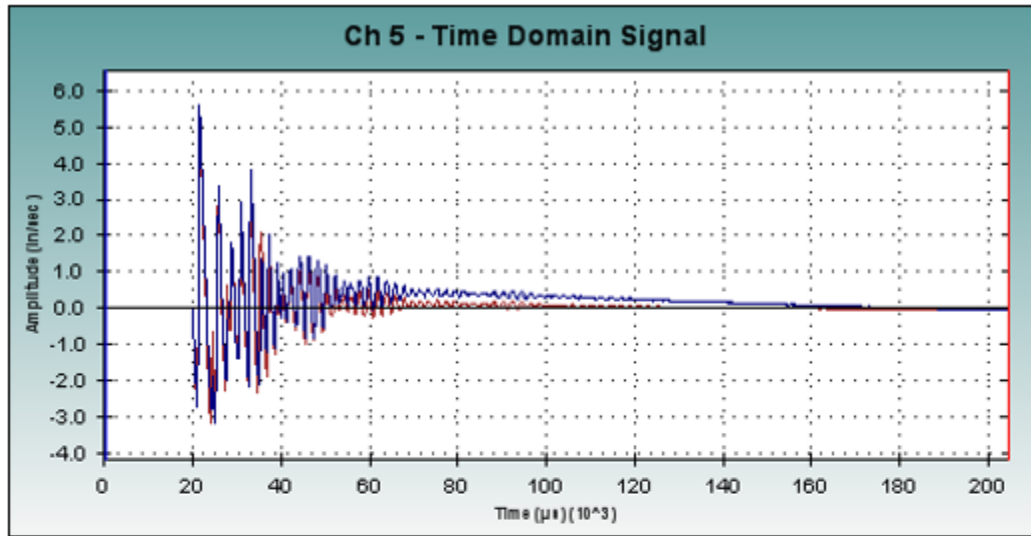


Figure 7.—Measurement from [1, 6] (top) before the grouting repair in 2022 and (bottom) after the grouting repair in 2023. Note how the amplitude of the time domain signal decreased from a maximum of 5.5 in/sec to less than 1 in/sec, indicating better support between the steel liner and concrete.

The UPE survey followed the same grid system as the SIR surveys. Results were plotted in 2-D with respect to the interpreted amplitude of wave reflections (figure 8). Amplitudes of wave reflections were classified into three categories: 0-0.5 indicating little to no observed reflection, 0.5-1.0 indicating moderate wave reflection, and 1.0-1.5 indicating maximum wave reflection (figure 9). A higher-amplitude reflection can be indicative of a subsurface void whereas a lower-amplitude reflection (or no reflection) likely suggests no void or defect in the subsurface; approximately 0-3ft below measurement point, the average maximum depth of investigation.

Detection of Voids Behind Spillways, Conduits, Canals, Tunnels, and Siphons

These higher amplitudes can be viewed in 1D traces with the signal and envelope have a higher amplitude compared to surrounding signals (figure 9a). These traces can then be viewed as 2-D color plots for an easier visual inspection of the surveyed area (figure 9b).

This method was designed for testing on concrete structures and its effectiveness on a steel lined structure was undetermined at the time of the investigation. Due to the curved surface of the draft tube, it was challenging to securely couple the instrument and all transducers with the tube surface. Inadequate coupling introduces unwanted noise, decreases data quality, and subsequently decreases the accuracy and overall confidence in the results. Therefore, relatively high-amplitude reflections interpreted in the UPE data set are more likely related to poor coupling rather than the presence of voids behind the tube liner.

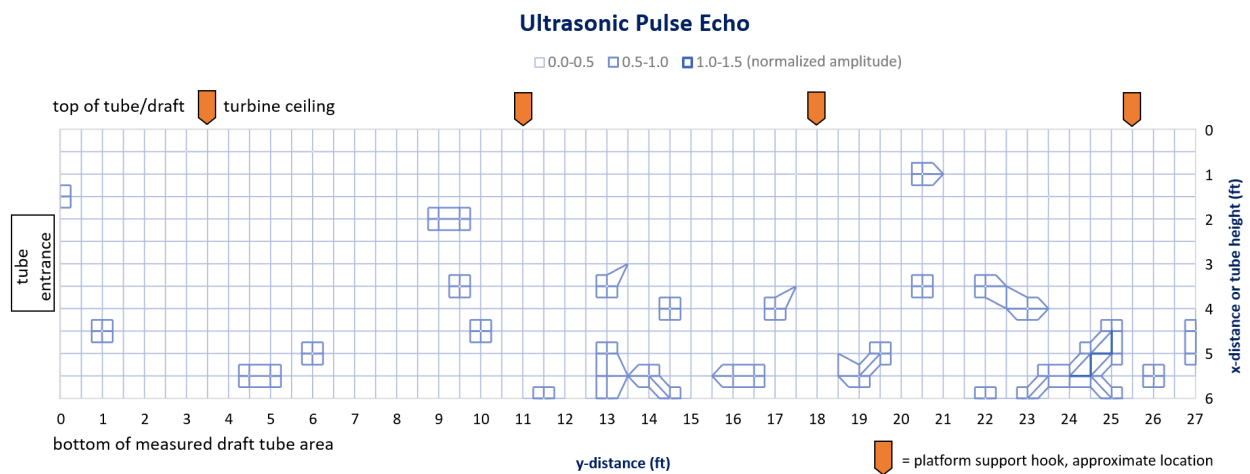


Figure 8.—2-D plot of interpreted UPE results. Areas enclosed in blue polygons represent areas where a higher-amplitude reflections were interpreted.

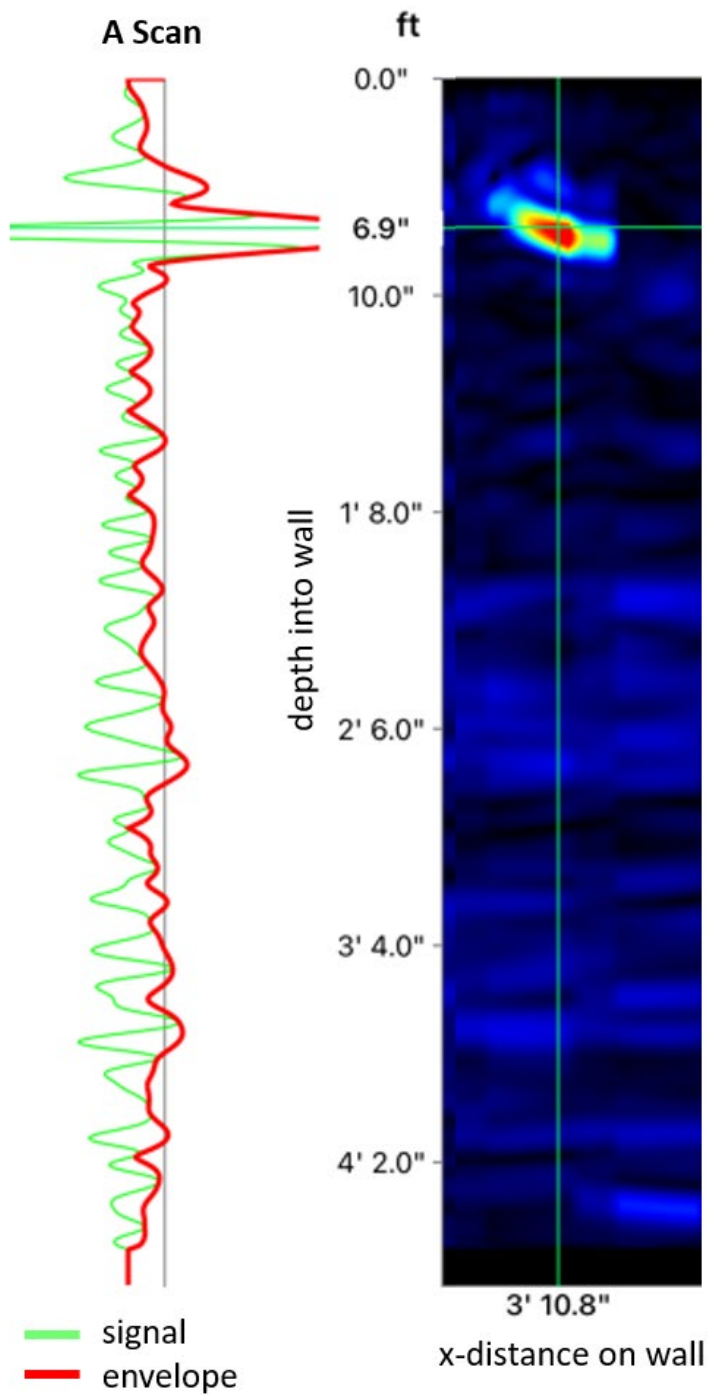


Figure 9.—Example UPE sounding from the 2022 survey. (Left) A-Scan signal where the 1-D trace signal amplitude is shown in green and the signal envelope is shown in red. (Right) Multiple 1-D traces can be viewed as a 2-D color plot where warmer colors represent higher-amplitude reflections and cooler colors represent low-amplitude to no reflection.

4.2 Experiment 2: Denver Federal Center

4.2.1 Background

An outdoor experiment was designed for this Science and Technology research project to evaluate how effectively different geophysical methods can detect voids beneath concrete slabs under varying conditions. More specifically, different types of metal reinforcement were investigated to determine how each affected the appearance of void signatures. The contents of the void were also investigated to determine whether these variations affected the appearance of void signatures as voids may occur under various environmental conditions including flooding, excessive drying, and snowy and icy weather.

Geophysical methods included:

- ground penetrating radar (GPR)
- impact echo (IE)
- thermography using a forward-looking infrared (FLIR) camera

GPR and IE are techniques commonly used by Reclamation geophysicists. The FLIR system is a newer technology to Reclamation personnel. GPR systems can be handheld or mounted on a cart for more rapid 2D imaging. IE and FLIR systems are handheld instruments that record point (1D) measurements. These two techniques are typically used for more focused investigations over small survey areas compared to the more rapid GPR surveying method. In many cases, GPR is used first to identify areas of interest within a large field area and then these smaller instruments (i.e., IE and FLIR) are used to provide complimentary data sets and verify the presence of observed anomalous features.

The outdoor experiment consisted of four concrete slabs produced in-house by TSC Civil Engineer, Caleb Nickel (8530). Each slab was made of 4000psi concrete with $\frac{3}{4}$ -inch maximum aggregate. Slab 1/N contained no reinforcement (N), Slab 2/M contained a single layer of mesh (M), Slab 3/SM contained a single rebar mat (SM), and Slab 4/DM contained a double rebar mat (DM). The single mat consisted of a seven-by-seven No.3 rebar layer at the base of the slab (figure 10a). The double mat was comprised of a seven-by-seven No.3 rebar layer at the base of the slab and a four-by-four No.3 rebar layer toward the top of the slab (Figure 10a). The mesh had 6-inch square spacing between wires (figure 10b).

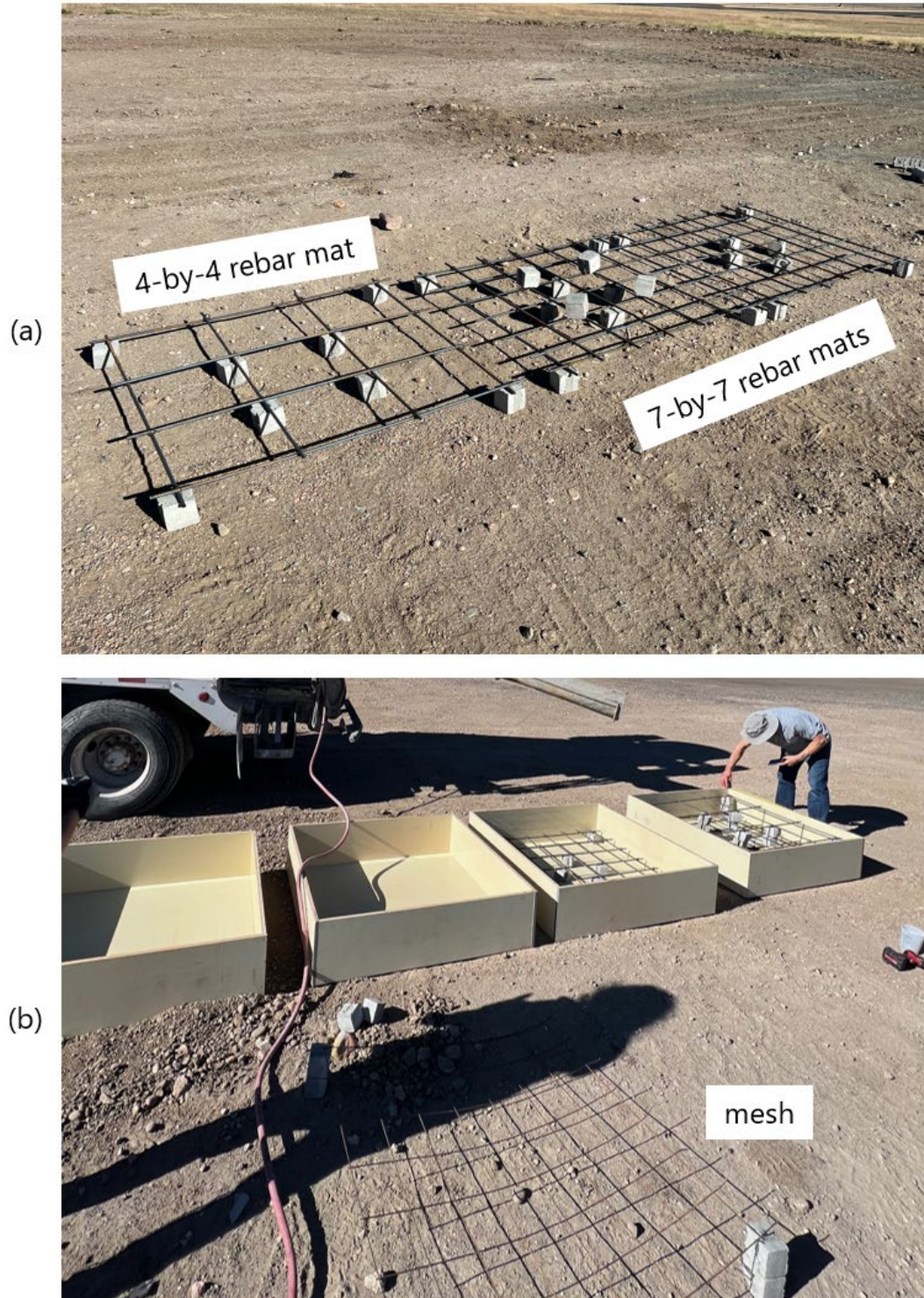


Figure 10.—(a) Photo of the four-by-four and seven-by-seven rebar mat reinforcements. (b) Photo of the wooden boxes used to form the concrete slabs with reinforcement materials. The rebar mats are placed in the boxes, the mesh is shown at the bottom of the image. Photos courtesy of Caleb Nickel (Civil Engineer/8530).

4.2.2 Methodology

4.2.2.1 *Ground Penetrating Radar*

GPR surveys are non-invasive and non-destructive, and they allow for the canvassing of an extensive area in a relatively short amount of survey time in the field (figure 11). GPR uses electromagnetic (EM) waves created by a transmitter antenna that are directed downward into the subsurface, reflecting off discrete objects and other boundaries where a change in the dielectric permittivity is present. These reflected EM waves then propagate back up to the ground surface where they are recorded by the receiver antenna of the GPR system. The time it takes for that EM wave to propagate down to a boundary and reflect upwards and back to the instrument is converted to a depth value after a two-way travel time and velocity calibration is calculated through data processing. The assessed propagation velocity can then be used to perform time-to-depth conversions. This velocity can also be used to perform reverse-time or Kirchhoff migration, which helps to focus the GPR image (e.g., collapses hyperbolas into points to reveal the true shape and location of reflectors at depth).

In the case of discrete objects (e.g., “reflectors”) such as a boulder, a hyperbolic reflection pattern is observed as the GPR system passes over these types of features. This hyperbolic data pattern is also generated when scanning across a metal pipeline in the perpendicular direction (i.e., scan line perpendicular to pipeline alignment). In the case of very closely spaced discrete objects or continuous interfaces (e.g., rebar matting or bedrock) a continuous GPR reflection (e.g., a reflection horizon) is observed in the recorded GPR 2-D profile. Both fixed and dynamic stacking were implemented during GPR surveys to maximize the signal-to-noise ratio (SNR) and the profile depth scale was approximated in the field using an appropriately assumed velocity model based on GPR surveys performed at this site. This velocity model and depth estimation can be recalibrated in post processing, if necessary, and does not adversely affect the quality of the data set.



Figure 11.—Photos of GPR data collection at the Denver Federal Center using a (left) cart-based system and (right) handle attachment. Each system has a built-in odometer wheel to track distance surveyed.

4.2.2.2 *Impact Echo*

The IE method measures the peak resonance frequency of a given material to estimate the thickness of that material layer. The instrument generates a high-frequency acoustic wave (i.e., seismic compressional wave [p-wave]) by impacting a surface with a small hammer (figure 12). This small hammer is built into the handheld instrument, or an external hammer may be equipped if a greater energy source is needed. This impact will excite the material and any signals that reflect upward (or “echo”) from a lower boundary are recorded by the IE instrument. Such lower boundaries may be related to a lower slab boundary or an internal flaw in the primary material such as a crack or honeycombing feature. Given an assumed p-wave velocity of the surveyed material and the recorded two-way travel times of these repeating signals, the depth to that lower boundary (or thickness of that layer) is calculated for the layer possessing the observed peak frequency.

The shape of the observed peak frequency can be used to evaluate the condition of a material boundary. For example, a sharp, high-amplitude peak (figure 13, top) is often indicative of competent material that is well-supported by a deeper material. If the peak broadens or deteriorates (figure 13, bottom), it is likely the result of deformation within the survey material. These features can be associated with honeycombing or poorly cemented aggregate within a concrete subsurface.



Figure 12.—Photo of Impact Echo data collection on the experimental slabs. The grey box (left) is the laptop and datalogger which attaches to the IE instrument (right).

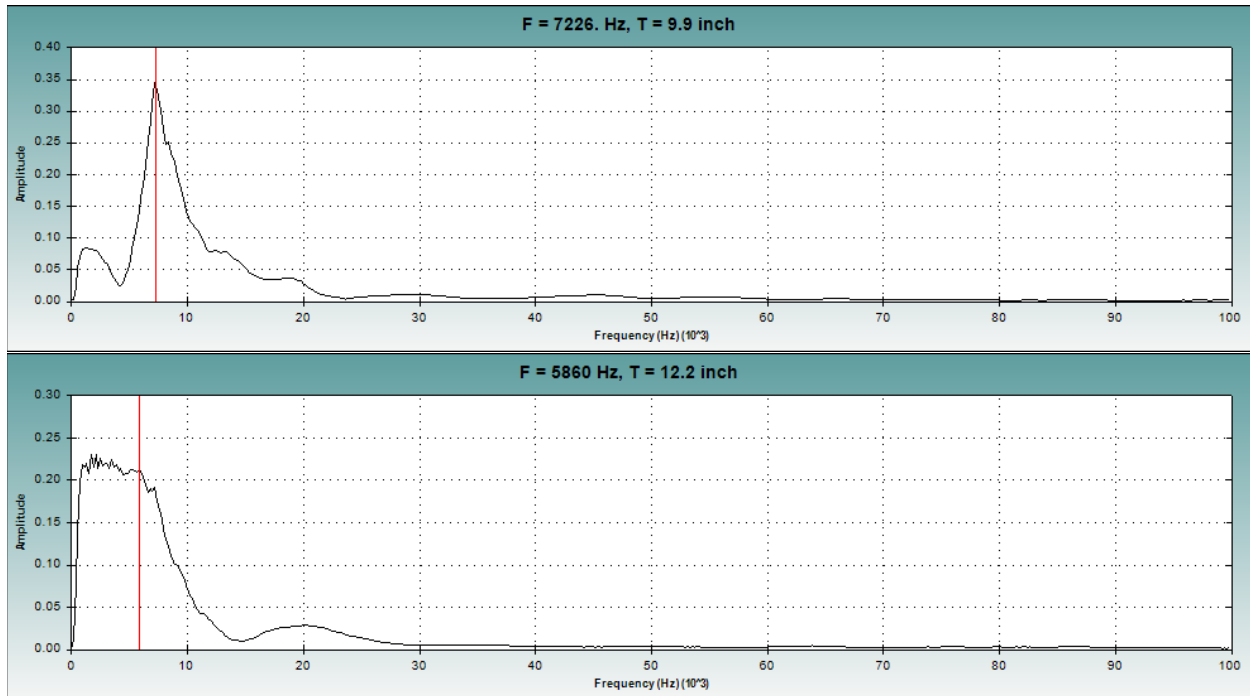


Figure 13.—Impact Echo (IE) amplitude versus frequency plots with automatically estimated peak frequencies (vertical red lines) and corresponding depth to a deeper reflection boundary. Top image displays a sharp spike in amplitude, representing the materials’ resonance frequency with a corresponding depth estimation. Bottom image displays a poorly defined range of high-amplitude signals, likely due to deformations in the measured concrete layer.

4.2.2.3 FLIR

A FLIR, or forward-looking infrared camera, E96 Advanced Thermal Imager (figure 14) is a non-contact device that uses thermal imaging to detect and generate images based on the presence of heat rather than visible light. These thermal signals (i.e., radiation) are emitted by all objects that are warmer more than absolute zero and are considered invisible to the human eye. A FLIR camera is mostly used to identify changes in heat, the warmer the object, the more thermal energy it will emit. For this investigation, heat variations of interest can be related to the presence of moisture, ice, and exposed material surfaces (e.g., voids).



Figure 14.—(Left) Photo of geophysicist Miriam Johnston using the FLIR during one of the outdoor experiments. (Right) Image of the FLIR E96 handheld system, courtesy of manufacturer website (T. Equipment).

4.2.3 Experimental Design and Data Collection

Four experiments (table 3) were designed to evaluate the effectiveness of geophysical imaging techniques. The first experiment (E1) did not have a void present under each slab to establish a baseline for each of the four imaging techniques. Geophysical surveys were repeated for each subsequent experiment to detect a longitudinal air-filled void (experiment 2, E2), a longitudinal water-filled void (experiment 3, E3), and a longitudinal void filled with partially frozen water (experiment 4, E4).

Table 3.—Summary of concrete slab experiments

Experiment	Subslab Condition
E1	No void
E2	Air-filled longitudinal void
E3	Water-filled longitudinal void
E4	Partially frozen water-filled longitudinal void

The four concrete slabs were placed on the ground (table 4) and in a continuous row at a test site on the Denver Federal Center campus (figure 15). Each slab was separated by a 2ft by 4ft by 1ft tall Styrofoam block to minimize reflections from different reinforcement types during GPR surveys (figure 15) resulting in a 22ft long by 4ft wide survey grid across the continuous top surface of the slabs and Styrofoam. A ramp was constructed at the start and end of the row for easier access with the GPR cart system (figure 16). Survey lines were marked on all slabs at 0.5ft spacing in both the short-axis (x-) direction and long-axis (y-) direction to aid data collection (figure 17).

Table 4.—Concrete slab characteristics

Slab	Reinforcement	Y-Distance (ft) in grid
1	None (N)	0–4
2	Mesh (M)	6–10
3	Single rebar mat (SM)	12–16
4	Double rebar mat (DM)	18–22

All field surveys were performed in November 2022 with outdoor temperatures varying between 30-60 degrees Fahrenheit with a snow event occurring between Experiment 3 and Experiment 4. The experiment consisted of four parts, with each focused on a different subslab void condition. An approximately 0.5ft-wide by 0.5ft-deep void was hand dug with a shovel after Experiment 1 surveys to simulate a continuous longitudinal feature beneath the center y-axis of the concrete slabs (figure 18). For the third experiment, the void was lined with a visqueen plastic film to prevent the added water from draining (figure 18, figure 19). The water was left overnight during a snowstorm and the surveys were repeated the following morning (E4) to image under partially frozen conditions.

Detection of Voids Behind Spillways, Conduits, Canals, Tunnels, and Siphons



Figure 15.—Photo of field experiments showing each of the four concrete slabs. Slab 1 had no reinforcement (N), Slab 2 had a mesh reinforcement (M), Slab 3 had a single rebar mat (SM), and Slab 4 had a double rebar mat (DM).



Figure 16.—Photo of ramp construction on each end of survey area to aid GPR surveying.



Figure 17.—Photo of concrete blocks with survey grid marked along the edges to indicate total distance along the survey grid. This photo shows block 4 marked from $x=18$ to 22ft.



Figure 18.—Photo of longitudinal tunnel hand dug under the long axis of the experimental setup. A layer of visqueen plastic film was used to prevent the added water from draining during surveys.



Figure 19.—Photo of water-filled visqueen films that were placed under each of the four concrete slabs.

4.2.4 Results

Summary of table 5 provides an overview of the results from experiments 2, 3, and 4. Results from experiment 1 are considered baseline and are compared to subsequent experiments throughout this section. Each methodology was noted with Y (yes) if a void was detected, N (no) if no void was detected, or N/A (not applicable) if no results were returned for each experiment. A more detailed analysis of these results and supporting figures are provided in the next subsections.

Table 5.—Geophysical results summary table

Method	Slab	E2: Air-filled Void				E3: Water-filled Void				E4: Partially Frozen Water-filled Void			
		1/N	2/M	3/SM	4/DM	1/N	2/M	3/SM	4/DM	1/N	2/M	3/SM	4/DM
GPR		Y	Y	Y	Y	N	N	Y	Y	Y	Y	N	Y
IE		N	N	N	N	N	N	N	N	N	N	N	N
UPE		N/A	N/A	N/A	N/A	N/A	N/A	N/A	N/A	N/A	N/A	N/A	N/A
FLIR		N	N	N	N	N	N	N	N	Y	Y	Y	Y

Note: N/1 refers to slab 1 with no reinforcement, M refers to slab 2 with wire mesh reinforcement, SM refers to slab 3 with single rebar mat reinforcement, and DM refers to slab 4 with double rebar mat reinforcement.

4.2.4.1 GPR

A small 2-D GPR grid was collected using 0.5ft by 0.5ft line spacing across concrete slabs resulting in 2-D profiles in both x- (long axis) and y-directions (short axis); these 2-D profiles were combined to generate 3-D depth slices. GPR profiles and corresponding depth slices for all experiments are shown in figure 20 through figure 28. The x-direction was parallel to the longitudinal void, and the y-direction was perpendicular to the orientation of the void. It is important to note that filtering parameters varied from line to line depending on the level of noise observed in each profile. Therefore, interpretations are based on qualitative signal changes (e.g., the appearance of abnormal signal, relative change in amplitude), rather than quantitative signal variations (e.g., exact decibel change in signal). It is also important to note that any void directly under a metal object, such as rebar, is considered undetectable. Features below metal objects are essentially masked because nearly all EM wave energy are reflected to the surface, leaving little to no signal to reflect off deeper targets.

In general, each type of metal reinforcement was interpreted in GPR profiles from the x-axis (long axis) of each experimental setup (figure 20) as well as the different 3-D depth slices (figure 24, figure 26, figure 28). High-amplitude, coherent hyperbolas associated with the double rebar mat were observed in each of the four experiments compared to the hyperbolas related to the other reinforcement types (mesh, single rebar mat). GPR profiles from the y-axis (short axis) were more affected by the short, vertical edges of each slab, which required signals to be muted to minimize other potential features of interest being masked by the more dominant

edge effects. GPR anomalies related to the void were more readily observed in Experiment 2 (figure 23), with hyperbolas appearing at the edges of the void trench and ringing signals originating from within the air-filled void.

Overall, the most commonly anomaly signatures in GPR profiles were hyperbolas (figure 23, figure 25, figure 27) and ringing signals (figure 23, figure 25); these signatures are likely associated with the longitudinal void beneath the concrete slabs. A high-amplitude, longitudinal feature was also observed beneath Slab 3/M in Experiment 2 (figure 24) and beneath Slab 4/DM in Experiment 4 (figure 28).

4.2.4.2 Impact Echo

As a point measurement method, the resulting values did not yield a specific indication of a void along a specific alignment or beneath any of the tested slabs (figure 29). From a broader perspective, slabs 1/N, 2/M, and 3/SM yielded relatively consistent slab thickness estimations (i.e., 1-1.14ft) during Experiment 1, when no subslab void was present. However, IE measurements taken across slab 4/DM with the double rebar mat yielded a significant overestimation of slab thickness (i.e., 1.25-1.5ft).

Once the void was introduced in Experiment 2, slab thickness estimations became irregular across each slab regardless of reinforcement type and subslab void conditions. Measurements taken over the air-filled void (E2) yielded the greatest change in slab thickness estimations compared to those from other experiments (table 6). In Experiment 2, slab thickness estimations increased by 7-11.4% across slabs 1, 2, and 3, whereas the estimated thickness across Slab 4/DM remained relatively unchanged. In Experiment 3, slab thickness estimations increased by 2 - 8.2% across slabs 1, 2, and 3, whereas the estimated thickness across slab 4 decreased by approximately 3%. Lastly, in Experiment 4, slab thickness estimation across slab 1/N remained nearly unchanged compared to Experiment 1. Slabs 2/M and 3/SM exhibited a 5-7.5% increase compared to Experiment 1 and Slab 4/DM exhibited a 2% decrease compared to Experiment 1.

Table 6.—Average of slab thickness (ft) across each slab

	1/N	2/M	3/SM	4/DM
Exp. 1	1.138	1.142	1.141	1.257
Exp. 2	1.218	1.231	1.271	1.254
Exp. 3	1.161	1.219	1.235	1.220
Exp. 4	1.149	1.229	1.198	1.234

Based on these experiments, slab thicknesses were slightly overestimated across the slab with a double mat (i.e., slab 4/DM) whether the void was or was not present. Once a void was introduced, measurements taken across slabs 2/N and 3/SM also yielded overestimated values. This suggests that the increased and more rigid reinforcement in the slab creates unwanted noise that causes additional resonance and subsequently leads to an overestimation of slab thickness.

Although thickness estimations across slab 4/DM were slightly greater than the true thickness, they remained relatively unchanged compared to all other slabs. This suggests that the double rebar mat adequately reinforced the slab and reduced the effects of subslab voids (unsupported areas) on the concrete slab. Slab 4/DM displayed great performance, but ultimately the likelihood of detecting a void beneath such a slab remains challenging.

4.2.4.3 UPE

Due to time and software constraints, no results are currently available from the UPE surveys. Data files are available upon request.

4.2.4.4 FLIR

In general, the thermal energy emissions recorded using FLIR were consistent with the outdoor air temperature at the time of each data collection. Images displaying the distribution of thermal energy emissions (in degrees Fahrenheit) across each slab are shown in figure 30. It is important to note that color scales are consistent across each slab by experiment, but color scales varied from experiment to experiment. All images are displayed with the same x-y orientation with a white dashed rectangle overlain across the images representing the void location.

During Experiment 1, temperature distribution (55-56°F) was relatively uniform across all slabs regardless of reinforcement type (figure 30a). Experiment 1 was performed in early afternoon, which likely contributed to the higher recorded temperatures. After the void was dug (Experiment 2), some variations in thermal energy emission distribution were observed, though no specific feature could be correlated to subslab void (figure 30b). Some relatively higher temperatures (e.g., red coloring referring to 40°F) were observed on one side of each slab, though this may be related to projection of the sun during data collection. Experiment 2 images were taken in late afternoon of the same day as Experiment 1; the sun was at a lower angle leading to a consistent temperature anomaly on the same side of all slabs. A similar display of higher temperatures was observed during Experiment 3 (figure 30c), which was performed the following day in early to mid-afternoon. Therefore, the relatively higher temperatures are attributed to direct sunlight on that side of the slab.

Experiment 4 was performed the next morning while air temperatures were below freezing and after a snowstorm. In contrast to the other experiments, a relatively lateral feature possessing higher thermal energy emissions was observed in FLIR images during the last experiment (figure 30d). The location of this lateral feature coincides with the alignment of the partially filled void, along the longitudinal y-axis, suggesting that this region of concrete above the void maintained a slightly elevated temperature. These middle sections of each slab yielded temperatures from 32°F to 42°F, ranging 10-20°F warmer than each slab's outer areas. Interestingly, the thermal anomaly across slab 2/M had the highest increase in temperature whereas the thermal anomaly across slab 4/DM had the lowest increase in temperature. This suggests that the mesh reinforcement may have allowed the slab to better maintain a higher temperature in the partially filled void compared to the double rebar mat reinforcement. This may also suggest that the FLIR method is better suited for void detection during colder temperatures whose voids are possibly

Detection of Voids Behind Spillways, Conduits, Canals, Tunnels, and Siphons

related to freeze-thaw. It is also important to note that FLIR images from Experiments 1 and 2 were not taken at the same time of day as Experiments 3 and 4. The warmer daytime temperatures may have limited the total magnitude of change observed during Experiments 1 and 2.

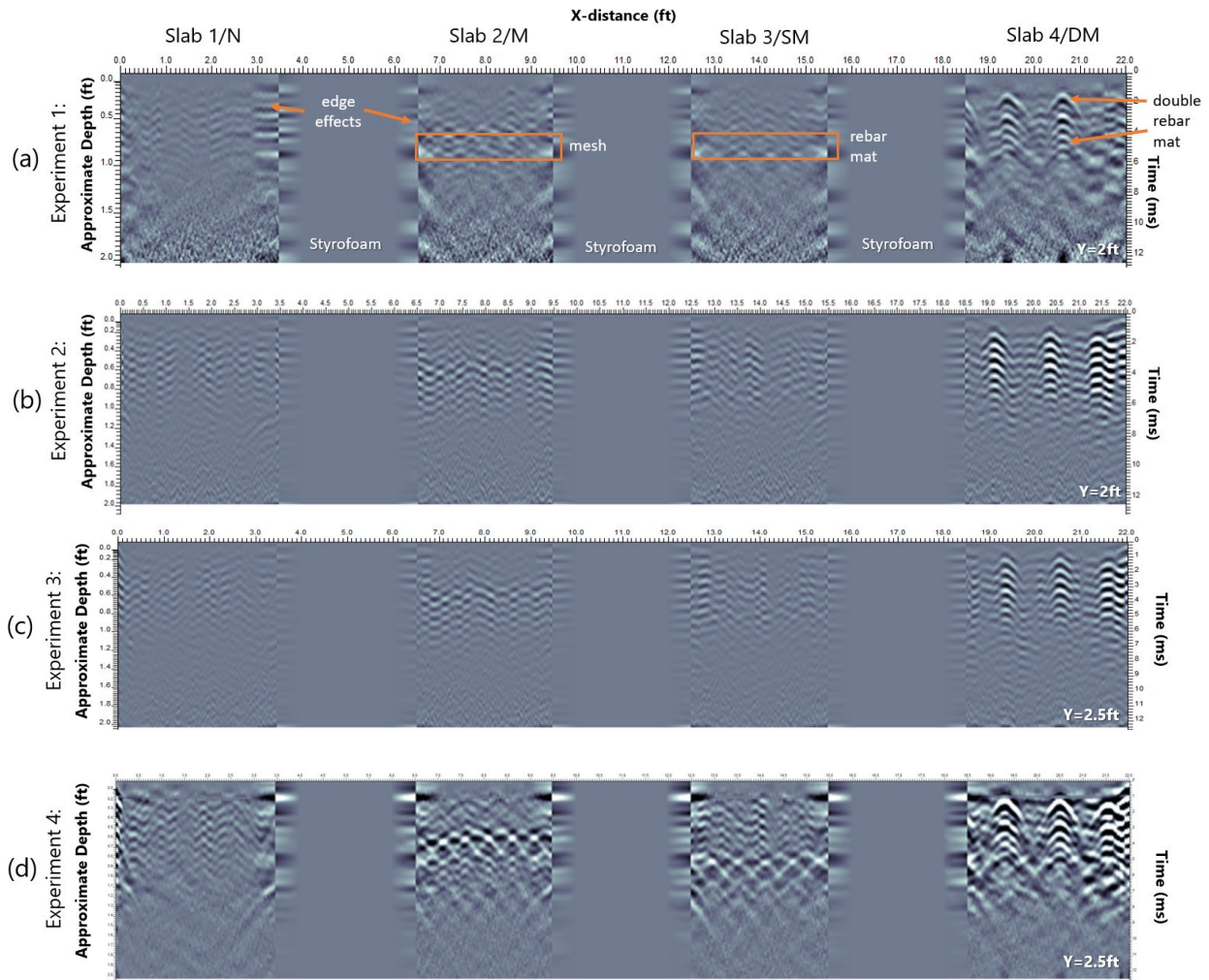


Figure 20.—X-axis (long-axis) GPR profiles across the centerline of each experimental setup. Each profile includes all four concrete test slabs with varying types of reinforcement separated by a Styrofoam block. For reference, the locations of each reinforcement are indicated in Experiment 1.

Detection of Voids Behind Spillways, Conduits, Canals, Tunnels, and Siphons

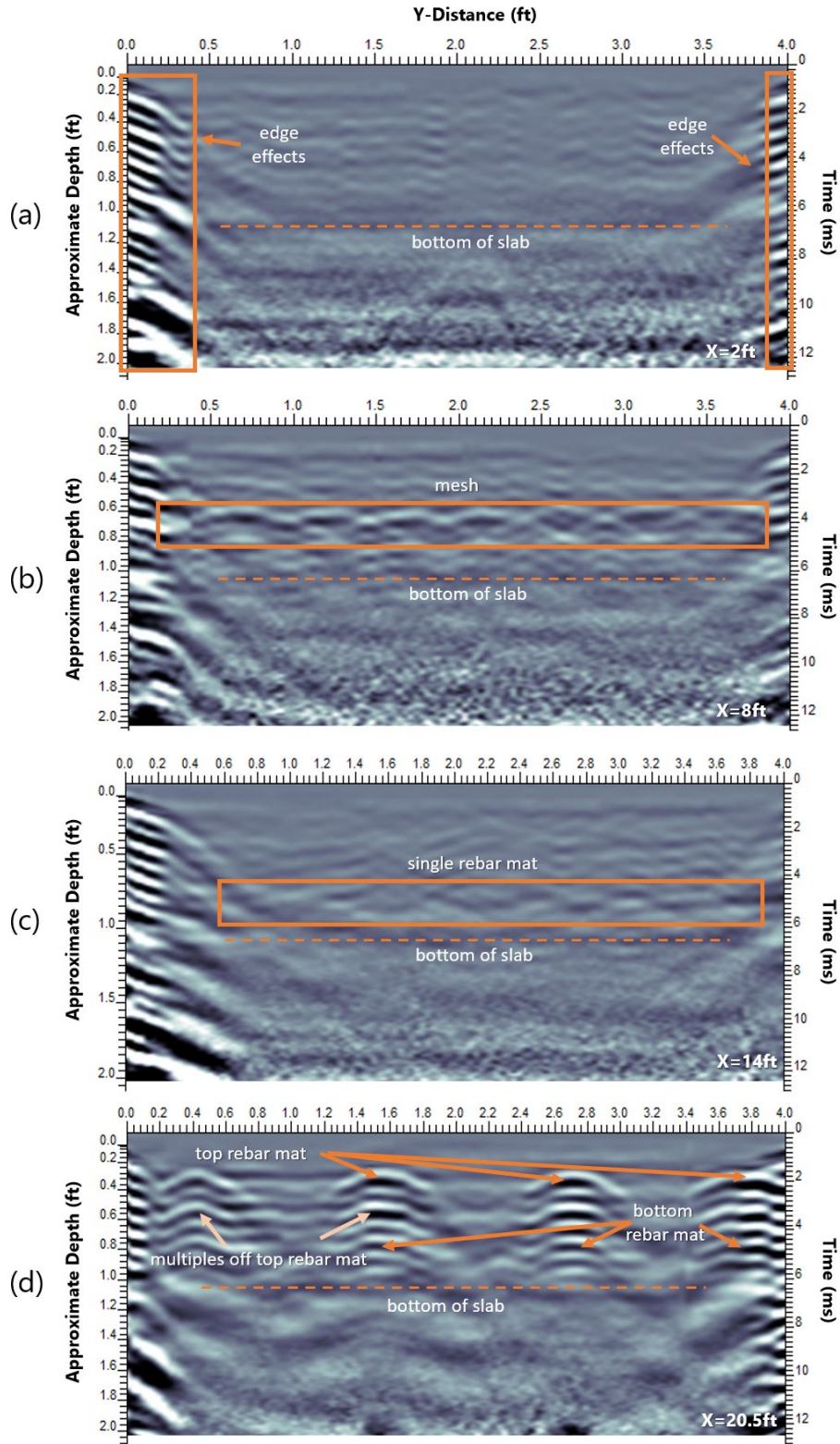


Figure 21.—Y-axis (short axis) GPR profiles across each concrete slab in Experiment 1; no void is present in this setup. The locations of each reinforcement and interpreted bottom of each slab are indicated in each profile.

Detection of Voids Behind Spillways, Conduits, Canals, Tunnels, and Siphons

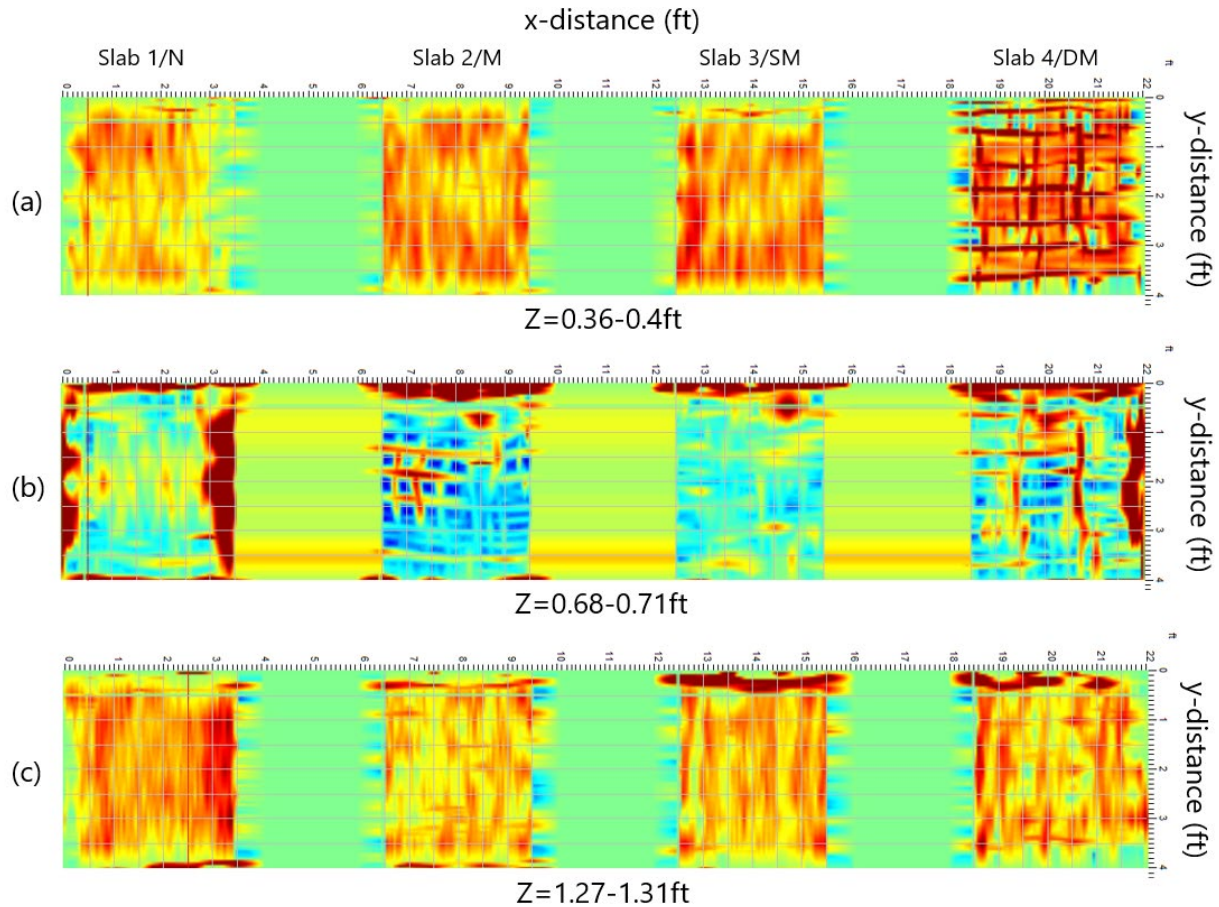


Figure 22.—Depth slices (plan-view profiles) from Experiment 1. Each depth slice includes all four concrete test slabs with varying types of reinforcement separated by a Styrofoam block. (a) The upper rebar mat is observed in slab 4 at 0.38 ft depth. (b) the wire mesh and rebar mats are observed at approximately 0.7 ft depth. (c) the bottom of the slab is at approximately 1.2 ft depth.

Detection of Voids Behind Spillways, Conduits, Canals, Tunnels, and Siphons

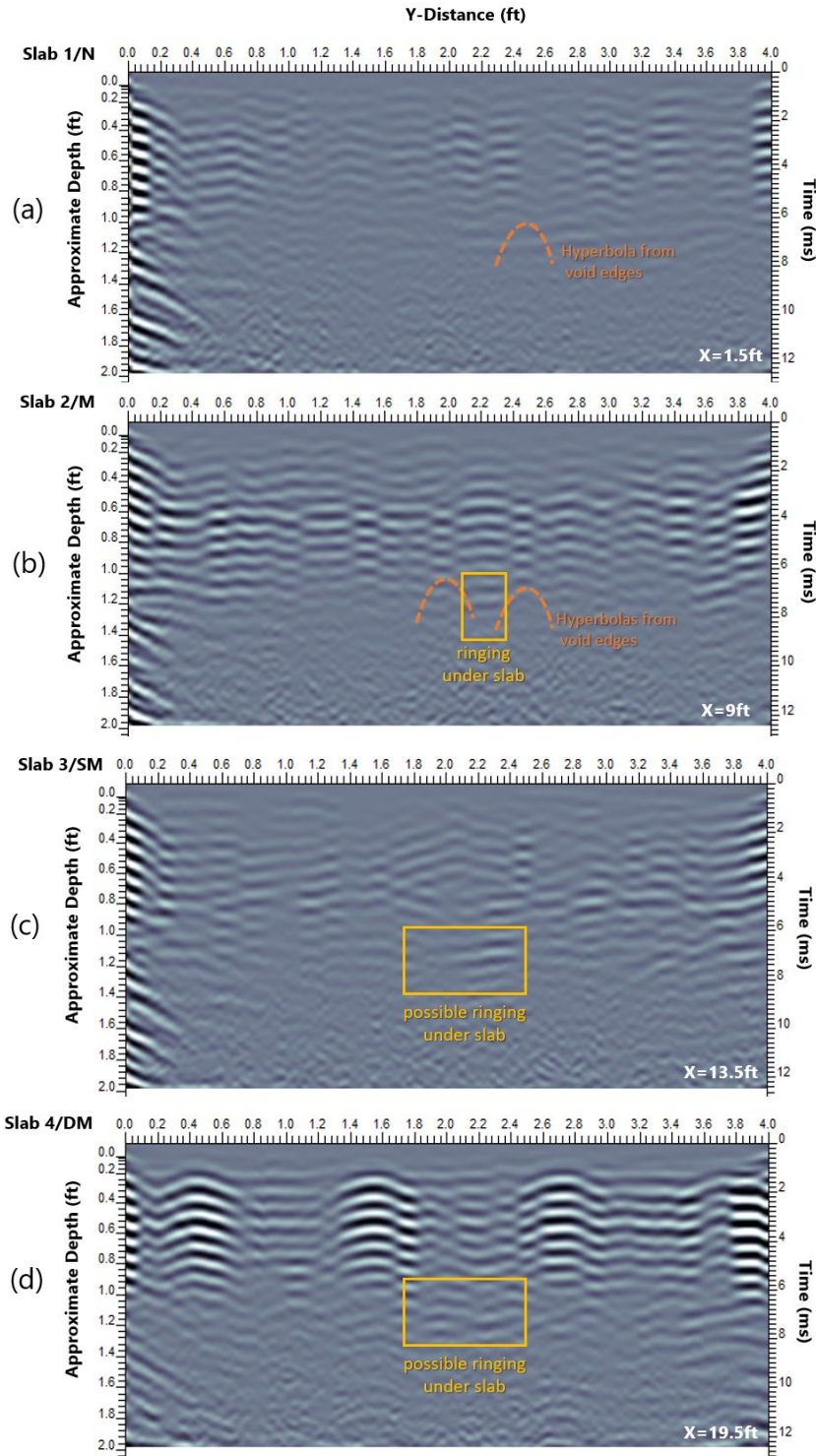


Figure 23.—Y-axis (short axis) GPR profiles across each concrete slab in Experiment 2 with an air-filled void; the void centerline is at approximately $y = 2$ ft. Evidence of the void are interpreted in each profile as either hyperbolas from the lateral edges of the void or ringing beneath the concrete slab.

Detection of Voids Behind Spillways, Conduits, Canals, Tunnels, and Siphons

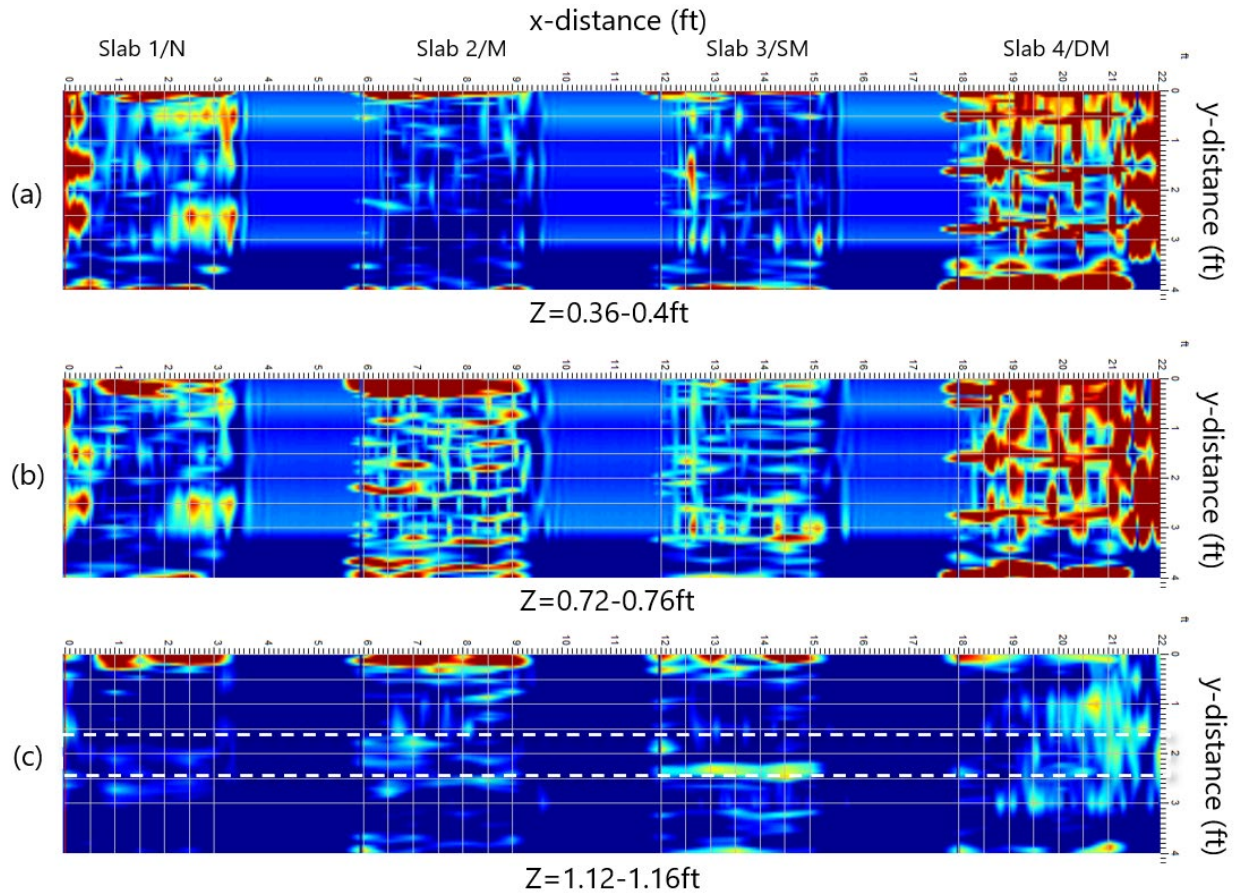


Figure 24.—Depth slices (plan-view profiles) from Experiment 2. Each depth slice includes all four concrete test slabs with varying types of reinforcement separated by a Styrofoam block. (a) The upper rebar mat is observed in Slab 4/DM at 0.36 ft depth. (b) the wire mesh and rebar mats are observed at approximately 0.72 ft depth. (c) the bottom of the slab is at approximately 1.2 ft depth. A longitudinal feature is observed below Slab 3/SM in the approximate location as the air-filled void.

Detection of Voids Behind Spillways, Conduits, Canals, Tunnels, and Siphons

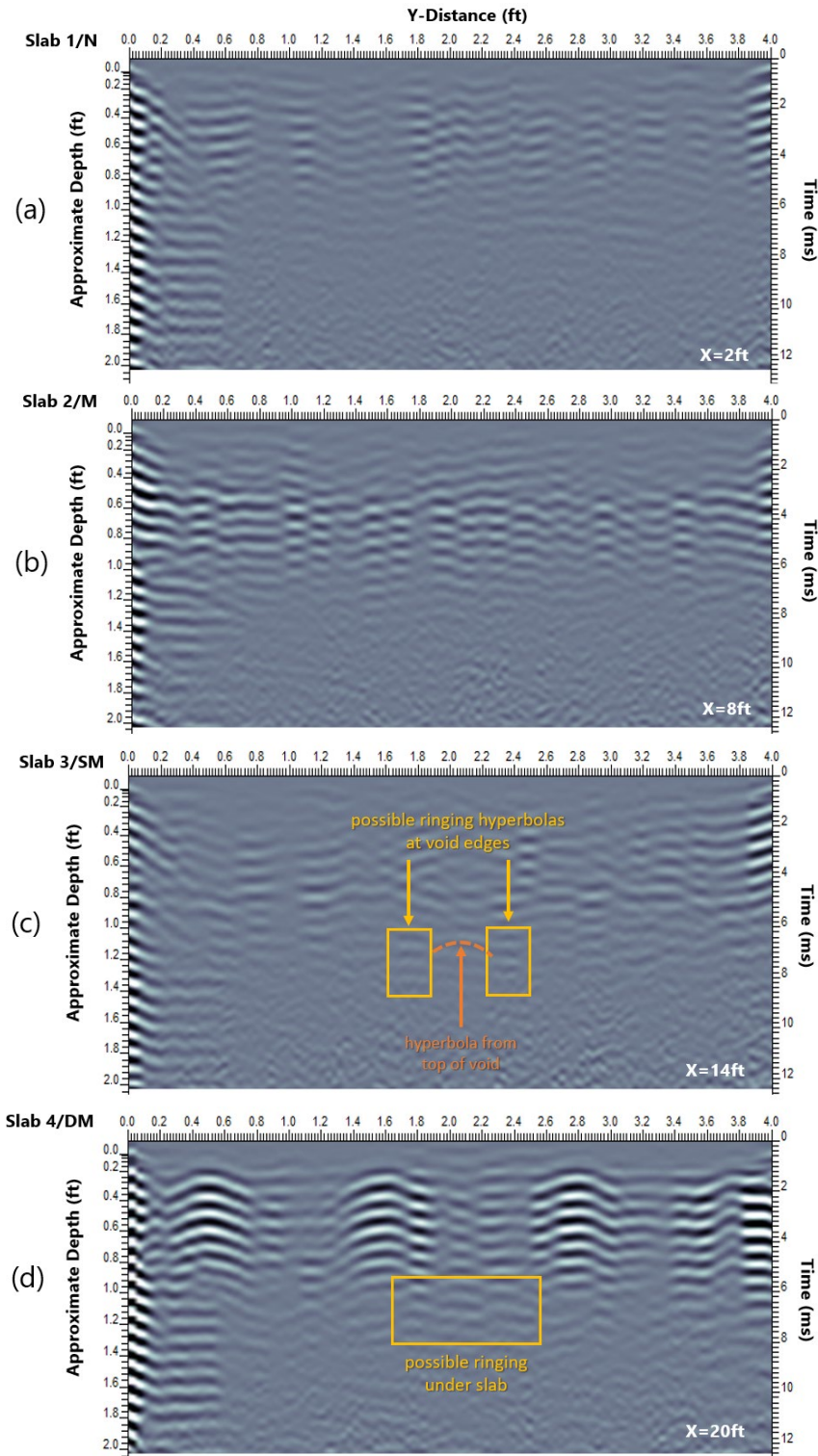


Figure 25.—Y-axis (short axis) GPR profiles across each concrete slab in Experiment 3 with a water-filled void; the void centerline is at approximately $y = 2$ ft. Evidence of the void are interpreted below Slab 3/SM and Slab 4/DM as either hyperbolas or ringing beneath the concrete slab.

Detection of Voids Behind Spillways, Conduits, Canals, Tunnels, and Siphons

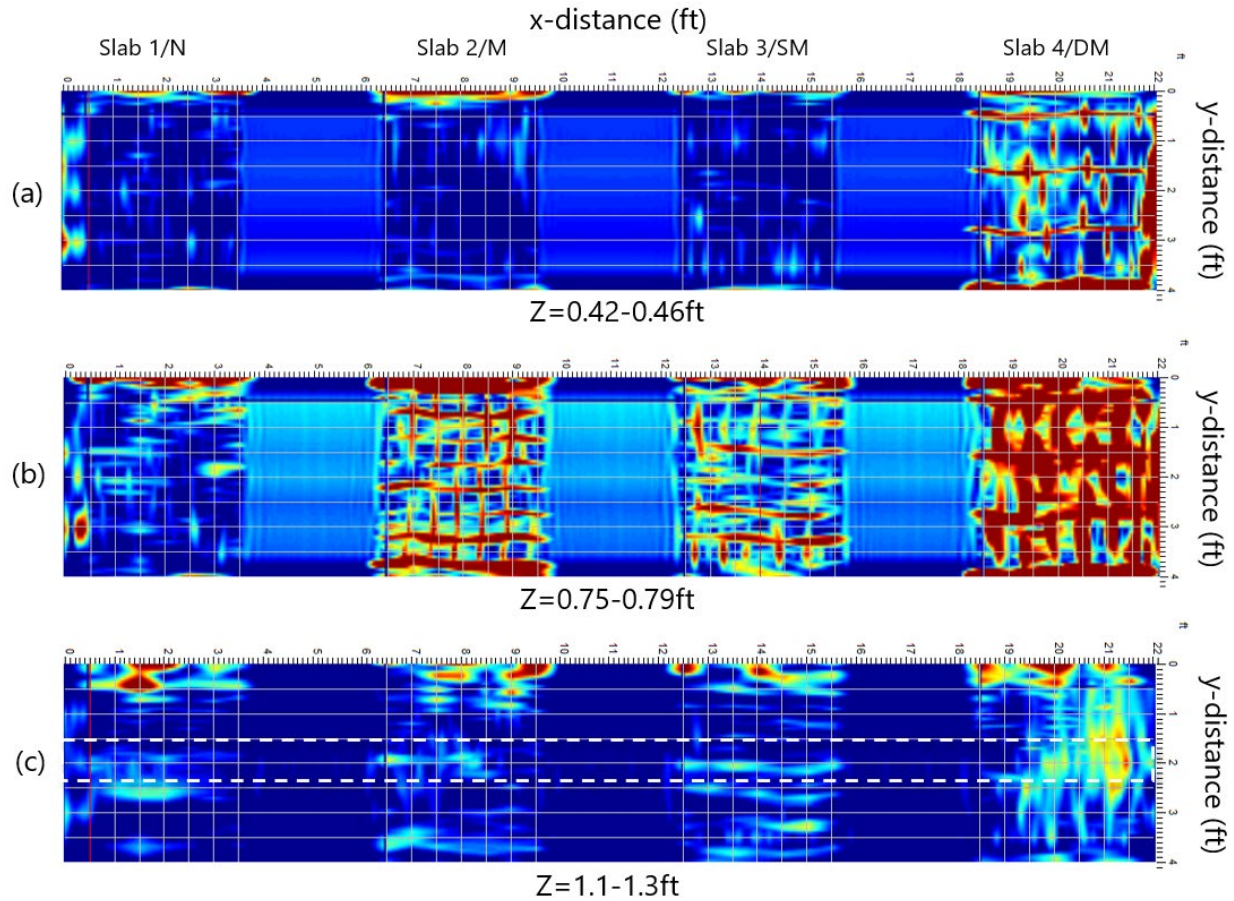


Figure 26.—Depth slices (plan-view profiles) from Experiment 3. Each depth slice includes all four concrete test slabs with varying types of reinforcement separated by a Styrofoam block. (a) The upper rebar mat is observed in Slab 4/DM at 0.42ft depth. (b) the wire mesh and rebar mats are observed at approximately 0.75ft depth. (c) the bottom of the slab is at approximately 1.2ft depth. A low-amplitude longitudinal feature is observed below Slab 2/M and Slab 3/SM in the approximate location as the water-filled void.

Detection of Voids Behind Spillways, Conduits, Canals, Tunnels, and Siphons

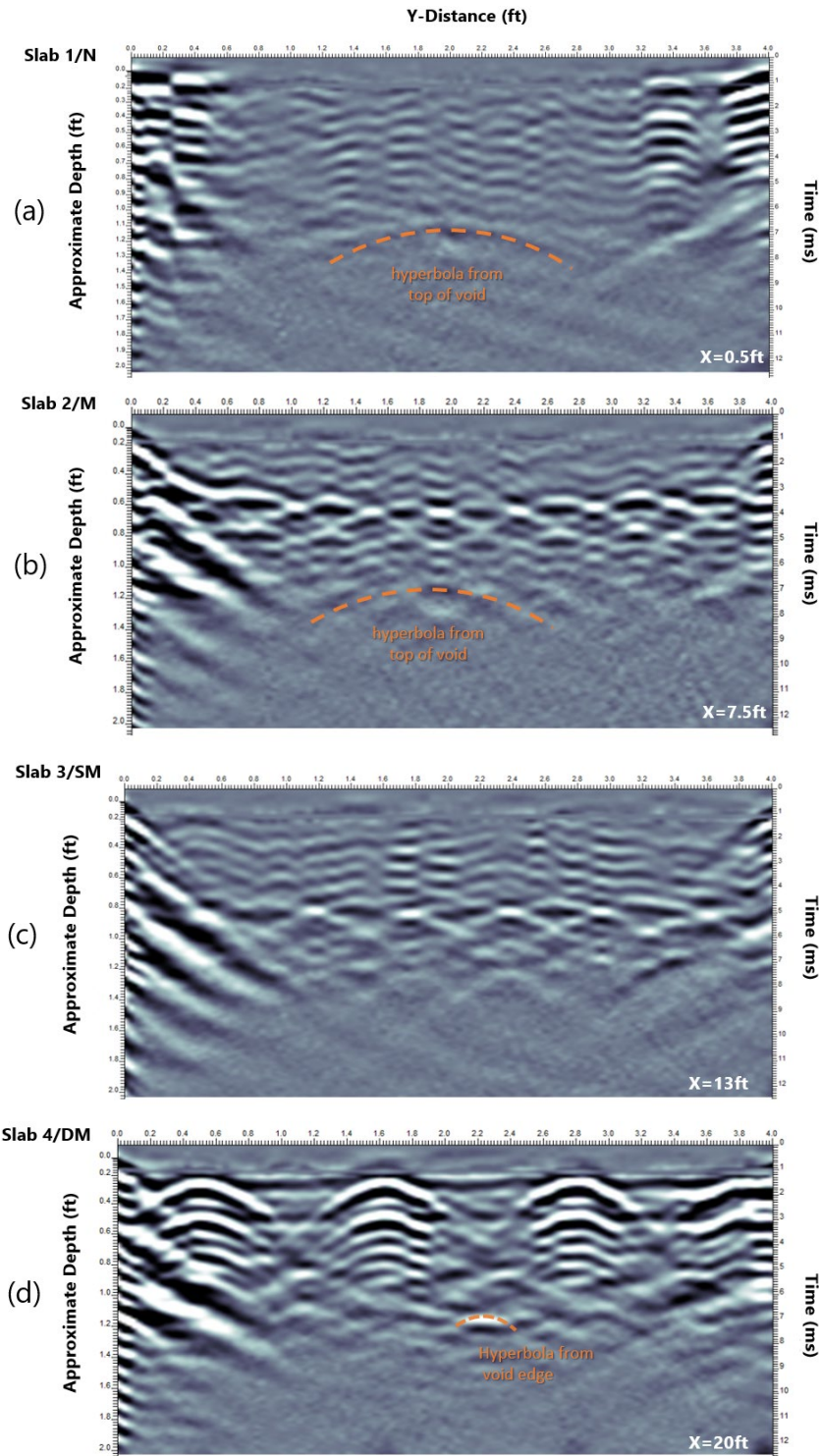


Figure 27.—Y-axis (short axis) GPR profiles across each concrete slab in Experiment 4 with a partially frozen water-filled void; the void centerline is at approximately $y = 2$ ft. Evidence of the void are interpreted in Slabs 1/N, 2/M, and 4/DM as hyperbolas from either the top of the void or the lateral edges of the void.

Detection of Voids Behind Spillways, Conduits, Canals, Tunnels, and Siphons

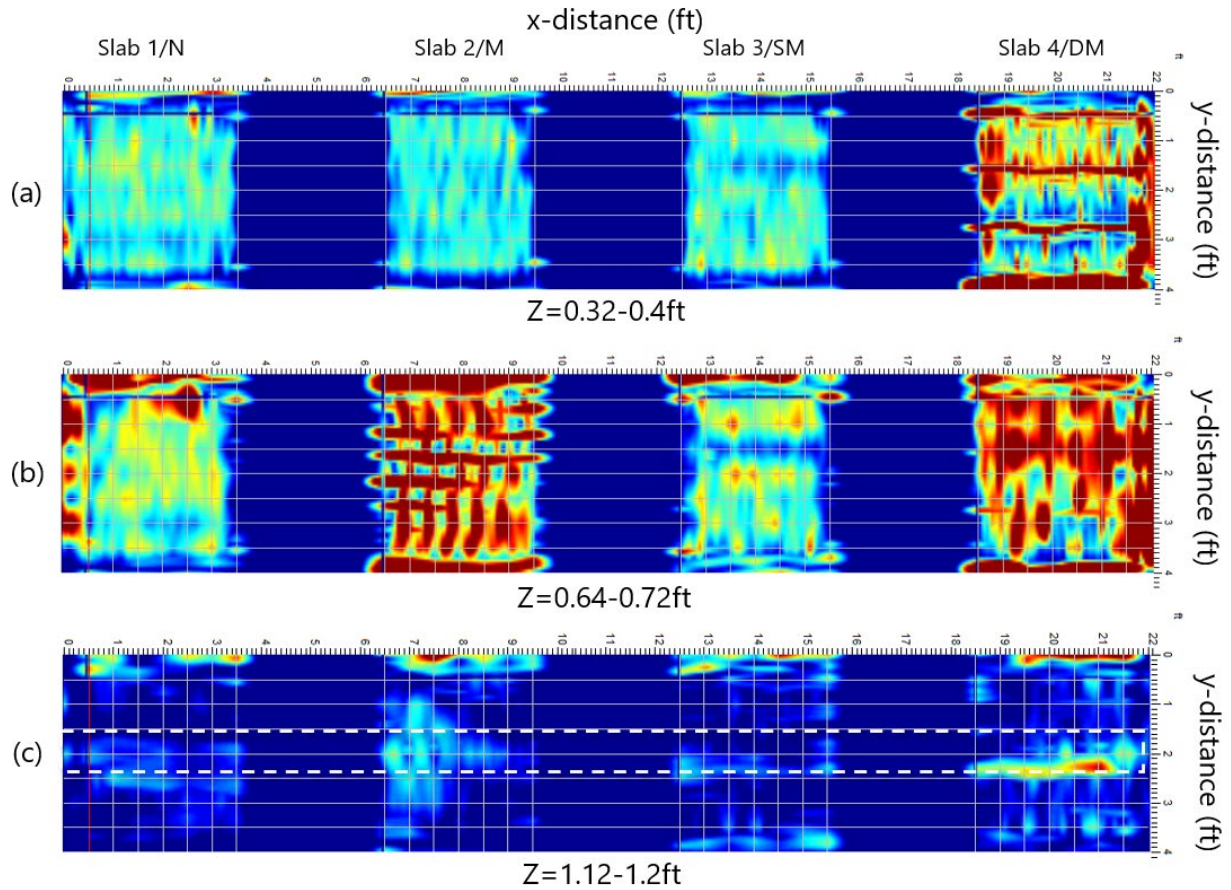


Figure 28.—Depth slices (plan-view profiles) from Experiment 4. Each depth slice includes all four concrete test slabs with varying types of reinforcement separated by a Styrofoam block. (a) The upper rebar mat is observed in Slab 4/DM at 0.36 ft depth. (b) the wire mesh and rebar mats are observed at approximately 0.7 ft depth. (c) the bottom of the slab is at approximately 1.15 ft depth. A longitudinal feature is observed below Slab 4/DM in the approximate location as the partially frozen water-filled void.

Detection of Voids Behind Spillways, Conduits, Canals, Tunnels, and Siphons

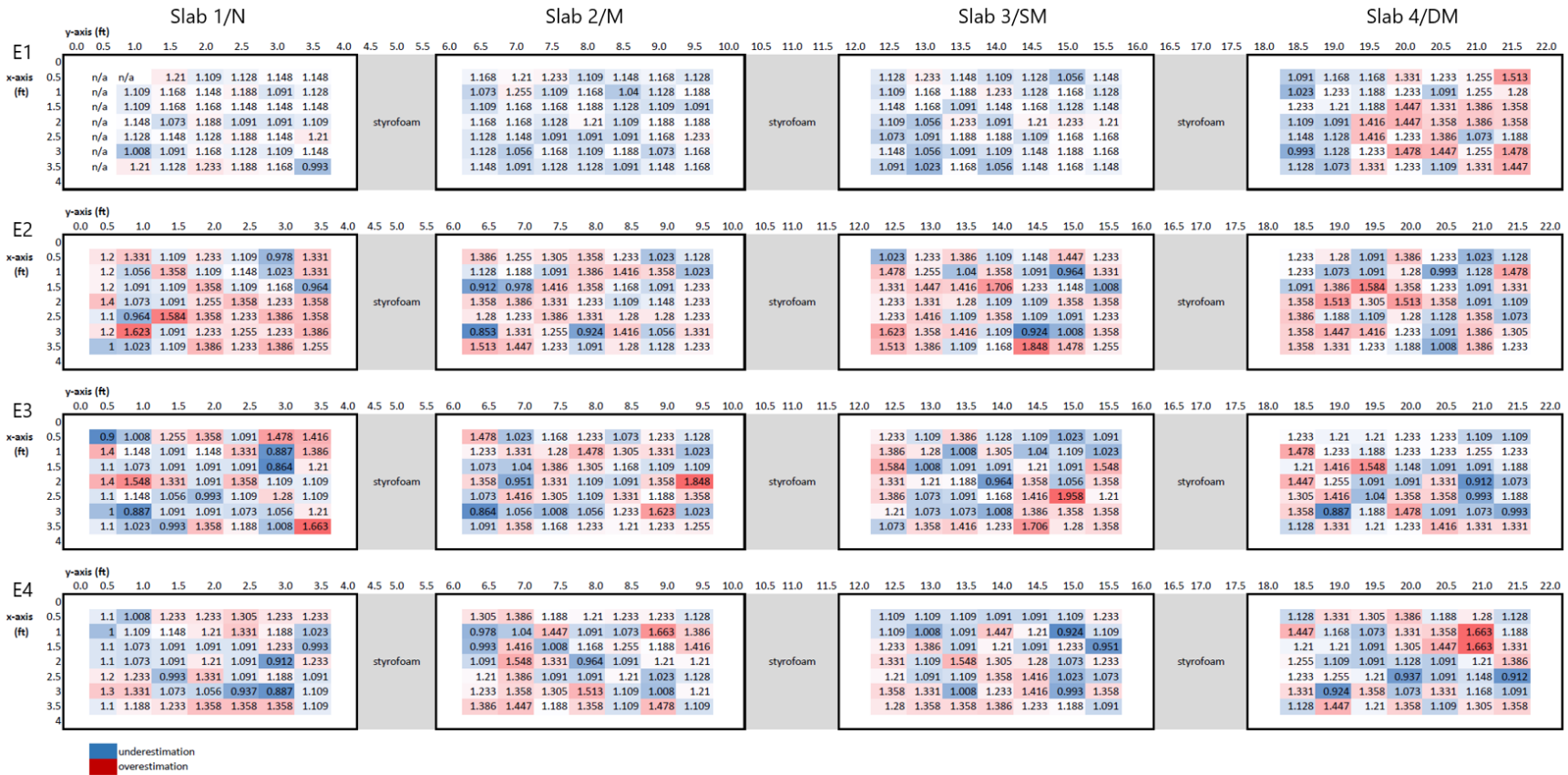


Figure 29.—IE results for each experiment and each slab. Warmer (redder) colors represent larger slab thickness estimates and cooler (bluer) colors represent smaller, or thinner, slab thickness estimates.

Detection of Voids Behind Spillways, Conduits, Canals, Tunnels, and Siphons

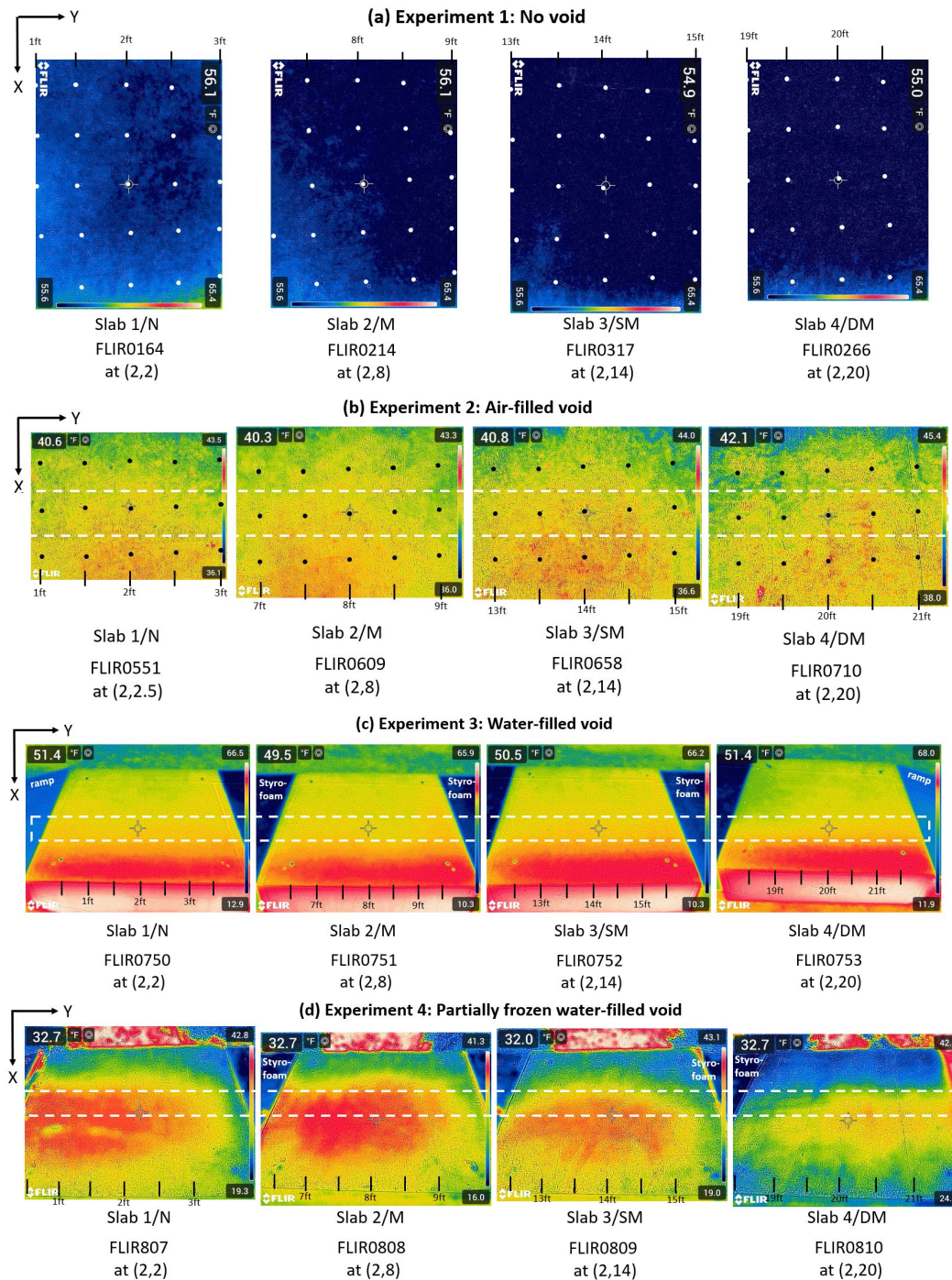


Figure 30.—(a) – (d) FLIR images of each slab for each experiment. An approximate grid and scale are overlaid on each FLIR image. The white dashed rectangle is drawn to indicate the approximate location of the subslab longitudinal void. N refers to no void, M refers to mesh reinforcement, SM refers to single rebar mat, and DM refers to double rebar mat. Temperature scales are listed on the right side of each image.

4.3 Experiment 3: A Canal Tunnel

4.3.1 Background

A Canal Tunnel is a concrete-lined irrigation tunnel in Klamath Falls, Oregon, and the California-Great Basin Region of Reclamation. It was constructed in 1906 as part of the Klamath Reclamation Project, one of the earliest Reclamation projects, to transport and provide water to the Klamath Basin. The tunnel is nearly 3300ft long (from sta. 17+60 to sta. 50+50) with a capacity of 1150 cubic feet per second and is primarily fed by the Klamath River and Upper Klamath Lake to irrigate approximately 63000 acres. The tunnel is 11ft tall and 13.5ft wide with an arched ceiling (crown) that is nearly 3.5ft tall. Based on as-built drawings, the concrete liner is 8 inches thick along the walls and crown. The invert (floor) is drawn as being 6 inches (0.5ft) thick, though it was resurfaced and raised in 2012 due to large scouting pits. No records were made available of this resurfacing. The concrete tunnel also possesses timber reinforcement behind most of the concrete liner (figure 31), though details about such reinforcement was not noted in construction drawings.

Geophysical surveys were requested by the Klamath Basin Area Office (KBAO) after KBAO personnel attended the Technical Tuesday presentation given by Evan Lindenbach and Sarah Rupert on this Science and Technology void research project. A Klamath Irrigation District report in 2021 noted the inlet and outlet for having extensive freeze thaw damage and spalling with various cracks, voids, leaking pipes, mineral build up, and heavy seepage areas observed in other sections of the tunnel. Therefore, TSC personnel were invited to perform geophysical surveys to detect and map other voids that are suspected behind the concrete liner. As a result, geophysical surveys were performed from January 31, through February 9, 2023, with the help of KBAO personnel. Similar damage to the tunnel structure was observed during data collection including voids, deteriorated timber and concrete (figure 31), mineral build up, and freeze thaw damage (figure 32).

Detection of Voids Behind Spillways, Conduits, Canals, Tunnels, and Siphons



Figure 31.—Photos of exposed timber reinforcement and varying degrees of concrete deterioration observed in A Canal Tunnel during data collection.



Figure 32.—Photos of tunnel conditions showing uneven concrete surface (top) and icy walls (bottom) due to the deterioration of the concrete.

4.3.2 Methodology

4.3.2.1 *Ground Penetrating Radar*

GPR surveys are non-invasive and non-destructive, and they allow for the canvassing of an extensive area in a relatively short amount of survey time in the field. GPR uses electromagnetic (EM) waves created by a transmitter antenna that are directed downward into the subsurface, reflecting off discrete objects and other boundaries where a change in the dielectric permittivity is present. These reflected EM waves then propagate back up to the ground surface where they are recorded by the receiver antenna of the GPR system. The time it takes for that EM wave to propagate down to a boundary and reflect back to the instrument is converted to a depth value after a two-way travel time and velocity calibration is calculated through data processing. The assessed propagation velocity can then be used to perform time-to-depth conversions. This velocity can also be used to perform reverse-time or Kirchhoff migration, which helps to focus the GPR image (e.g., collapses hyperbolas into points to reveal the true shape and location of reflectors at depth).

In the case of discrete objects (e.g., “reflectors”) such as a boulder, a hyperbolic reflection pattern is observed as the GPR system passes over these types of features. This hyperbolic data pattern is also generated when scanning across a metal pipeline in the perpendicular direction (i.e., scan line perpendicular to pipeline alignment). In the case of very closely spaced discrete objects or continuous interfaces (e.g., rebar matting or bedrock) a continuous GPR reflection (e.g., a reflection horizon) is observed in the recorded GPR 2-D profile. Both fixed and dynamic stacking were implemented during GPR surveys to maximize the signal-to-noise ratio (SNR) and the profile depth scale was approximated in the field using an appropriately assumed velocity model based GPR surveys performed at this site. This velocity model and depth estimation can be recalibrated in post processing, if necessary, and does not adversely affect the quality of the data set.

4.3.2.2 *Slab Impulse Response*

The SIR method is designed to detect voids beneath concrete slabs as well as areas with delamination if the damage is relatively shallow. It is considered a non-invasive and non-destructive testing method that utilizes a modified hammer to generate acoustic waves at multiple, densely spaced locations. The velocity of these acoustic waves from the hammer impacts are measured using a transducer, such as a vertical-component geophone or Wilcoxon, that is pressed firmly on the test surface (i.e., steel liner for this project). SIR is typically used on concrete slabs and retaining walls, pavement, runways, spillways, and tunnel liners.

These measurements are first plotted in the time domain as a function of wave amplitude to assess data quality. Multiple impacts can be performed at each grid location and stacked to improve signal quality and decrease noise. Once a stacked record is deemed acceptable, the velocity measurement is converted to the frequency domain to estimate the material’s average mobility (velocity/force) and flexibility (displacement/force) at each point location.

In general, areas possessing low mobility and low flexibility qualitatively suggest the material is more rigid and well supported (e.g., minimal to no delamination present) compared to areas possessing relatively high mobility and flexibility (less supported, voids may be present allowing

material to flex). These point measurements can be plotted as a two-dimensional (2-D) contour plot to map the average mobility; this allows a better visualization of the surveyed area and can be used to interpret the lateral extent of subsurface voids.

4.3.3 Data Acquisition

Fixed-offset cart-based GPR line data (2-D data) were collected using a Sensors and Software Inc. Noggin SmartHandle™ GPR system with a 1000MHz antenna (figure 33). The irrigation tunnel consists of 11 ft-tall vertical walls and a nearly 4ft-tall crown. Survey lines were oriented along the tunnel's long axis in the east-west (upstream-downstream) direction across the north wall (left embankment), south wall (right embankment) and tunnel crown. Surveys were performed with caution due to the environmental conditions inside the tunnel. Standing water was present in many sections and walls were often wet, covered in ice, or overrun with cobwebs (figure 33, figure 34). Geophysical surveys were performed under a confined space permit with personnel positioned on both sides of the tunnel throughout the duration of each workday.

Surveys were performed in 50-ft sections to keep consistent with observed survey markers that were mounted to the tunnel walls. Five horizontal lines were collected at 2ft vertical spacing across each tunnel wall and seven horizontal lines were collected at 2ft spacing across the tunnel crown, totaling 17 lines within each 50-ft section (figure 35). GPR data were collected across 48 sections; some sections were obstructed by thick ice across the tunnel floor and were therefore deemed unsafe to access. As a result, 2400 of the 3300ft-long irrigation tunnel was surveyed yielding approximately 40800 total line-feet of GPR data coverage over nine consecutive days.

Four slab impulse response survey grids were also performed in three sections of A Canal (figure 36). These sections include sections 11, 18, and 22 and were selected based on visual evidence of surface cracking and voids on and through the concrete wall. The grid locations and geometries for all SIR surveys are summarized in table 7.

SIR grid locations coincided with GPR surveys to allow for multi-method data correlation. Data points were collected in 0.5 to 1ft intervals across different tunnel facings to determine average flexibility and average mobility. In general, areas with observed higher mobility (i.e., material is less rigid) and higher flexibility (i.e., material has less foundational support) are more likely to possess voids. Voids were observed in various locations throughout the tunnel ranging in size from small cracks (<1in wide) to large holes (>1-2ft wide).

Detection of Voids Behind Spillways, Conduits, Canals, Tunnels, and Siphons

Table 7.—SIR Grid Geometrics

Grid No.	Section No.	Facing	Grid Size (ft)	Measurement Spacing (ft)
SIR Grid 1	11	North wall	12 x 5	1
SIR Grid 2	18	North wall	6 x 3	0.5
SIR Grid 3	22	South wall	9 x 5	0.5
SIR Grid 4	22	Crown	14 x 6	0.5

Detection of Voids Behind Spillways, Conduits, Canals, Tunnels, and Siphons



Figure 33.—Photos of Reclamation personnel performing GPR surveys on the tunnel walls.



Figure 34.—Photos of tunnel conditions showing cobwebs across ceiling with broken up icy floor (left) and deepening standing water (right).

Detection of Voids Behind Spillways, Conduits, Canals, Tunnels, and Siphons

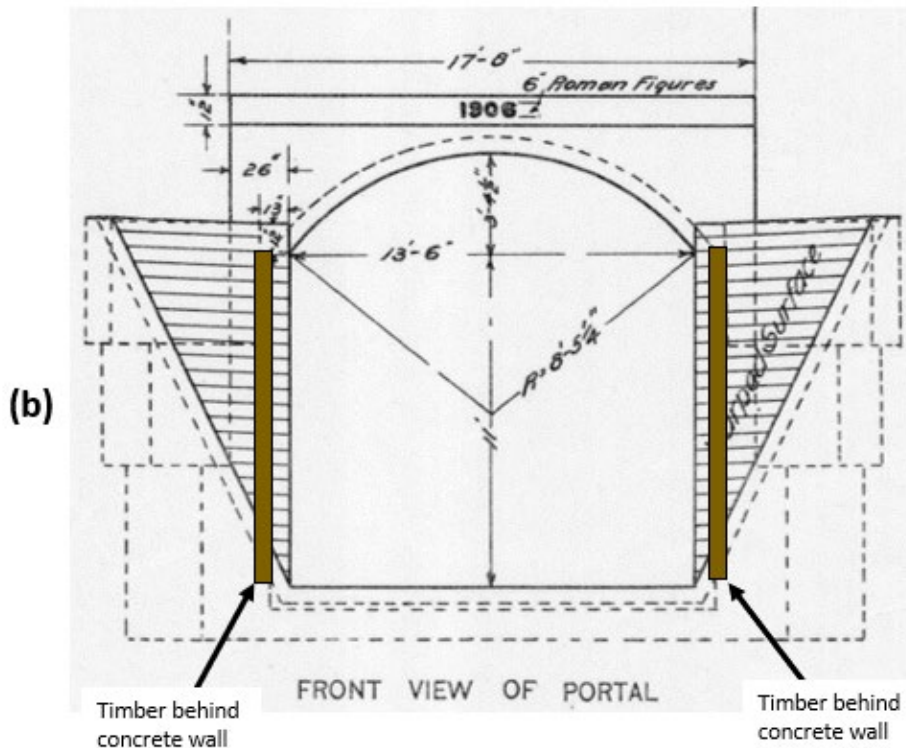
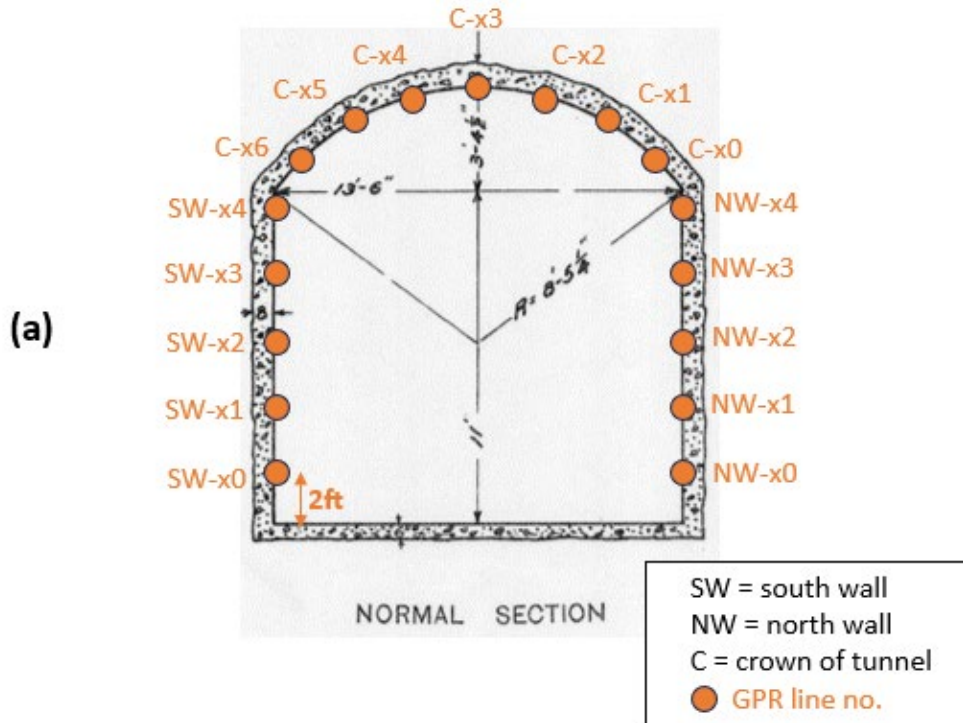


Figure 35.—(a) GPR survey line locations (orange) in A Canal Tunnel. (b) Schematic of A Canal Tunnel showing approximate locations of timber supports with respect to the sloped canal embankment walls. Figures are modified from Drawing No. 12-201-1766.



Figure 36.—Photo of Reclamation personnel performing one of the slab-impulse response surveys within A Canal.

4.3.4 Results

Summary table 8 provides an overview of GPR anomalies interpreted across multiple sections of the A Canal Tunnel. Anomalous features consistent with a void were observed in eight of the nine areas. Each section is also suspected to have deteriorated or missing timber beams behind the concrete walls. SIR surveys results indicate a few areas where voids may exist based on increased flexibility and mobility observed in each of the four grids; these SIR surveys were performed in the same sections as the presented GPR results. A more detailed analysis of these results and supporting figures are provided in the next subsections.

Table 8.—Summary table of interpreted GPR anomalies in a canal tunnel

	Section 11			Section 18			Section 22		
	North	South	Crown	North	South	Crown	North	South	Crown
Deteriorated Timber	Yes	Yes	Yes	Yes	Yes	Yes	Yes	Yes	Yes
Potential Void	No	Yes	Yes	Yes	Yes	Yes	Yes	Yes	Yes
Cracks	No	No	No	No	No	No	No	Yes	No
Metal Object	No	No	No	No	No	Yes	No	No	No

4.3.4.1 GPR

GPR survey lines are oriented downstream (DS) to upstream (US) from 0 to 50ft, respectively, along the tunnel walls. The A Canal Tunnel is divided into 50-ft sections and each section was labeled on the tunnel wall with a metal disc secured to the wall. A total 2400ft of the 3300-foot-long tunnel was surveyed using GPR and three sections are highlighted in this report including Sections 11, 18, and 22. Each vertical wall consisted of 5 survey lines and each line was separated vertically by 2ft starting from the bottom of each wall and moving upwards toward the crown. The crown consisted of 7 survey lines also with approximately 2ft line spacing.

GPR sections imaged 2.5 to 3ft of material from the tunnel surface and into the tunnel embankment. Therefore, GPR sections are oriented such that 0ft depth refers to the concrete wall surface with “depth” referring to distance into and behind the tunnel surface. Figure 37 illustrates the orientation of each GPR section in space, the orientation of each section varies depending on its location on the tunnel surface. The depth scale plotted on the vertical axis of each GPR section is calculated based on an assumed velocity model. For these sections, a 0.33ft/ns velocity model was used, which corresponds to the velocity of concrete. Given the variability in quality of concrete throughout the tunnel, some level of error may exist, therefore depth to interpreted features is approximate and may vary +/- 0.5ft.

GPR anomalies were interpreted and divided into three categories. The first feature is a shallow series of hyperbolas observed at approximately 5ft intervals and an estimated 4 ms, or < 1 ft behind the tunnel wall surface. These regularly occurring hyperbolas are likely associated with the presence of vertical timber beams that were installed during tunnel construction. The amplitude (e.g., brightness of these reflectors) of these hyperbolas may be related to the structural integrity of each timber beam. Those with less coherent, or lower amplitude signal are likely associated with beams that have broken or deteriorated. Timber beams suspected to be missing or damaged are marked with a yellow circle on all GPR sections.

The second feature appears as a horizontal and relatively consistent surface at an estimated 10-12ms, which is nearly 2ft behind the tunnel wall. It is important to note again that these depth calculations are approximate, and some level of error may exist that is ± 0.5 ft. This horizontal feature is likely associated with the slanted cutout wall of the canal and surrounding embankment. The amplitude of this horizontal feature varies between GPR sections because processing parameters were tuned to focus on interpreting the shallower timber beams and possible voids; this subsequently lessened the appearance of the deeper horizontal feature.

The third category consists of irregular anomalies that possess characteristics often associated with voids. These are represented by “ringing” signatures, which result from EM waves interacting with an air-material contact and echoing or reverberating in the open void space. Such features can be difficult to discriminate as the amount of ringing can depend on the size and depth of the void, the type of material the void is encased in, and the contents of the void. Voids at this structure exist as air-filled or ice-filled features based on visual inspection. Some voids may also be debris-filled depending on whether embankment material has sloughed, or timber beams have deteriorated and left gaps in the structure. These partially filled voids can appear as a collection of hyperbolic features due to the uneven surface of collapsed debris.

Detection of Voids Behind Spillways, Conduits, Canals, Tunnels, and Siphons

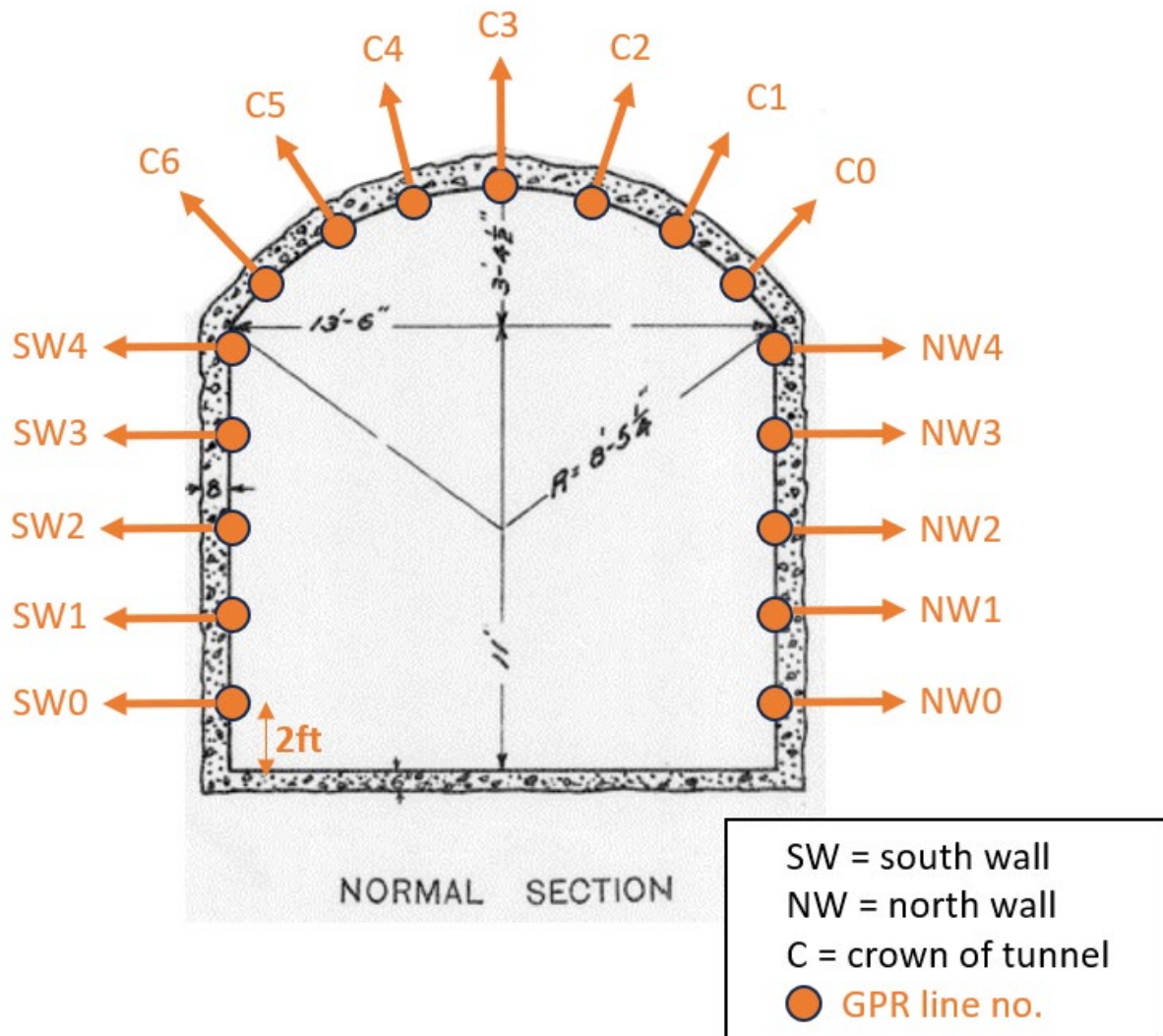


Figure 37.—GPR line names and each profile's depth orientation. Each orange arrow illustrates how depth projects into the subsurface behind the tunnel wall.

Section 11, North Wall

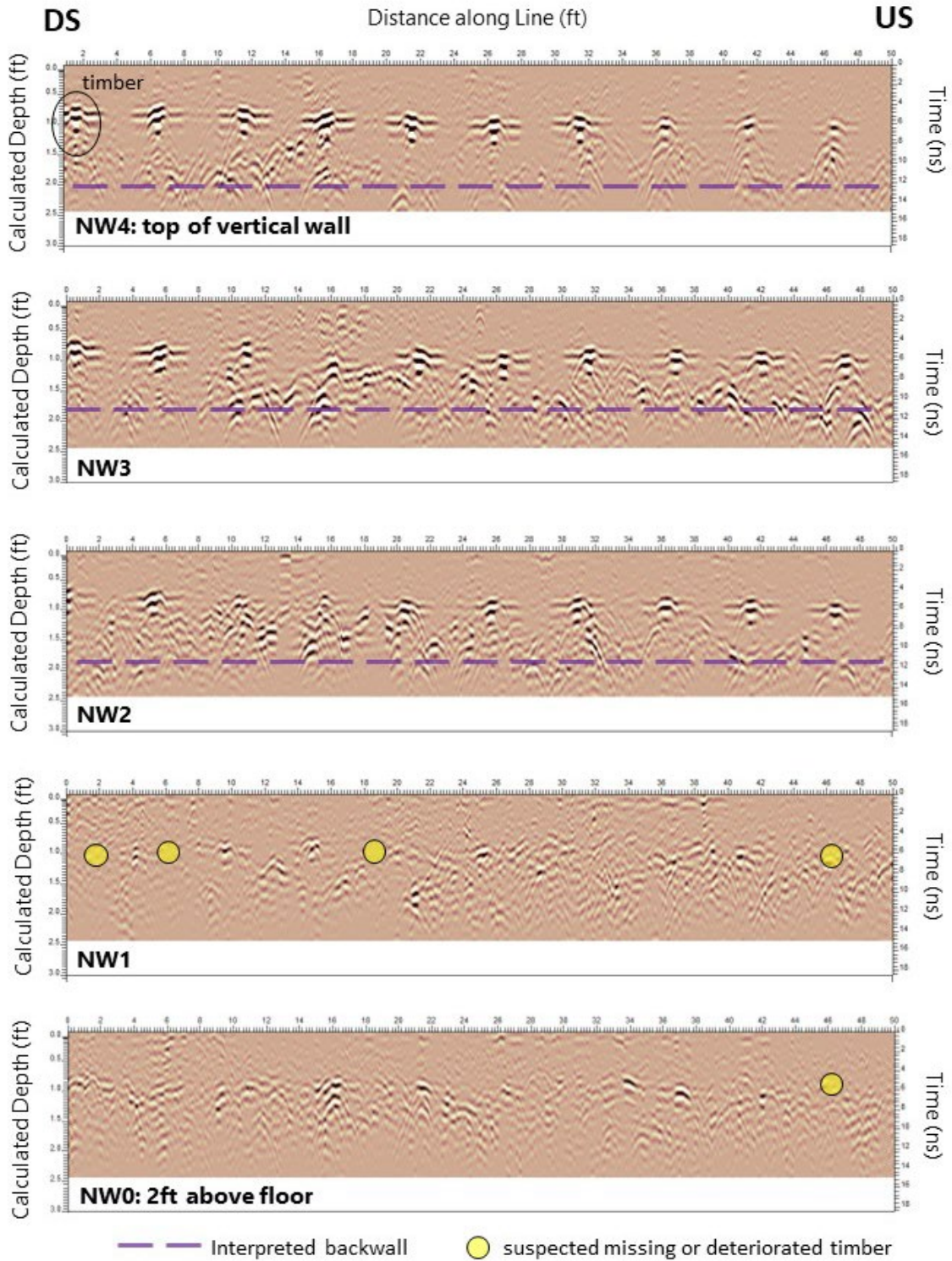


Figure 38.—GPR profiles from Tunnel Section 11 along the North wall. Each line has 2 ft vertical separation from the bottom of the wall (NW0) to the top of the vertical wall (NW4).

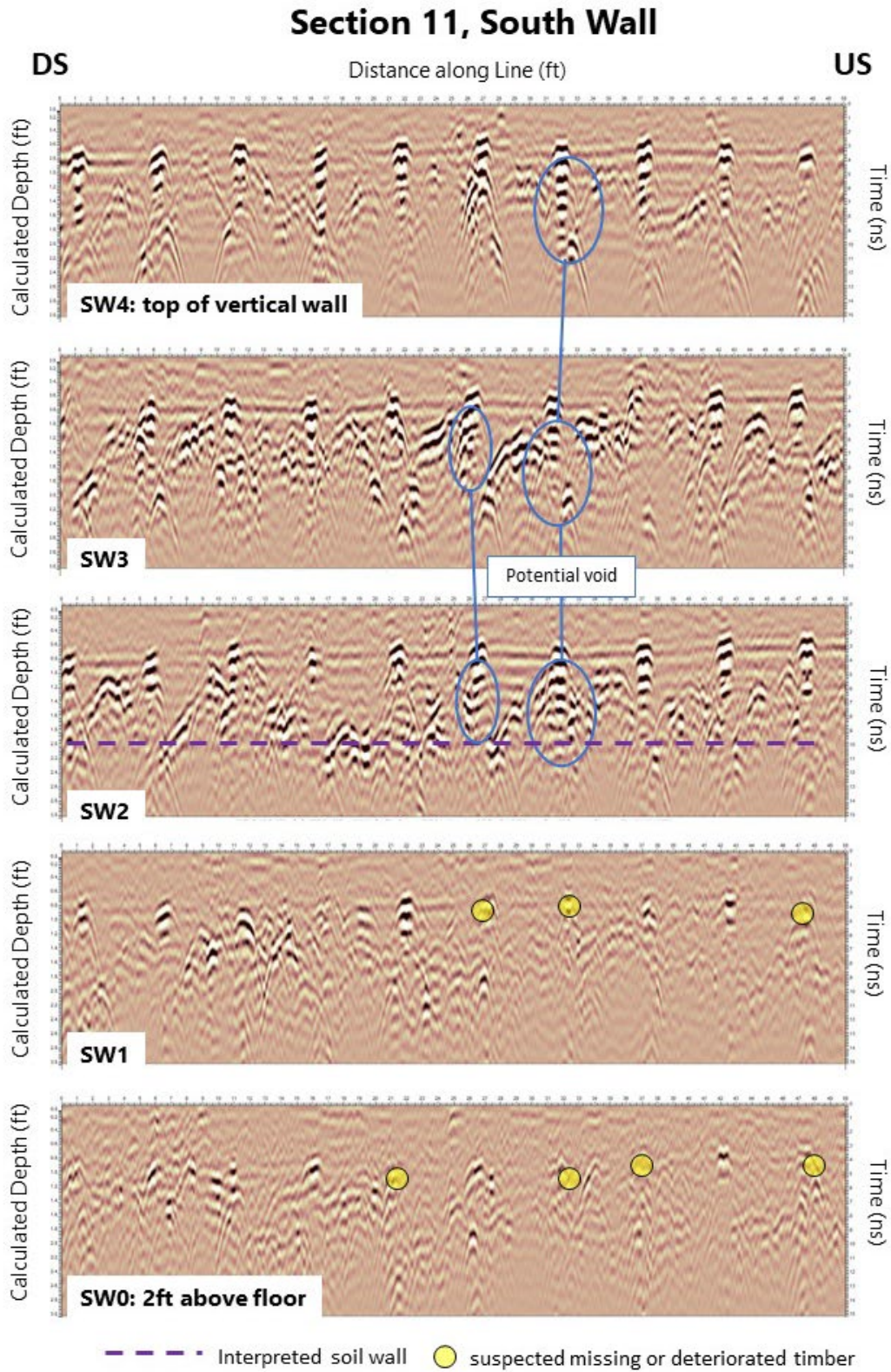


Figure 39.—GPR profiles from Tunnel Section 11 along the South wall. Each line has 2ft vertical separation.

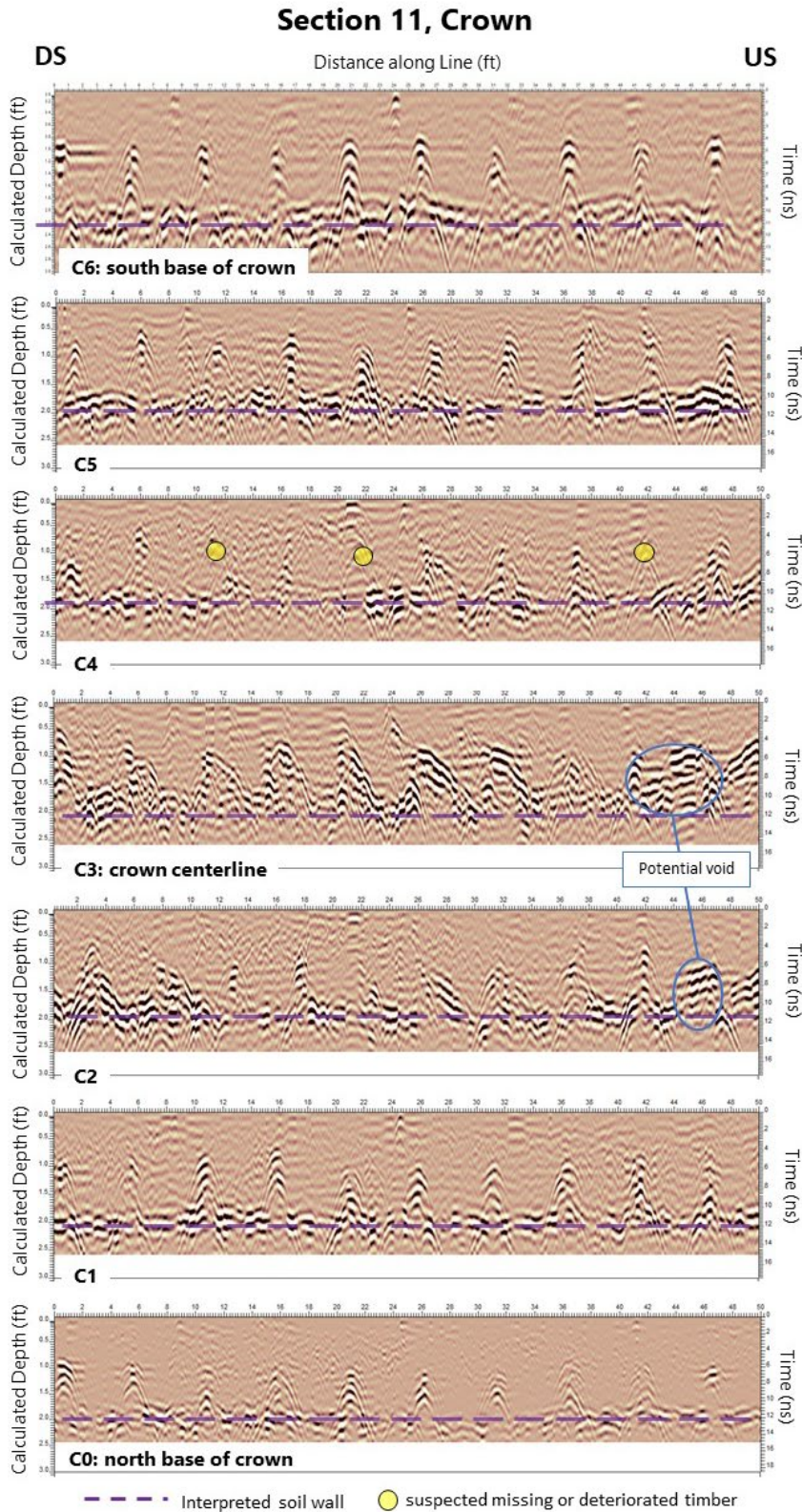


Figure 40.—GPR profiles from Tunnel Section 11 along the crown. Each line has 2 ft vertical separation.

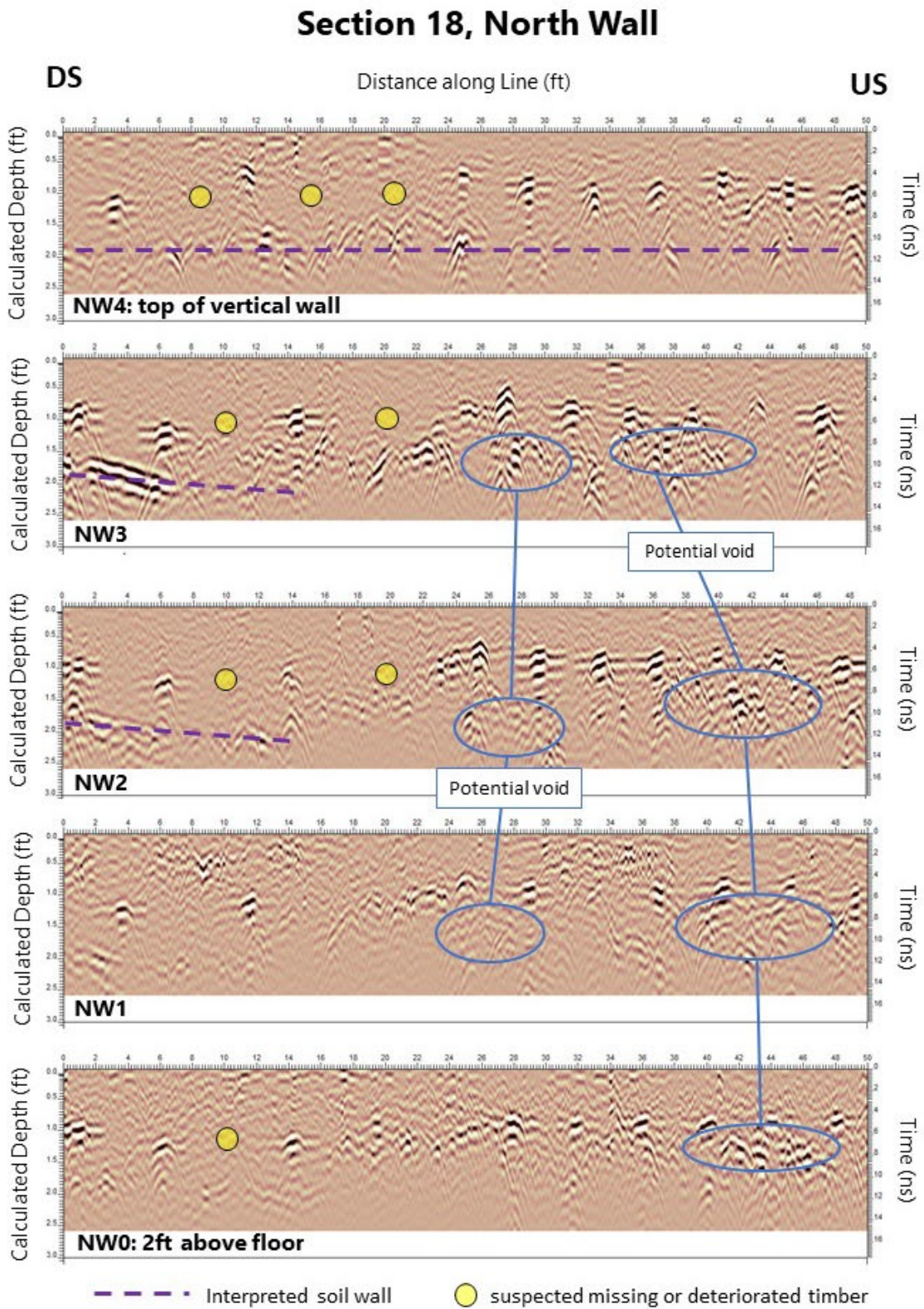


Figure 41.—GPR profiles from Tunnel Section 18 along the North wall. Each line has 2 ft vertical separation.

Section 18, South Wall

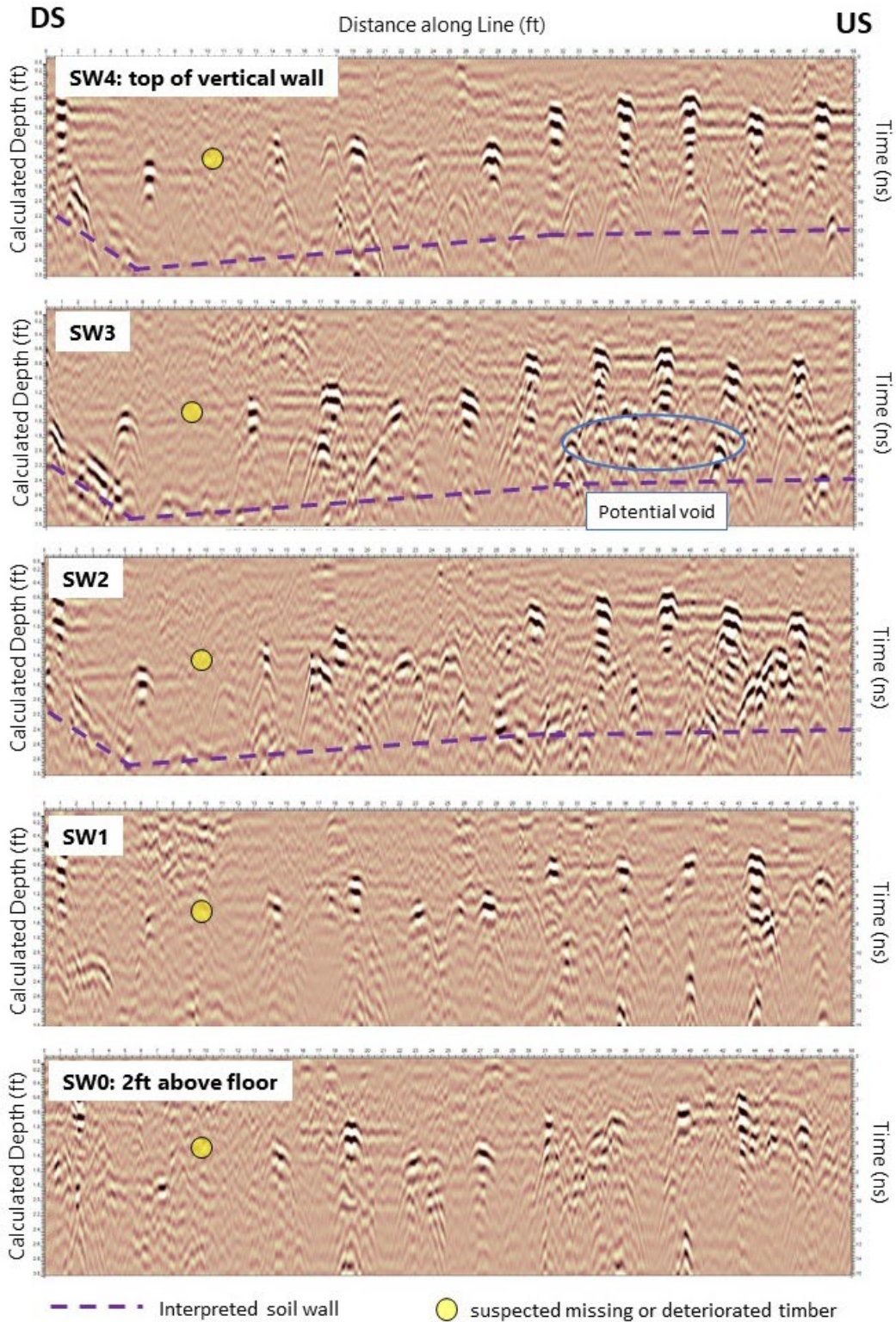


Figure 42.—GPR profiles from Tunnel Section 18 along the South wall. Each line has 2 ft vertical separation.

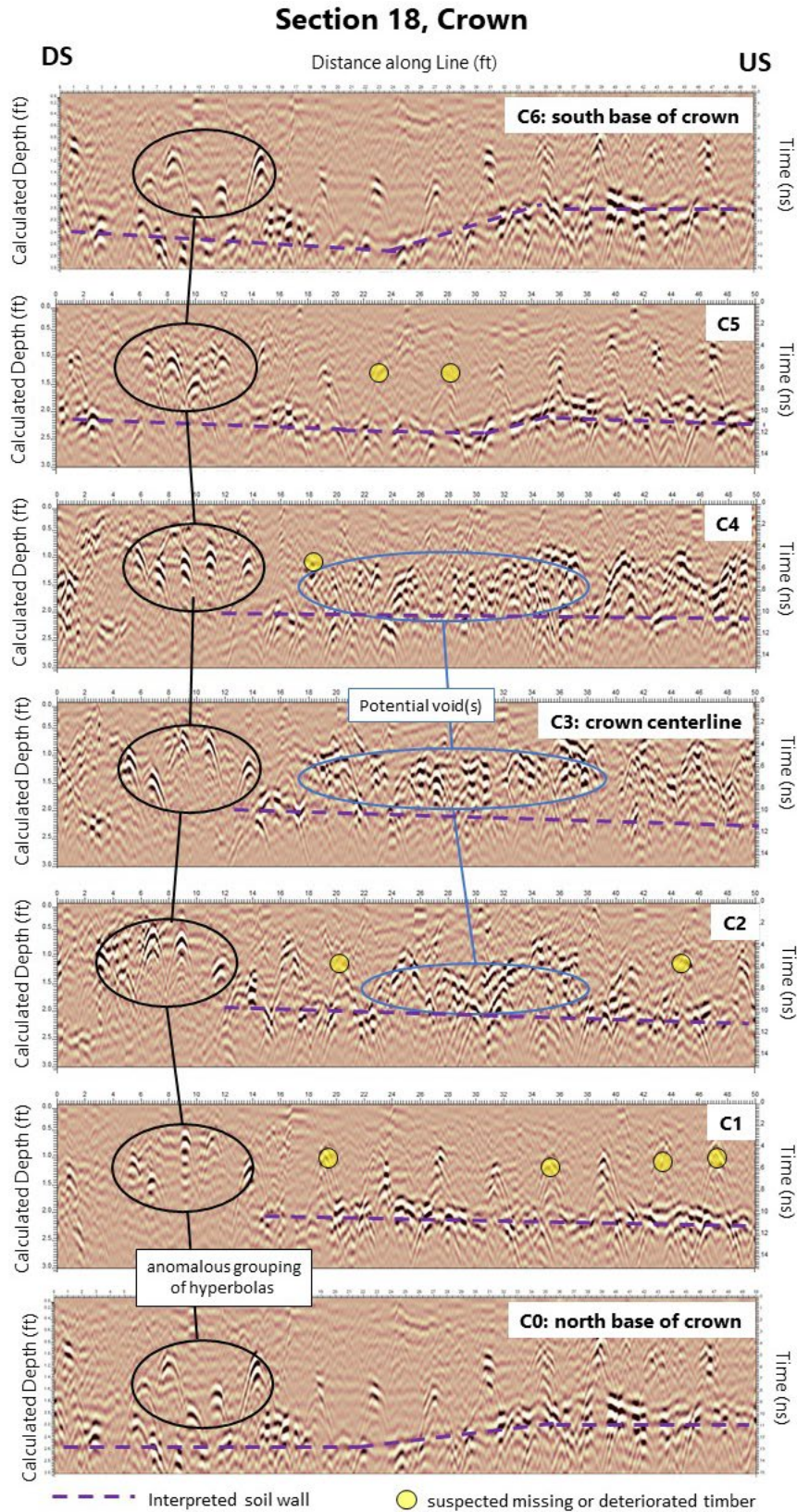


Figure 43.—GPR profiles from Tunnel Section 18 along the crown. Each line has 2 ft vertical separation.

Section 22, North Wall

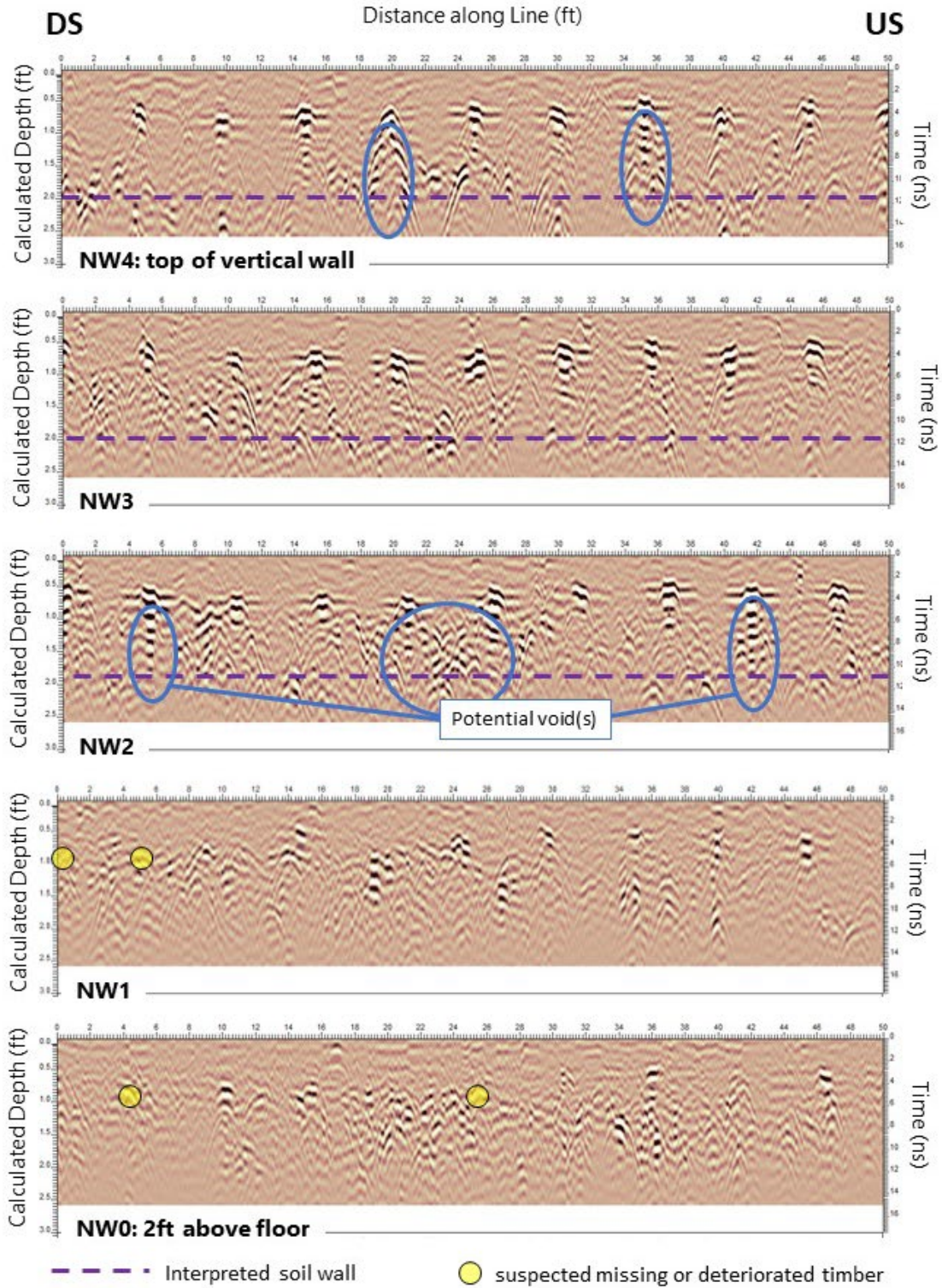


Figure 44.—GPR profiles from Tunnel Section 22 along the North wall. Each line has 2 ft vertical separation.

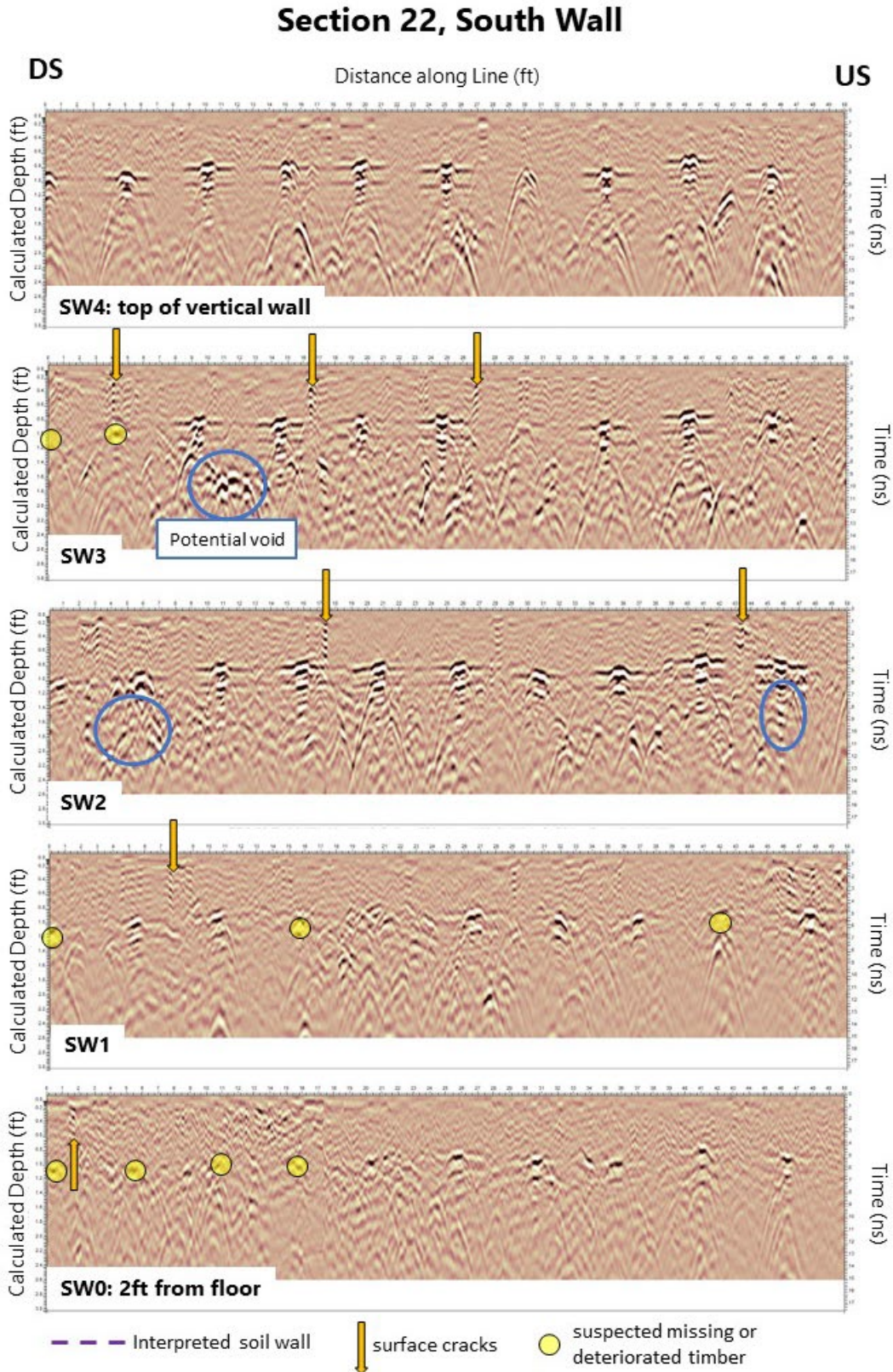


Figure 45.—GPR profiles from Tunnel Section 22 along the South wall. Each line has 2 ft vertical separation.

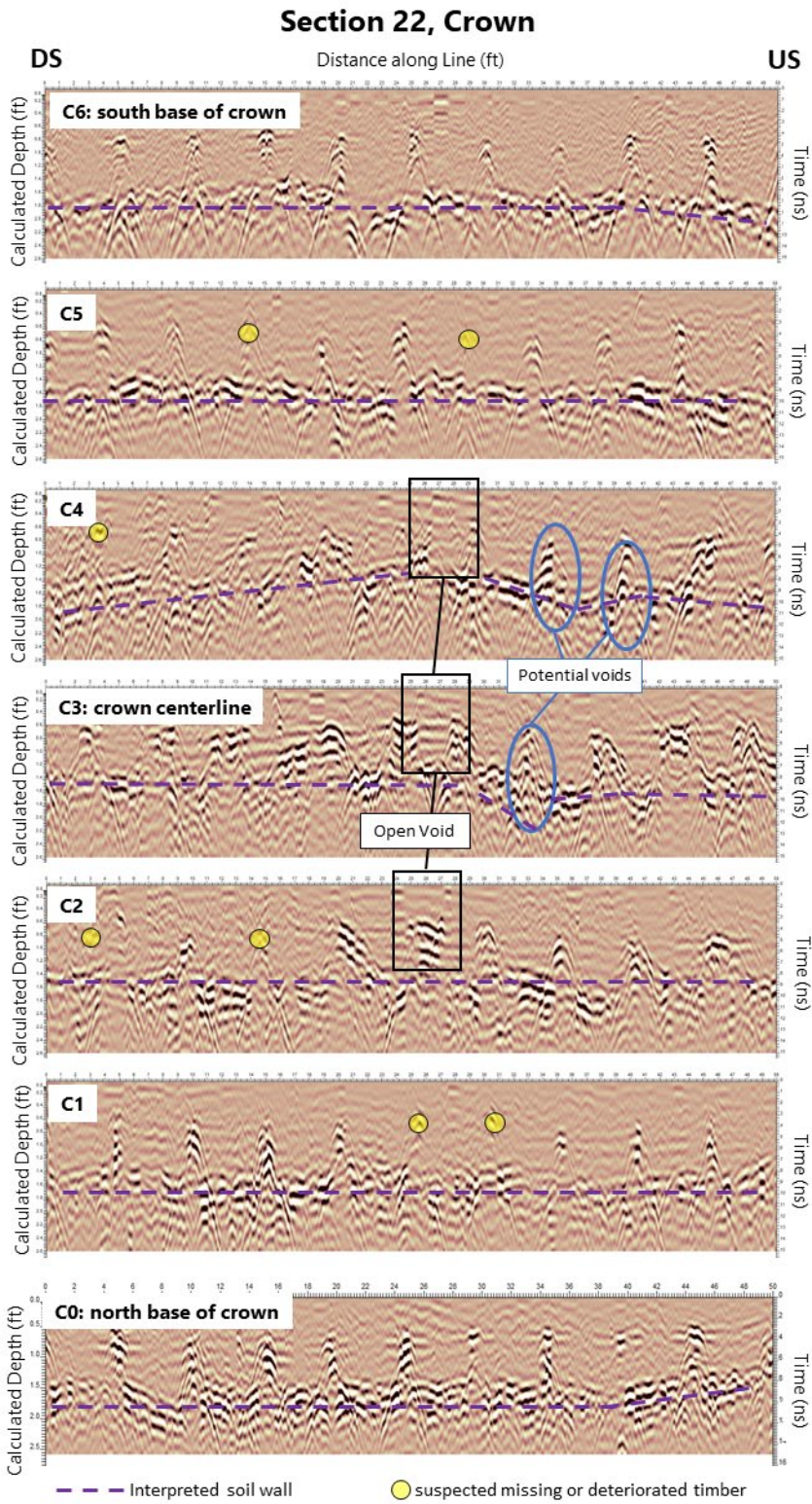


Figure 46.—GPR profiles from Tunnel Section 22 along the crown. Each line has 2 ft vertical separation.

4.3.4.2 SIR

Slab impulse response results were plotted in a similar coordinate system as the GPR results. The locations and grid geometries for all four SIR grids are listed in table 7. Areas possessing more competent concrete are characterized by a lower-amplitude flexibility peak and a smoother or low-amplitude mobility curve. Areas possessing less competent concrete are characterized by a higher-amplitude flexibility peak and a higher-amplitude, low-frequency mobility peak.

A 5ft tall by 12ft wide SIR survey (SIR1), with 1ft measurement spacing, was performed on the North wall of Section 11 where two cracks were visible on the concrete surface (figure 47); the location of this SIR grid overlaps with portions of GPR lines NW0, NW1, and NW2. In Section 11, the highest observed mobility values were in three areas along vertical $x=9\text{ft}$ and horizontal $y=0\text{ft}$ and $y=5\text{ft}$ (figure 48). These high mobility, high flexibility locations coincide with the visible surface cracks in figure 47. A portion of GPR Line NW0 was also noted for anomalous signatures that may be related to deteriorated timber beams behind the wall (figure 38), which may be contributing to these higher SIR values.

SIR2 was performed in Section 18 on the upper North Wall and lower Crown areas in a 3 ft tall by 6ft wide grid with measurements every 0.5ft (figure 49); this SIR grid overlapped GPR Lines C0 and NW4. Most notably, [5.5ft, 0ft] exhibited the highest mobility and flexibility measurement, suggesting this area to be less rigid than the surrounding surveyed area (figure 48). Multiple GPR lines taken along the North Wall and Crown were interpreted as possessing deteriorated or missing timber beams in this section (figure 41, figure 43). An anomalous grouping of hyperbolas was observed in all GPR sections on the Crown, which may be related to the less rigid area interpreted in the SIR2 grid $x=2.5\text{ft}$. These hyperbolas are consistent with metal objects or pipes and its possible that material surrounding these objects may have shifted causing its background material to weaken.

The SIR3 survey consisted of a 5ft tall by 9ft wide grid with measurements every 0.5ft along the South Wall in Section 22 (figure 51); this grid overlapped portions of GPR Lines SW0, SW1, and SW2. Four areas across the lower half of the survey grid possessed increased average flexibility and mobility (figure 52), which are located between GPR Lines SW1 and SW0. This lateral area of higher SIR values can be attributed to the noisy data portion of GPR Line SW0, between 2-10ft (figure 45) which suggests the concrete wall may possess a more heterogeneous consistency (e.g., different, or larger aggregate) than has been observed in other sections.

Lastly, SIR4 was positioned across the Crown in Section 22 where a large hole and void was present. This 6ft tall by 14ft wide grid with measurements every 0.5ft coincided with GPR Lines C0 through C6 (figure 53); no photo is available of the grid area in the tunnel. The location of this open hole and void coincides with the SIR anomaly (e.g., red-colored area) located in the $y=5.5\text{ft}$ line from $x=1$ to 3ft with slightly increased values radiating laterally outwards across the arched surface of the crown. This is consistent with the approximately 2ft-wide anomaly observed on GPR Lines C2, C3, and C4 (figure 46). This weakened, or less rigid area, is likely related to the void spanning a larger area than is exposed on the crown wall.

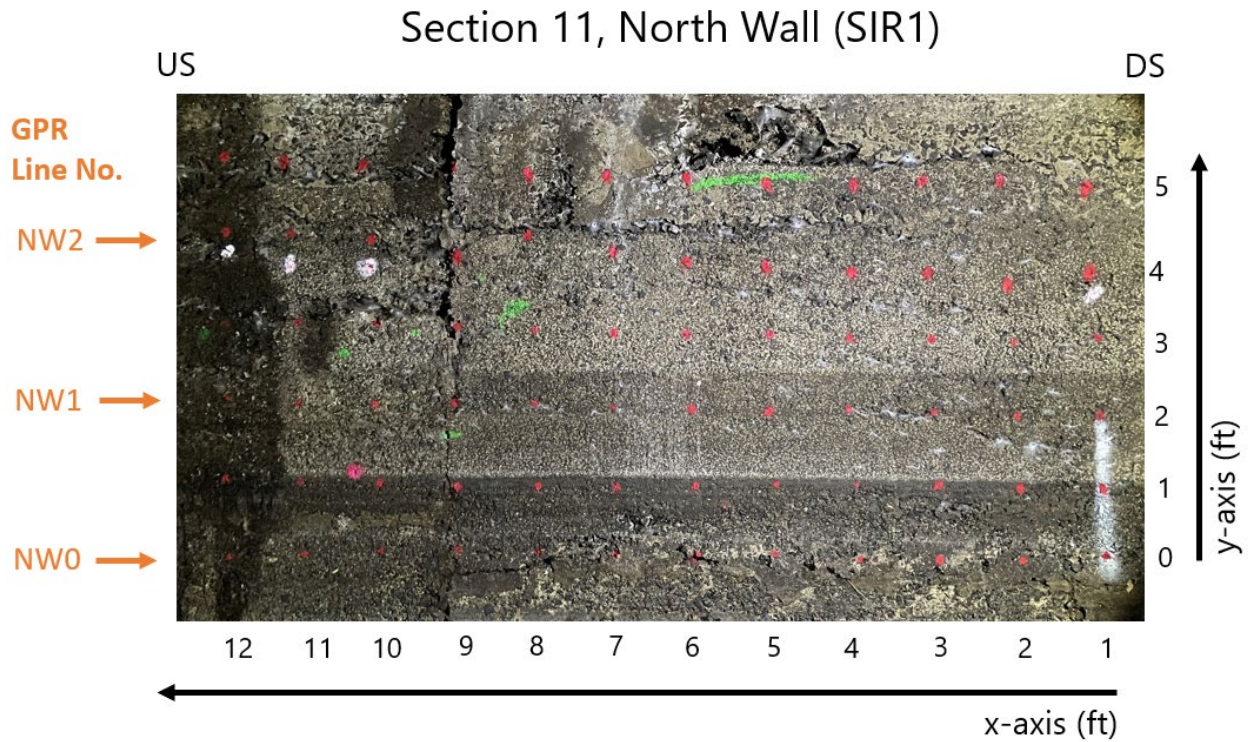


Figure 47.—Photo of SIR1 grid area consisting of a 5 ft by 12 ft grid with measurements every 1 ft. This area possesses noticeable surface cracks along $x = 9$ ft and $y = 5$ ft. $x=0$ ft accidentally not included in photo.

Detection of Voids Behind Spillways, Conduits, Canals, Tunnels, and Siphons

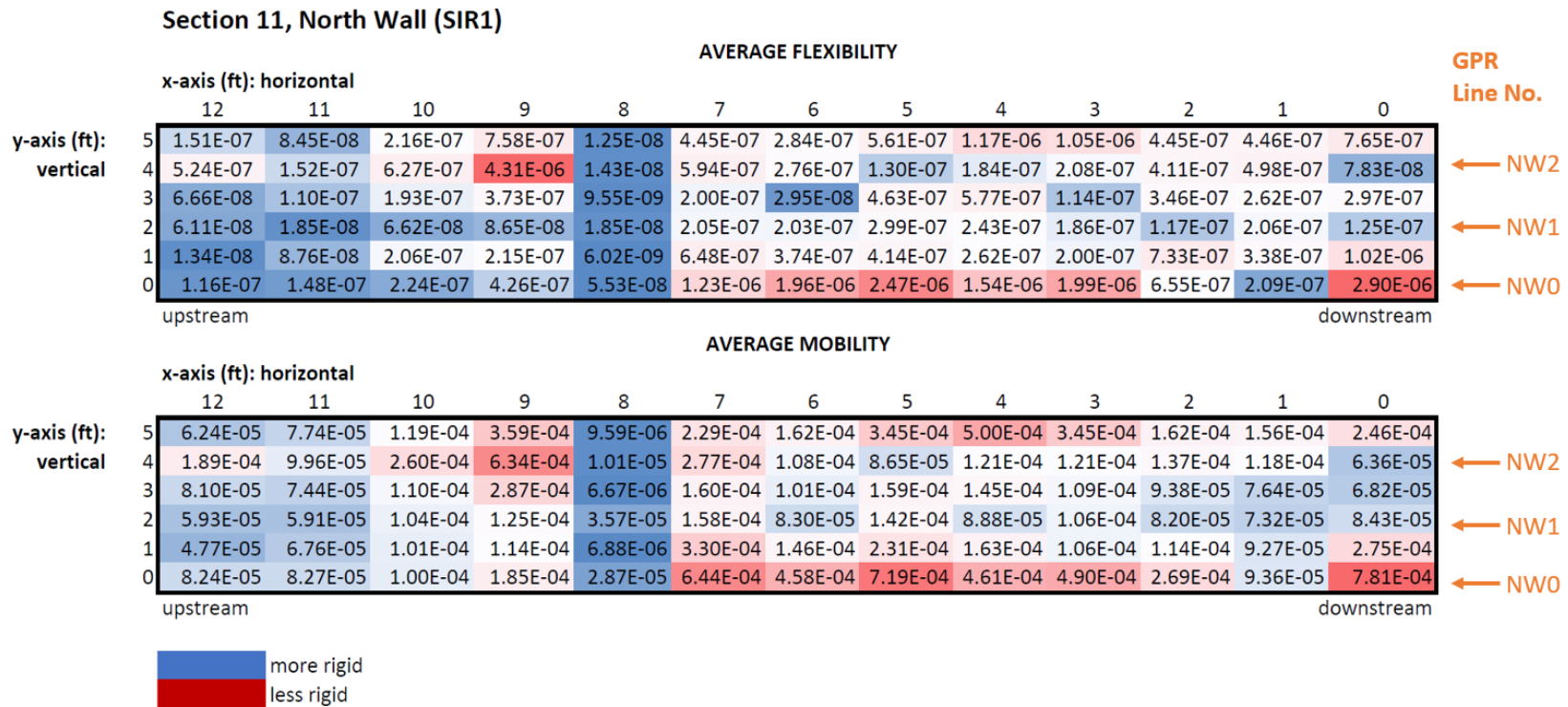


Figure 48.—SIR1 results from the North Wall of Section 11 where more rigid areas are colored in blue and less rigid areas are colored in red.

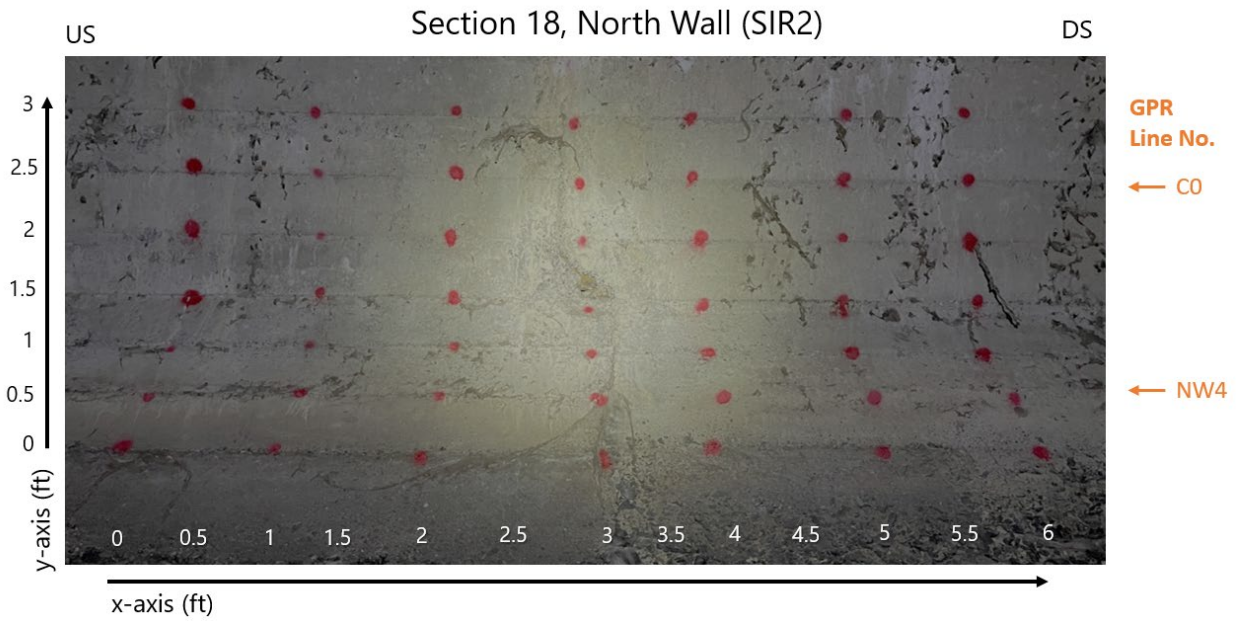


Figure 49.—Photo of SIR2 grid area consisting of a 3 ft by 6 ft grid and measurements every 0.5 ft.

Detection of Voids Behind Spillways, Conduits, Canals, Tunnels, and Siphons

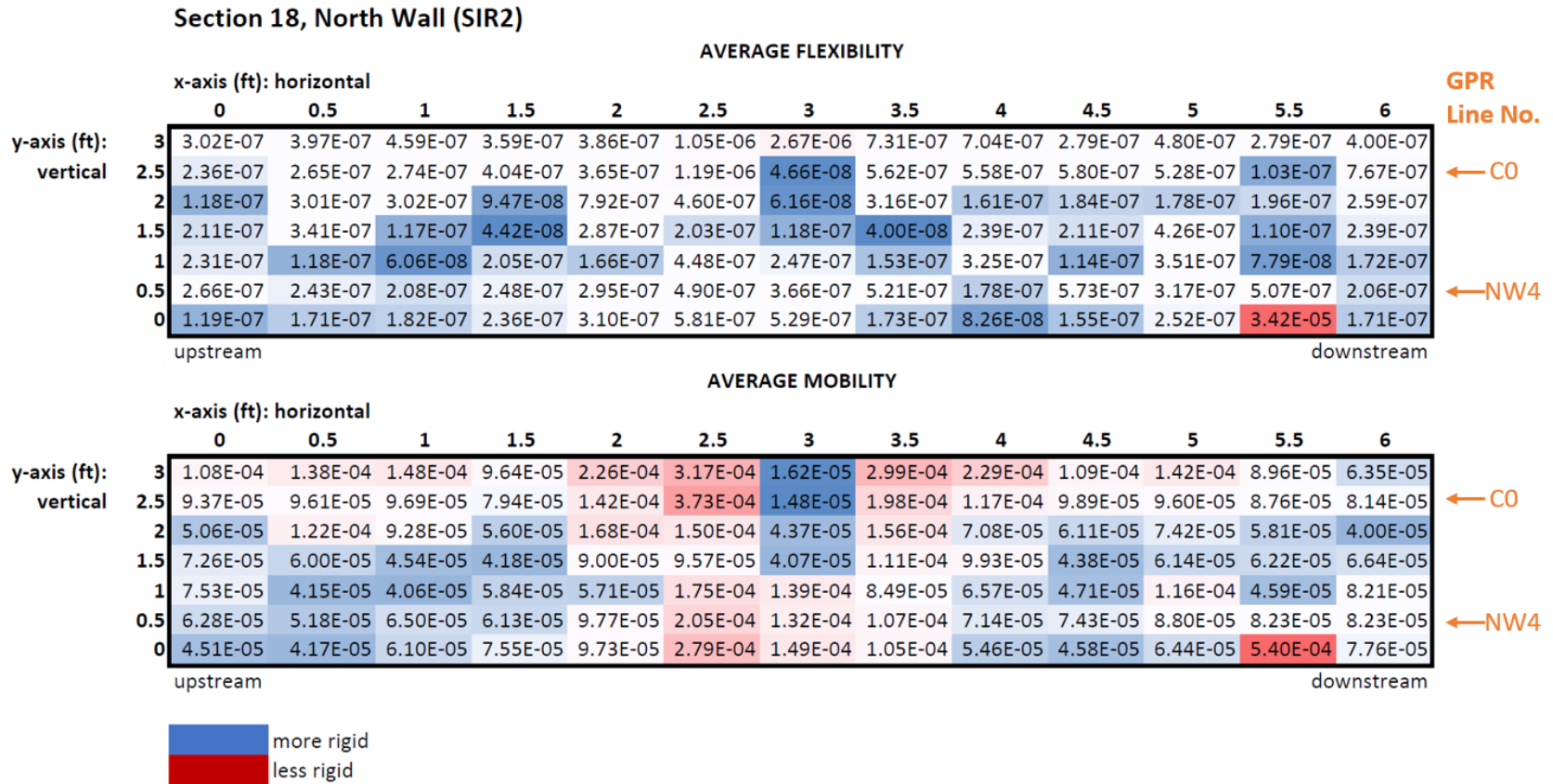


Figure 50.—SIR2 results from the North Wall of Section 18 where more rigid areas are colored in blue and less rigid areas are colored in red. This grid overlaps with portions of GPR Lines C0 and NW4 in this tunnel section.

Section 22, South Wall (SIR3)

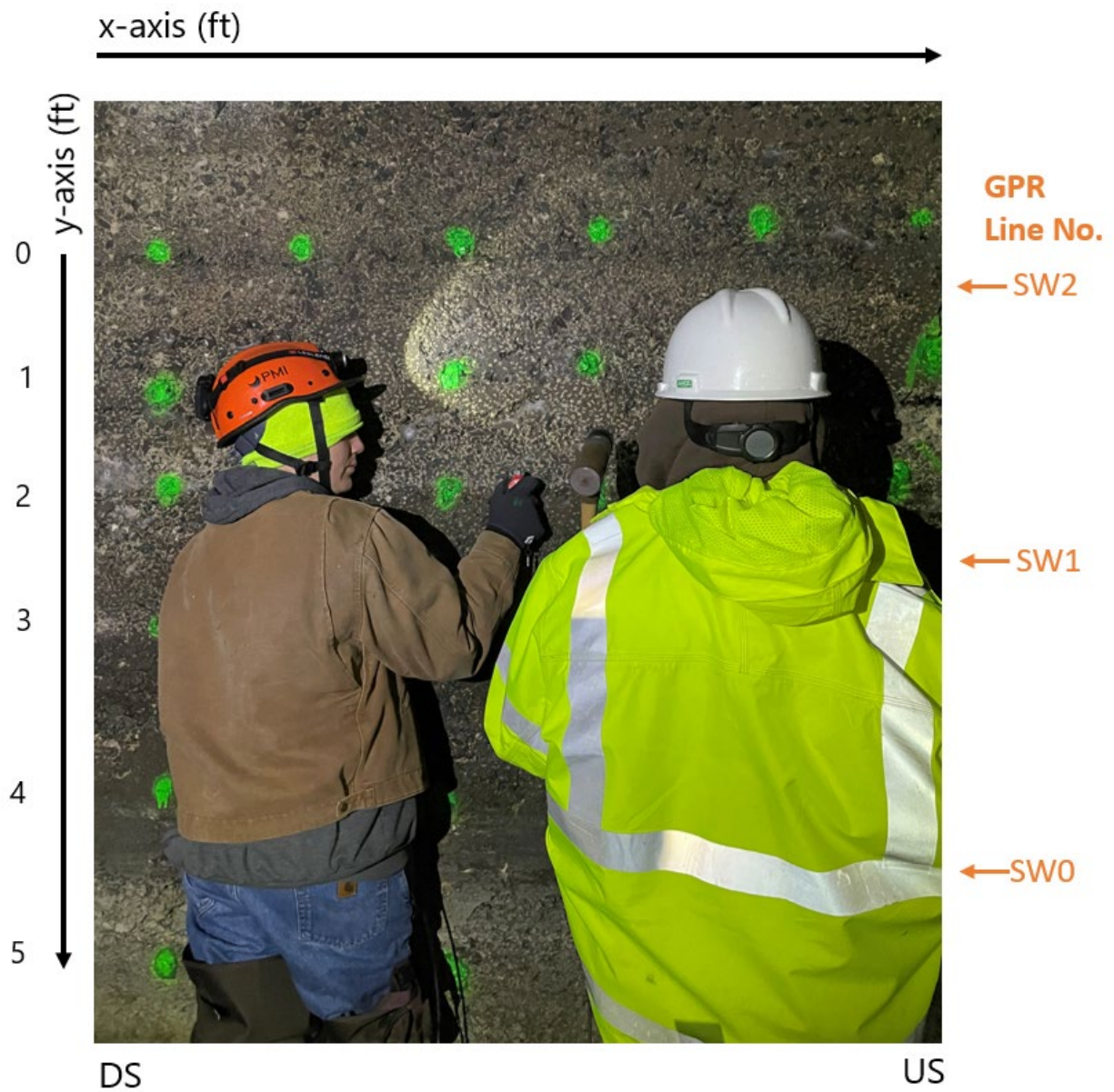


Figure 51.—Photo of SIR3 survey grid area consisting of a 5 ft by 9 ft wide grid with measurements every 0.5 ft.

Detection of Voids Behind Spillways, Conduits, Canals, Tunnels, and Siphons

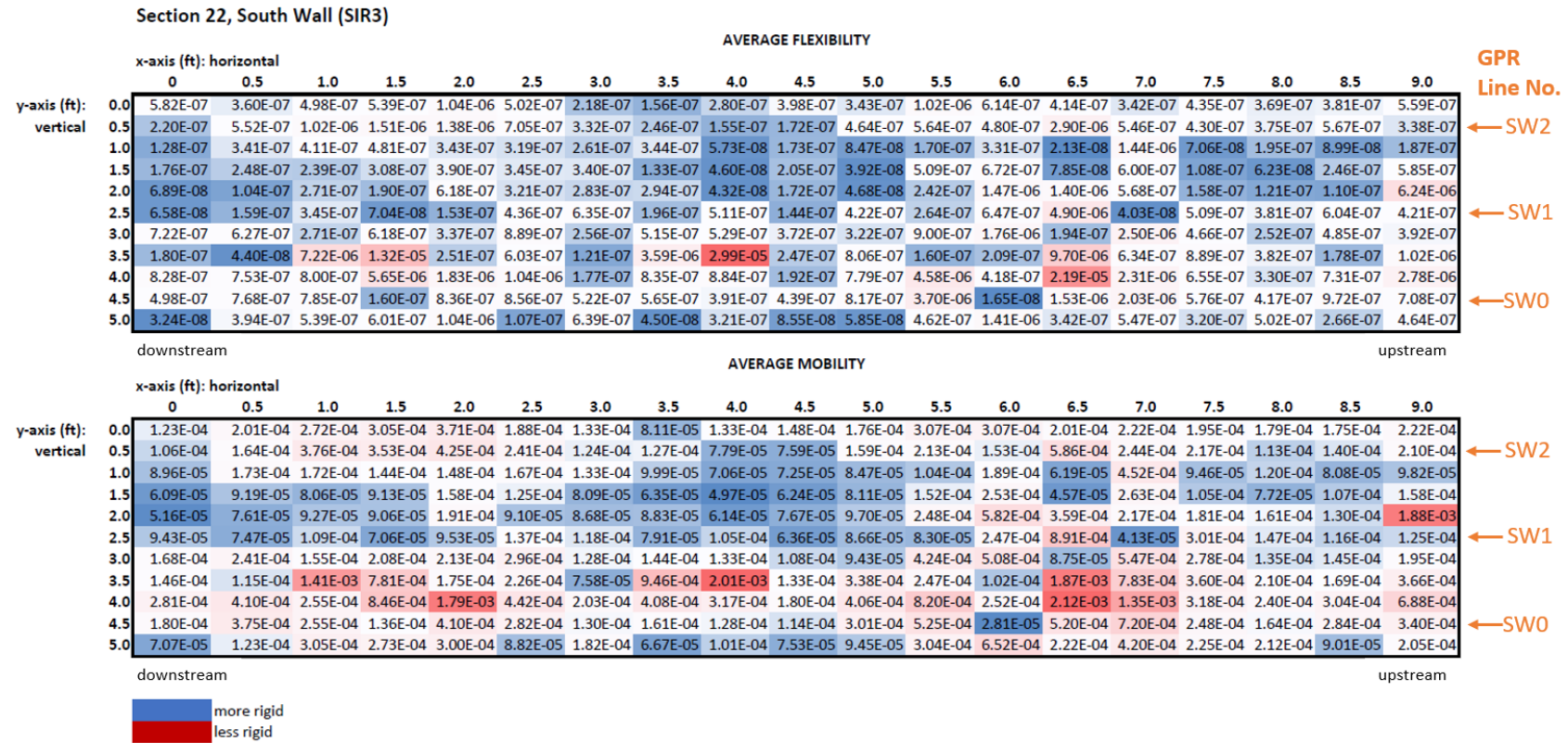


Figure 52.—SIR3 results from the South Wall of Section 22 where more rigid areas are colored in blue and less rigid areas are colored in red.

Detection of Voids Behind Spillways, Conduits, Canals, Tunnels, and Siphons

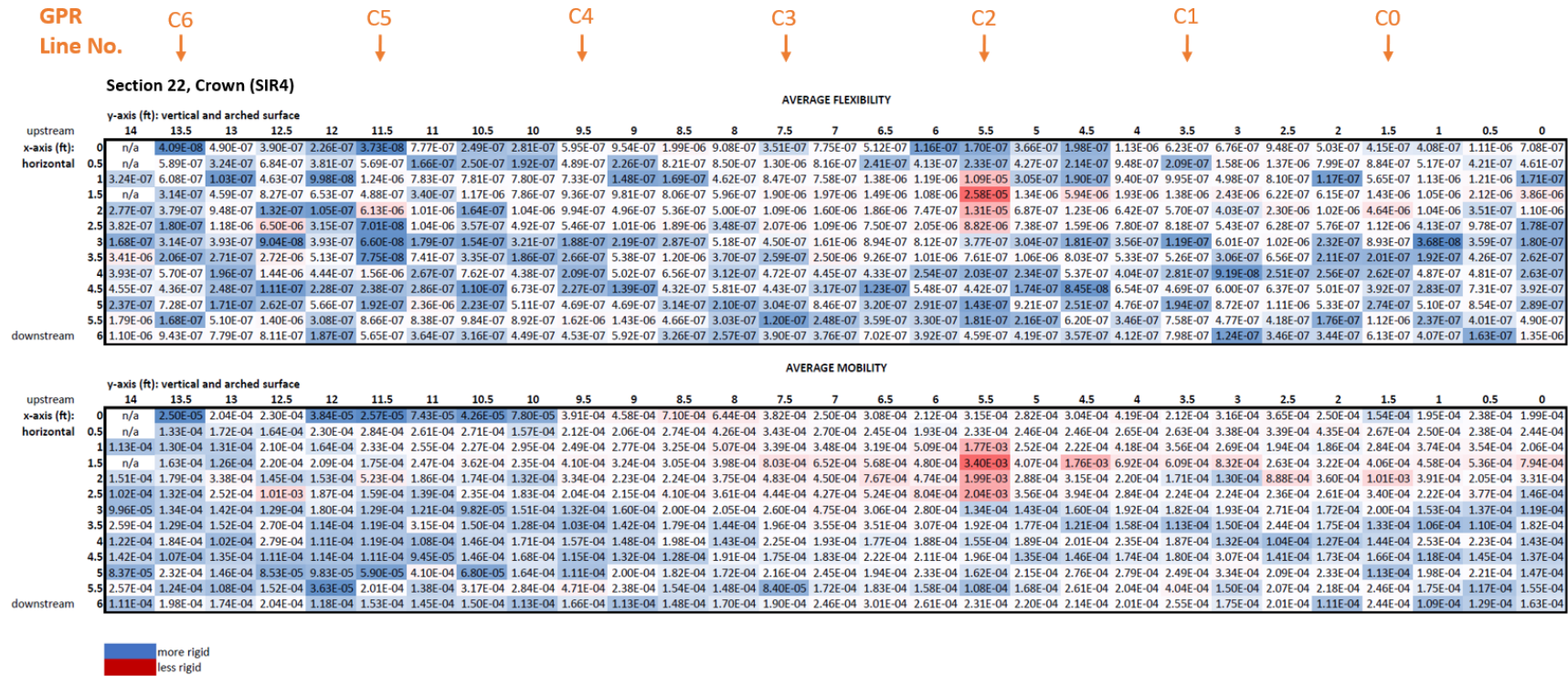


Figure 53.—SIR4 results from Section 22 with GPR line locations labeled across the grid. More rigid areas are colored in blue and less rigid areas are colored in red.

5.0 Conclusion

5.1 Experiment 1

A series of non-destructive testing (NDT) methods were performed inside the steel-lined portion of a hydroelectric turbine draft tube to detect voids. These voids have been allowing leakage and liner movement within surrounding concrete causing safety concerns within the facility. NDT methods considered for this study included slab-impulse response (SIR), impact echo (IE), and ultrasonic pulse echo (UPE). The IE and UPE methods were deemed unsuitable for this field study based on the poor quality of the recorded data sets and the variable thickness of the concrete foundation.

Based on SIR results, the topmost 1.5ft of the steel-lined tube wall had higher-amplitude flexibility peak responses and higher-amplitude, lower-frequency mobility peak responses compared to the lower 4.5ft of the surveyed area in the tube. This upper area with the highest observed mobility was generally consistent with the results of the soundings audibly heard when striking the steel with a mechanics hammer to manually map areas of suspected hollowness. The following year, the steel liner was regouted throughout the suspected area and another SIR survey was performed following its completion to re-assess for voids and decoupling. As a result, the amplitudes of flexibility and mobility peaks were greatly reduced in this upper portion compared to the initial survey. This suggests that the grouting successfully repaired the decoupling between the steel liner and concrete foundation and that the SIR method proved to effectively inform engineers about the structural health of this vertical draft tube.

5.2 Experiment 2

An outdoor experiment was designed to evaluate how effectively different geophysical methods can detect voids beneath concrete slabs with varying reinforcement and weather conditions. Overall, anomalous features consistent with a void were more commonly observed in GPR profiles perpendicular to the longitudinal void than profiles parallel or along the void. Evidence of ringing was apparent in GPR sections from Experiment 2 (air-filled void) and Experiment 3 (water-filled void). A high-amplitude longitudinal feature was observed below the single rebar mat concrete slab because of this more prominent ringing during Experiment 2 with a similar feature observed during Experiment 3; feature was at approximately 1.1-1.2ft depth. Most notably, a high-amplitude longitudinal feature was observed below the double rebar mat concrete slab during Experiment 4 when the void was filled with partially frozen water.

Results of the IE survey did not yield a specific indication of a void along a specific alignment or beneath any of the tested slabs. Measurements taken across slabs 1, 2, and 3 yielded relatively consistent slab thickness estimations (i.e., 1-1.14ft) during Experiment 1, when no subslab void was present, which is consistent with the thickness of the concrete slab observed in GPR sections. However, IE measurements taken across slab 4 with the double rebar mat yielded a significant overestimation of slab thickness (i.e., 1.25-1.5ft). Based on these IE measurements, increasing amounts of reinforcement can cause additional resonance of acoustic waves and

subsequently an overestimation of slab thickness. It appears the double rebar mat adequately reinforced the slab and reduced the effects of subslab voids (unsupported areas) on the concrete slab. Slab 4 displayed great performance in minimizing slab deflection, but ultimately reduced the likelihood of detecting a void beneath it.

The FLIR surveys suggest that thermography may be better suited for void detection during colder temperatures whose voids are possibly related to freeze-thaw. During Experiment 4, the thermal anomaly across slab 2 had the highest increase in temperature whereas the thermal anomaly across slab 4 had the lowest increase in temperature. This suggests that the mesh reinforcement may have allowed the slab to better maintain a higher temperature in the partially frozen water-filled void compared to the double rebar mat reinforcement; thus, a temperature anomaly related to the warmer air in the void was more apparent under these conditions.

5.3 Experiment 3

Experiment 3 consisted of a series of GPR surveys and co-located SIR grids used to detect voids within or behind the concrete tunnel wall as well as evaluate the health of vertical timber reinforcement. Three tunnel sections were surveyed including Sections 11, 18, and 22. Each section was divided into 3 areas: the North Wall, South Wall, and Crown, with a total of (17) 50-ft-long GPR profiles per section.

In general, GPR anomalies consistent with a void were observed in eight of the nine areas. Each tunnel section is also suspected to have deteriorated or missing timber beams behind the concrete walls, which likely contributes to the increased presence of voids. SIR survey results also indicate a few areas where voids may exist based on increased flexibility and mobility observed in each of the four grids; these focused SIR surveys were performed in the same sections as the presented GPR results. Other features interpreted in GPR profiles and SIR grids are cracks in the concrete wall and the trapezoidal soil wall that backfills between the concrete and natural environment. The thickness of this backfill appears to vary across GPR profiles which may be related to difficulty excavating the volcanic bedrock during construction (e.g., uneven bedrock surfaces).

Overall, multiple anomaly signatures were interpreted on GPR profiles and SIR grids, many of which were associated with known voids, and others where the presence of voids is unknown. The GPR method also proved successful in this environment despite being in an enclosed area where vertical walls and ceilings can cause unwanted noise in GPR profiles.

6.0 References

- [1] Akkaya, Y., T. Voigt, K.V. Subramaniam, and S. P. Shah. 2003. Nondestructive measurement of concrete strength gain by an ultrasonic wave reflection method: *Materials and Structures*, 36, 507–514.
- [2] Al-Shayea, N., R. Woods, and P. Gilmore. 1994. SASW & GPR to detect buried objects: Symposium on the Application of Geophysics to Engineering and Environmental Problems, EEGS. Expanded Abstracts, 543–560. <https://doi.org/10.4133/1.2922086>.
- [3] Aoike, K., Saito, H. and T. Inazaki. 2013. An evaluation of void thickness using a database of void wave-forms extracted from GPR data. 11th SEGJ International Symposium, 98–102.
- [4] Belesky, R.M. and H.R. Hardy Jr. 1986. Seismic and microseismic methods for cavity detection and stability monitoring of near-surface voids. 27th U.S. Symposium on Rock Mechanics, ARMA, 248–258.
- [5] Cassidy, N.J., R. Eddies, and S.Dods. 2011. A comparison between GPR and ultrasonic techniques for void detection beneath reinforced concrete sections. 17th EAGE European Meeting of Environmental and Engineering Geophysics, <https://doi.org/10.3997/2214-4609.20144415>.
- [6] Chen, D.H. and T. Scullion. 2008. Detecting subsurface voids using ground-coupled penetrating radar. *Geotechnical Testing Journal*, 31, no. 3, 1–8.
- [7] Diamanti, N. and A.P. Annan. 2019. Understanding the use of ground-penetrating radar for assess clandestine tunnel detection. *The Leading Edge*, 38, no. 6.
- [8] Gelis, C., D. Leproux, J. Virieux, A. Bitri, S. Operto, and G. Grandjean. 2005. Numerical modeling of surface waves over shallow cavities. *Journal and Environmental and Engineering GEOPHYSICS*, 10, no. 2, 111–121.
- [9] Grandjean, G., and D. Leparoux. 2004. The potential of seismic methods for detecting cavities and buried objects: experimentation at a test site. *Journal of Applied Geophysics*, 56, no. 2, 93-106. doi: 10.1016/j.jappgeo.2004.04.004.
- [10] Greenfield, R. J., P.M. Lavin, and R.R. Parizek. 1976. Geophysical Methods for Location of Voids and Caves. 121st International Association of Hydrological Sciences Proceedings of the Anaheim Symposium, 465–484.
- [11] Hickey, C.J. 2012. Rapid Assessment of Potential Hazards in Levees and Earthen Dams: SERRI Report 2010 90034–001.

Detection of Voids Behind Spillways, Conduits, Canals, Tunnels, and Siphons

- [12] Hickey, C.J., D.R. Schmitt, J.M. Sabatier, and G. Riddle. 2009. Seismic measurements for detecting underground high-contrast void. *SAGEEP*, 929–936.
- [13] Hollema, D.A. and L.D. Olson. 2004. Application of a combined nondestructive evaluation approach to detecting subgrade voids below a dam spillway. *SAGEEP*, 1059–1070.
- [14] Hutchinson, P.J. 2008. Electrical imaging of deep clay-mine voids. *SAGEEP*, 274–279.
- [15] Ivanov, J., R.D. Miller, and S.L. Peterie. 2016. Detecting and delineating voids and mines using surface wave methods in Galena, Kansas. *SEG International Exposition and 86th Annual Meeting*, 2344–2350.
- [16] Ivanov, J., R.D. Miller, S.L. Morton, and S.L. Peterie. 2019. Detecting and delineating voids and mines using surface wave methods in Southeastern Kansas: *ICEG Meeting*, 24–27.
- [17] Ivanov, J., R.D. Miller, D.Z. Feigenbaum, and S.L. Peterie. 2017. Detecting subsurface objects and identifying voids possibilities using the backscatter analysis of surface waves (MASW) method: 4th International Conference on Engineering Geophysics, Expanded Abstracts, 116–119.
- [18] Jouniaux, L., A. Mainault, V. Naudet, M. Pessel, and P. Sailhac. 2009. Review of self-potential methods in hydrogeophysics. *Comptes Rendus Geoscience*, 341, no. 10–11, 928–936.
- [19] Keller, G.V. and F.C. Frischknecht. 1966. *Electrical methods in geophysical prospecting*. Oxford, England, Pergamon Press, 519 p.
- [20] Khaidukov, V., E. Landa, and T.J. Moser. 2004. Diffraction imaging by focusing-defocusing: An outlook on seismic superresolution. *GEOPHYSICS*, 69, 1478–1490.
- [21] Kutrubes, D. L., M. Andrews, M. Andrews, and M. Denham. 2008. Time-depth imaging to locate bedrock fractures and voids, Saint James, Barbados. *SAGEEP*, 518–528.
- [22] Laureti, S., M. Ricci, M.N.I.B. Mohamed, L. Senni, L.A.J. Davis, and D.A. Hutchins. 2018. Detection of rebars in concrete using advanced ultrasonic pulse compression techniques. *Ultrasonics*, 85, 31–38.
- [23] Moran, M.L. and R.J. Greenfield. 1993. Radar signature of a 2.5-D tunnel. *GEOPHYSICS*, 58, 1573–1587.

- [24] Morton, S.L.C., S.L. Peterie, J. Ivanov, R.D. Miller, D.Z. Feigenbaum, S.D. Sloan, M.L. Moran, and H.H. Cudney. 2016. Feasibility study using surface wave attenuation and seismic quality factor for tunnel detection at the Yuma Proving Ground, Arizona. 86th International Annual Meeting, SEG, Expanded Abstracts, 2351–2356.
- [25] Morton, S.L., R.D. Parsons, and J. Han. 2024. Time-lapse shear-wave velocity changes corresponding to stages of soil arching using a trapdoor and the multichannel analysis of surface waves. *International Journal of Geomechanics*, 24(10), 04024207–1 to 04024207–12.
- [26] Munk, J. and R.A. Sheets. 1997. Detection of Underground Voids in Ohio by Use of Geophysical Methods: U.S. Geological Survey. Water-Resources Investigations Report 97–4221.
- [27] Nasser-Moghaddam, A., G. Cascante, and J. Hutchinson. 2005. A new quantitative procedure to determine the location and embedment depth of a void using surface wave. *Journal of Environmental and Engineering Geophysics*, 10, no. 1, 51–64.
- [28] Nyquist, J.E. and C.E. Corry. 2012. Self-potential: The ugly duckling of environmental geophysics. *The Leading Edge*, 21, no. 5, 446–451.
- [29] Ortega-Ramirez J., M. Bano, and L.A. Villa-Alvarado. 2020. GPR for detecting cracks and voids in a historical mural, before restoration, on the altar wall of a XVII century church, Mexico City. 18th International Conference on Ground Penetrating Radar, 22–25.
- [30] Papadakis, E.P. 1968. Buffer-rod system for ultrasonic attenuation measurements. *Journal of Acoustical Society of America*, 44, no. 5, 1437–1441.
- [31] Peterie, S.L. and R.D. Miller. 2015. Near-surface scattering phenomena and implications for tunnel detection. *Interpretation*, 3, no. 1, SF43–SF54. doi: 10.1190/int–2014–0088.1.
- [32] Peterie, S.L., R.D. Miller, J. Ivanov, and S.D. Sloan. 2020. Shallow tunnel detection using SH-wave diffraction imaging. *GEOPHYSICS*, 85, no. 2, EN29–EN37.
- [33] Peterie, S.L., R.D. Miller, and D.W. Steeples. 2009. Diffraction imaging versus reflection processing for shallow void detection. SEG International Exposition and Annual Meeting, 1421–1424.
- [34] Phillips, C., G. Cascante, and J. Hutchinson. 2000. Detection of Underground Voids with Surface Waves. Symposium on the Application of Geophysics to Engineering and Environmental Problems, EEGS, Expanded Abstracts, 29–37.

Detection of Voids Behind Spillways, Conduits, Canals, Tunnels, and Siphons

- [35] Prikryl, J.D., R.N. McGinnis, and R.T. Green. 2007. Evaluation of three-dimensional electrical resistivity array types for optimal detection of voids in karstic limestone. *SAGEEP*, 1538–1549.
- [36] Pugin, A. J.M., K. Brewer, T. Cartwright, and S.L. Sargent. 2019. Detection of tunnels and boulders using shallow SH-SH reflected seismic waves. *The Leading Edge*, 38, no. 6.
- [37] Qin, H., X. Xie, Y. Tang, and Z. Wang. 2020. Experimental study on GPR detection of voids inside and behind tunnel linings. *Journal of Environmental and Engineering Geophysics*, 25, no. 1, 65–74.
- [38] Sastry, R.G. 2014. Geoelectric imaging scores over MASW in geotechnical site characterization. *Symposium on the Application of Geophysics to Engineering and Environmental Problems, EEGS, Expanded Abstracts*, 521–531.
- [39] Schwenk, J.T., S.D. Sloan, J. Ivanov, and R.D. Miller. 2016. Surface-wave methods for anomaly detection. *GEOPHYSICS*, 81, no. 4, EN29-EN42.
- [40] Sloan, S. 2015. A current look at geophysical detection of illicit tunnels. *The Leading Edge*, 34, 154–158.
- [41] Sloan, S.D., and D.Z. Feigenbaum. 2020. Examples of seismic resonance from air-filled voids: *SEG International Exposition and 90th Annual Meeting, 1955–1959*.
- [42] Sloan, S.D., Miller, R.D., Ivanov, J., Moran, M.L., and H.H. Cudney. 2016. Depth estimation of voids using backscattered surface waves. *SEG International Exposition and 86th Annual Meeting*, 2362–2366.
- [43] Sloan, S.D., J.J. Nolan, S.W. Broadfoot, J.R. McKenna, and O.M. Metheny. 2013. Using near-surface seismic refraction tomography and multichannel analysis of surface waves to detect shallow tunnels: A feasibility study. *Journal of Applied Geophysics*, 99, 60–65. DOI: 10.1016/j.jappgeo.2013.10.004.
- [44] Sloan, S.D., S.L. Peterie, J. Ivanov, R.D. Miller, and J.R. McKenna. 2010. Void detection using near-surface seismic methods, in R.D. Miller, J.D. Bradford, and K. Holliger, eds., *Advances in near-surface seismology and ground-penetrating radar*. Society of Exploration Geophysicists, 201–218.
- [45] Sloan, S. D., S. Peterie, R.D. Miller, J. Ivanov, J.T. Schwenk, and J. McKenna. 2015. Detecting clandestine tunnels using near-surface seismic techniques. *GEOPHYSICS*, 80, no. 5, EN127-EN135.
- [46] Xia, J., J.E. Nyquist, Y. Xu, and M.J.S. Roth. 2008. Feasibility of detecting voids with Rayleigh-wave diffraction. *SAGEEP*, 1168–1180.

- [47] Zeng, C., J. Xia, R.D. Miller, G.P. Tsoflias. 2009. Modeling results on detectability of shallow tunnels using Rayleigh-wave diffraction. 79th International Annual Meeting, SEG, Expanded Abstracts, 1425–1429.